Microstructure evolution under tribological loading and its elementary mechanisms

Zur Erlangung des akademischen Grades eines
DOKTORS DER INGENIEURWISSENSCHAFTEN (Dr.-Ing.)

bei der KIT-Fakultät für Maschinenbau des
Karlsruher Instituts für Technologie (KIT)
genehmigte

DISSERTATION

von

M. Sc. Zhilong Liu

Tag der mündlichen Prüfung: 02.05.2018
Hauptreferent: Prof. Dr. rer. nat. Peter Gumbsch
Korreferent: Prof. Dipl.-Ing. Dr. rer. nat. Gerhard Dehm
Korreferent: KIT Associate Fellow Dr. rer. nat. Christian Greiner

Summary

Tribology, the science and technology of interacting surfaces in relative motion, is of great importance for many aspects of modern life. Friction and wear of metallic materials are crucial for energy efficiency and durability of many products from combustion engines to artificial limbs and joints. Microstructure change beneath the surface of material under frictional loading is not always continuous even in very mild sliding condition. Different tribologically induced layers parallel to the sliding surface have been very commonly observed. These layers can often be distinguished by the different grain size inside and a sharp boundary between them. This boundary is a discontinuity in the microstructure. It is of particular interest because it separates the surface layer from the bulk material underneath. The surface layer is exactly where the real contact happens, where the surface chemical reactions take place and where wear particles are generated. The formation mechanisms for this discontinuity are still elusive. This thesis embarks on investigating the origin of this discontinuity by performing the most simplified tribological experiment: a single sliding pass of a sapphire sphere on a high-purity copper sample. This experiment generates a generic microstructural feature seen by (scanning) transmission electron microscopy - a sharp line feature referred to as “dislocation trace line” - around 100 nm beneath the surface. It is interpreted as a dislocation self-organization structure caused by a sign change in the shear stress field in the sample induced by the sliding sphere on the surface.

The dislocation trace line is the very origin of microstructural discontinuity and its influence on the microstructure remains significant also for all further tribological loading. Monitoring the microstructure evolution through different stages of tribological loading, the formation of dislocation networks, growth of the tribologically induced layer and surface oxidation have

been observed. A sequence of these elementary processes is proposed and the elementary mechanisms behind them are revealed.

Among the elementary processes, tribological induced surface oxidation is characterized in detail as a distinct process on the sample surface. The tribological performance of the system - determined mostly by the surface layer - is significantly affected by the surface chemical reaction during the intermediate and late stages of tribological loading. The pathway for oxygen entering copper via tribologically induced oxidation is revealed. A formation mechanism for the amorphous / nanocrystalline cuprous oxide is proposed. This knowledge is of key importance because, once understood, it will allow for surface engineering and superior tribological performance.

The work in this thesis covers the whole microstructure evolution in high-purity copper in contact with sapphire spheres. It contributes to the fundamental knowledge which allows for a deep understanding to the deformation mechanisms under tribological loading. This work also provides critical information for future modelling aiming at predicting the performance of a tribosystem with respect to the evolution of friction and wear, especially during the early stages of sliding.

Zusammenfassung

Tribologie, die Lehre und Technologie von aufeinander wirkenden Oberflächen in Relativbewegung, ist von großer Bedeutung für viele Aspekte des alltäglichen Lebens. Reibung und Verschleiß von metallischen Werkstoffen sind zentral für die Energieeffizienz und Dauerhaftigkeit vieler Produkte, vom Verbrennungsmotor bis hin zu künstlichen Gliedmaßen oder Gelenken. Veränderungen der Mikrostruktur unterhalb der Oberfläche von Materialien unter tribologischer Belastung sind nicht immer kontinuierlich, selbst unter milden Gleitbedingungen. Sehr häufig wurden verschiedene tribologisch induzierte Schichten parallel zur Gleitrichtung beobachtet. Diese können oft durch unterschiedliche Korngrößen innerhalb der Schichten sowie einer scharfen Grenze dazwischen unterschieden werden. Diese Grenze ist eine Diskontinuität in der Mikrostruktur und von besonderem Interesse, da sie die Oberflächenschicht vom darunterliegenden Grundmaterial trennt. Die Oberflächenschicht ist der Bereich, in dem der reale Kontakt stattfindet, die chemischen Reaktionen an der Oberfläche ablaufen und Verschleißpartikel erzeugt werden. Die Bildungsmechanismen dieser Diskontinuität sind noch unklar. Ziel dieser Arbeit ist es, den Ursprung dieser Diskontinuität mittels eines soweit wie möglich vereinfachten tribologischen Experiments zu untersuchen: dem einmaligen Übergleiten einer hochreinen Kupferprobe mit einer Saphirkugel. Dieses Experiment erzeugt ein typisches Merkmal - eine als „Versetzungsstreifen“ (dislocation trace line) bezeichnete, scharfe Linie, die etwa 100 nm unter der Oberfläche mittels (Raster-) Transmissionselektronenmikroskopie beobachtet werden kann. Diese wird als eine selbst-organisierte Versetzungsstruktur interpretiert, welche durch einen Vorzeichenwechsel im Schubspannungsfeld in der Probe verursacht wird, hervorgerufen durch den gleitenden Gegenkörper auf der Oberfläche.

Der Versetzungsstreifen ist der Ursprung der mikrostrukturellen Diskontinuität und sein Einfluss auf die Mikrostruktur bleibt auch für weitere tribologische Belastungen maßgeblich. Durch die Betrachtung der Mikrostrukturentwicklung in verschiedenen Stadien tribologischer Beanspruchung konnten die Bildung von Versetzungsnetzwerken, das Wachstum einer tribologisch induzierten Schicht sowie Oberflächenoxidation beobachtet werden. Auf Basis der Beobachtungen wurden die Elementarmechanismen aufgedeckt sowie eine zeitliche Abfolge dieser grundlegenden Prozesse vorgeschlagen. In diesem Zusammenhang wird die tribologisch induzierte Oberflächenoxidation detailliert, als charakteristischer Vorgang an der Probenoberfläche, untersucht. Das tribologische Verhalten des Systems – hauptsächlich durch die Oberflächenschicht bestimmt – wird maßgeblich durch die chemischen Reaktionen an der Oberfläche während der mittleren und späten Stadien der tribologischen Beanspruchung beeinflusst. Der Pfad, auf dem Sauerstoff aufgrund der tribologisch induzierten Oxidation in das Kupfer eintritt, wird aufgedeckt. Ein Mechanismus für die Bildung von amorphem/nanokristallinem Kupfer(I)-oxid wird vorgeschlagen. Dieses Wissen ist von wesentlicher Bedeutung, da durch das Verständnis der Mechanismen ein Maßschneidern von Oberflächen hinsichtlich verbessertem tribologischem Verhalten möglich wird.

Diese Arbeit umfasst die komplette Mikrostrukturentwicklung in hochreinem Kupfer in Kontakt mit Saphirkugeln. Sie trägt zum grundlegenden Wissen bei, welches ein tieferes Verständnis von Verformungsmechanismen unter tribologischer Beanspruchung erlaubt. Des Weiteren beinhaltet diese Arbeit unverzichtbare Informationen für Modelle, welche darauf abzielen, das Verhalten eines Tribosystems hinsichtlich der Entwicklung von Reibung und Verschleiß vorherzusagen - insbesondere in frühen Stadien des Gleitens.

Acknowledgement

First, I would like to express my sincere gratitude to Prof. Peter Gumbsch for advising my doctoral work for the past four and half years. His deep understanding to the field, his dedication to high-quality research and his passion and energy for science have always been inspiration and encouragement to me. His extremely valuable advices and generous help along the way of my entire time in Karlsruhe are greatly appreciated.

I very much appreciated the opportunity Dr. Christian Greiner offered me to join his group in Karlsruhe. In the past four and half years, as my advisor, Christian has shown me how to be a successful scientist with himself as a perfect example. I sincerely thank Christian for his thorough training to my skills to be a scientist, for his continuous support to my research, and foremost for his trust in me and in my work. He is a mentor to me for my scientific work and a cordial guide for my life in Germany.

I would like to thank Prof. Gerhard Dehm as the co-referee in the committee for his precious time and effort reading and evaluating this thesis.

I very much appreciated all the help that I received to finish this thesis. Dr. Johannes Schneider has been kindly helping me in many aspects of my work in KIT. His valuable suggestions greatly improved the quality of my work and I thank him for proof reading this thesis. I would like to thank Prof. Lars Pastewka, for the helpful discussion on modelling my experimental results. I very much appreciate Dr. Reinhard Schneider's expertise in TEM and the fruitful collaboration with him. Prof. Thomas Höche and Dr. Christian Patzig kindly performed the TEM and EDXS measurements for my samples and have my sincerely gratitude also for their suggestions on the collaborative publication. I thank Dr. Luis Straßberger for the helpful TEM sessions and the intriguing discussions with him. I thank Dr. Moritz Wenk for sharing his rich knowledge of EBSD technique and his Matlab codes for data analysis. The valuable XPS measurements with the help from Eberhard Nold and Dr.

Dominic Linsler are much appreciated. I also would like to mention the helpful and stimulating discussions with Dr. Daniel Weygand and Johanna Gagel. I thank Michael Schäfer and Philipp Messer for their excellent work in our group as master students.

I appreciate the technical support from Katja Hahn, Friedbert Keller, Marcel Milich, Yiyue Li and the administrative support from Andrea Doer and Ines Knoch. Specifically, I would like to thank Michael Germann for his generous, quick and constant support to our microscope with which most of the images in this thesis were produced.

I must express my gratitude to my fellow colleagues and friends. We've been fighting in the same trench against the challenges in scientific research and my work and life in Karlsruhe has been so delightful because of them. The heart-warming welcome and help from Dr. Daniel Braun and Uwe Popp made my start in KIT smoother than I dared to imagine. Paul Schreiber has always been a caring friend and helped me to render the most beautiful picture in this thesis. Julia Lehmann's kindly help to translate thoroughly the Summary into Zusammenfassung is very much appreciated. It has been and will always be my great pleasure and honor to share the offices and labs with Sarah Becker, Friederike Ruebeling, Daniel Kümmel, Dr. Xiang Chen and Christian Haug. I appreciated every moment we worked together.

Personally, I want to thank my parents for their unconditional support. I want to thank my wife Jieqi Zheng for her understanding and continuous support. She has always been the warmth and light for me to keep going.

Karlsruhe, February 2018 Zhilong Liu

Table of Contents

Chapter 1: Introduction

1.1 Background

The subject of tribology – interacting surfaces with relative motion – appears across different length scales [1]: from mountains and rocks at the continental scale in geology [2] to a single asperity sliding at the atomic scale in contact mechanics [3]. Correspondingly, tribology is of great importance for many aspects of modern life [4]. For example, it is critical to energy efficiency in almost all engineering systems with moving parts [1, 5]; Micro-electromechanical systems' (MEMS) performance can be largely improved with the achievement of tribology at a small scale [6]; The understanding of friction and wear is critical to explain and solve most of the problems in the application of artificial hip joint implants [7, 8]; Knowledge in rate and state friction theory allows for a deep understanding and in the future a reliable prediction of earthquakes which concerns people's life and properties [2, 9]. In recent years, the field of tribology's applications in the energy efficiency has been even more widened, expanding to daily wearable equipment [10] as well as to massive energy harvest from nature [11]. Superlubricity [12, 13] and 2D ultra-low friction materials [14, 15] have already become one of the hottest topics in science, opening new fields of research in tribology.

1.1.1 An early history of tribology

The evidence of humans trying to reduce friction has been found thousands of years ago. The first documented successful application of reducing friction (Figure 1.1a) can be traced back to ancient Egyptian era [1]. The very first rational description of friction phenomena (Fig. 1.1b) was proposed merely over 500 years ago by Leonardo da Vinci [16]. The two laws of friction, however, were rediscovered in 1699 by and commonly named after Guillaume

Amontons. It was stated that the friction force should be proportional to the normal force applied to the sliding contact and the friction force is independent of the contacting area. Later on, in 1785, independence of sliding speed was complemented to Amontons' law by Charles-Augustin Coulomb. These three laws until today still hold to certain conditions (e.g. dry sliding under a large load with little or no adhesion).

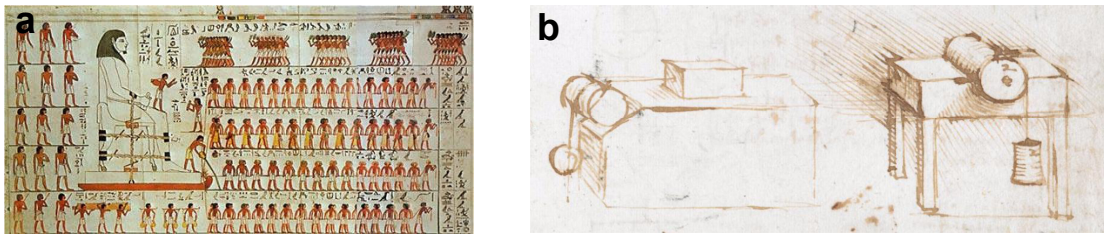

Figure 1.1: Records in early history in tribology. (a) A wall painting from ancient Egypt from 1800 BC on the tomb of Djehutihotep [17]. (b) Leonardo da Vinci's notes and sketches relating to the laws of friction [16].

The name "tribology" was coined by Tabor and Jost [18, 19] in the 1960s and eventually widely accepted by scientists and engineers. Before the molecular theory was applied in tribology, an understanding to friction heavily relied on contact mechanics. The continuum models developed in classical contact mechanics offered an excellent guide line for analyzing the contact stress at that time. Hertz in 1882 firstly proposed an elastic contact model [20]. When the intermolecular forces started to be recognized as the force countering the normal force which pushed the two objects together [21], many mysterious phenomena could find their explanation outside Amontons' laws at a much smaller scale [22], for example, the friction force observed at zero or even negative normal load (explains why geckos stick to walls) [23]. Since the force between molecules (or atoms) depends on the distance between them, in theory, the two interacting surfaces could either pull toward or push against each other when the distance between them changes. The contact then could no longer be considered as simple as two surfaces being pushed together by the normal load. Adhesion

was added to Hertzian theory by the later investigators, e.g. Johnson and Maugis, and two dominating models were developed to describe the contact mechanics [24, 25]. Johnson-Kendall-Roberts (JKR) model assumes the adhesion exists only inside the contact area, and Derjaguin-Muller-Toporov (DMT) model considers the attractive force from outside the Hertzian contact area. Tabor eventually brought the above two models together by introducing a material parameter [26], which could switch cases between the two models depending on the properties of the contacting materials.

1.1.2 Solutions in continuum theory

Hertz in 1882 published the analytical solution to the contact stress between two curved surfaces under a normal load which pushes them together [20]. In his theory (later referred to as the classical Hertzian model), the following assumptions are made: a) the surfaces are continuous and non-conforming; b) the strains are small; c) each solid can be considered as an elastic half-space; d) the surfaces are frictionless. The absolute value of the contact size, a, compression, δ, and maximum pressure, p_0, can be expressed as following:

$$a = \left(\frac{3PR}{4E^*}\right)^{1/3} \tag{1}$$

$$\delta = \frac{a^2}{R} = \left(\frac{9P^2}{16RE^{*2}}\right)^{1/3} \tag{2}$$

$$p_0 = \frac{3P}{2\pi a^2} = \left(\frac{6PE^{*2}}{\pi^3 R^2}\right)^{1/3} \tag{3}$$

where $\frac{1}{E^*} = \frac{1-{\nu_1}^2}{E_1} + \frac{1-{\nu_2}^2}{E_2}$; P is the normal load; R is the relative radius of curvature [25]. E_1 and E_2 are the bulk Young's modulus of the two contacting bodies, with ν_1 and ν_2 being their Poisson's ratio.

The first model adding friction to the contact mechanics was proposed by Mindlin in 1949 within the elastic deformation regime [27]. The assumption made here is that the tangential traction in the contacting surface is everywhere proportional to the normal. Hamilton and

Goodman then in 1966 [28] investigated the stress field underneath the surface. This has brought a great leap for the stress field prediction under tribological loading. In 1983, Hamilton published the explicit equations for the stresses in the subsurface area under a sphere-plane sliding contact, offering a convenient analytical solution [29] (the details of this solution can be found in Appendix I). The contour maps of von Mises yield stress normalized by the maximum Hertzian pressure for the classical Hertzian model and the Hamilton's solution are presented in Figure 1.2.

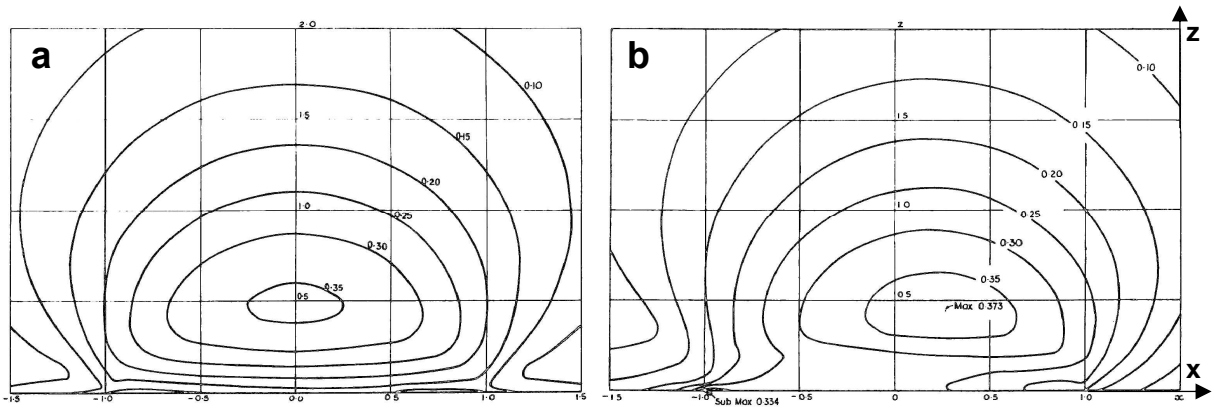

Figure 1.2: Contour maps of von Mises yield stress of a circular contact in the subsurface cross-sectional area of the contact calculated using the classical Hertzian model and the Hamilton's solution, normalized by the maximum Hertzian pressure. (a) Hertzian model; (b) Hamilton solution. The coefficient of friction here is 0.25. Distances are normalized by the Hertzian contact radius and the stress level is normalized to the maximum Hertzian pressure. z-axis is the sample surface normal and x-axis is the sliding direction [28]. An enlarged figure can be found in Figure A1 in the Appendices for more details.

Following Mindlin's assumption, in Hamilton's work, a sliding contact loading was decomposed into a normal force pushing the surfaces together and a tangential force acting as the friction force. The normal force component was borrowed from the classical Hertzian theory and the tangential force was dependent on the coefficient of friction.

Hamilton's solution provided a practical method to calculate the stress field under the sliding contact, and it has been used to explain many phenomena in tribology, for example, to predict

the elastic stress field in ceramic materials in sliding contact and to understand the friction and wear behaviors in coatings [30, 31]. Due to the complex stress / strain conditions and the various deformation mechanisms triggered at the interface, there has not yet been a theory which can offer a satisfactory solution to the contact stress with plastic deformation in the subsurface area. An elastic model in this case, even though being insufficient because of the lack of the influence from plasticity, gives a very good estimation to the stress level and its distribution inside the material. This, as a first step, serves very well [32, 33] allowing for an interpretation of the materials' behavior under tribological loading.

1.1.3 Asperities, a different world at small scale

In continuum models, the geometry of the contacting surfaces and the normal load decides the apparent contact area. A major assumption of the continuum theory here is that the contacting area is smooth and the strain of elastic / plastic deformation follows the bulk properties. However, a mathematically flat or atomically smooth surface does not exist experimentally due to the inevitable roughness of any surface. A seemingly simple question then is: what is actually "in contact"? The contact should only exist at the asperities and be part of the apparent contact area. Therefore, the real contact area should be much smaller than the apparent contact area usually considered in continuum models. This has been confirmed via the in-situ observation of various contacts [34, 35]. Figure 1.3 presents the contact at different length scales. The contact at these asperities makes the continuum models break down when facing the small-scale problems, because a) the contact surface can no longer be considered as perfectly smooth and b) the deformation is dominated by a cutoff at the asperities instead of continuum strain deduced from bulk elastic properties. The "real contact area" later is referred to as the sum of pairs of atoms, one from each plane, the distance between which is smaller than the separation at the potential energy minimum [36, 37]. A model to describe the rough surfaces contact has been developed with success through

different length scales [38]. Recently, the term of "contact quality" has been proposed [39] as a more appropriate term to characterize the contact.

One of the important branches of tribology – nanotribology - was established in the 1980s. The scanning tunneling microscopy (STM), atomic force microscopy (AFM), surface forces apparatus (SFA) and nanoindentation are the main experimental methods to investigate the surface with high lateral resolution. Except for the SFA, they share the synergy of applying a sharp tip as a probe to measure the surface topography and to test small scale mechanical properties of the surface. These techniques contribute greatly to the contact mechanics and serve as novel testing methods in tribology [14, 40, 41]. Combining advanced electron microscopy techniques (e.g. applying a nanoindenter inside a transmission electron microscope with a specially manufactured holder), in-situ observation of the contact and the microstructure of the contacting materials is available [3, 42]. Here the contact literally happens on a single asperity (tip of the probe), which can be entirely modeled using atomistic methods, e.g. molecular dynamics [43, 44].

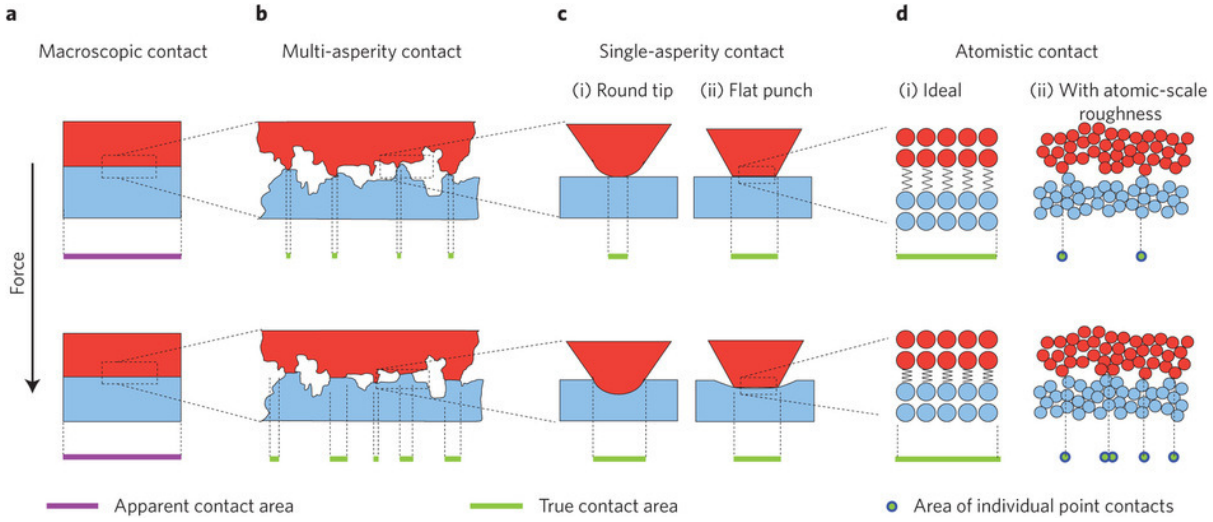

Figure 1.3: Schematics of the contact at different size scales. (a) Macroscopic contacts appear smooth; (b) The real contact area consists a large number of contact points. (c) Nanoscale single-asperity contacts appear to be smooth; (d) Single asperity contact can be treated as atomically smooth (i) or atomically rough (ii) depending on the applied force and surface condition [45].

When attempts are made to connect the phenomena from single asperities with macroscopic phenomena [46], the challenges from length and time scales appear to be a barrier. This is mainly because, on the one hand, the stress level in single asperity experiments is usually higher by a few orders of magnitude than the stress level in macroscopic applications and this cannot be fixed through simply summing up all the asperities; on the other hand, the atomic simulations are only capable to calculate the system's response in an extremely short time window (typically in the range of 10^{-12} s) within a relatively small volume (typically tens or hundreds of layers of atoms). These cause the strain and the strain rate at a small scale, especially for atomistic simulations, to be dramatically higher than the reachable level in macroscopic experiments. These gaps are being filled by means of using larger volumes of atoms in simulation and wider time windows [47]. Agreements between atomic simulations and macroscopic experiments in certain aspects, for example, chemistry changes near the contacting surfaces [47, 48] can be found. Yet, there is still a long way to go before a realistic comparison of results can be achieved through the length and time scales.

1.2 Microstructure evolution under tribological loading, the key lies beneath the surface

Zooming out from a single asperity, at a scale of millimeters and meters, where most engineering components can be found, the properties of the materials underneath the surface are significantly influencing the friction and wear.

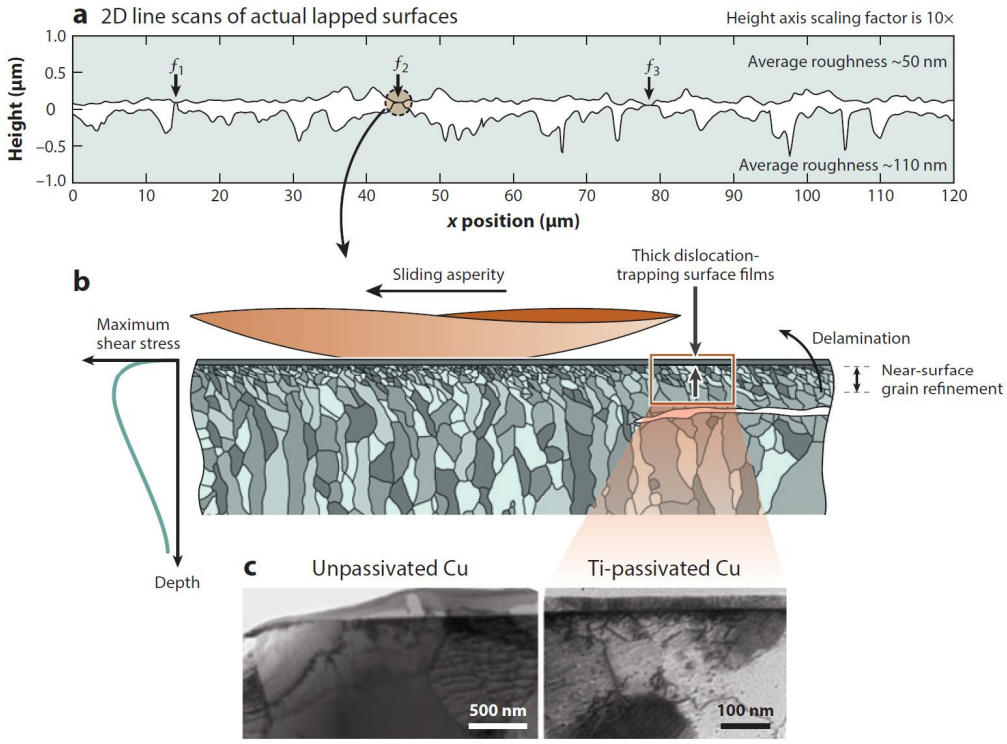

Figure 1.4: Schematic diagrams showing the microstructure under tribological loading adopted from reference [49]. (a) Cross-sectional view of a real contact between polished metal surfaces. (b) A schematic diagram of delamination wear in a mildly wearing, otherwise unlubricated metal contact. (c) Cross-sectional transmission electron microscopy images [50] of fatigued (fully reversed, bulge test) Cu films both unpassivated (left) and Ti passivated (right).

Figure 1.4 presents a schematic view of how the microstructure is changed by sliding contact. The modified microstructure then determines the materials' properties, which is key to tribological performance [51]. In contrast to focusing on the surface and the single asperity contact, the work documented in this thesis is mainly inspired and motivated by the research in microstructure changes under tribological loading. A more detailed background will be presented in the next section.

1.2.1 Introducing materials science into tribology

In the 1950s, Bowden and Tabor stated that junctions were formed and sheared during a metallic sliding contact [51]. If one of the sliding partners was harder than the other, the

softer surface would be ploughed to an appreciable depth by the hard surface's asperities, and hence the bulk properties of the softer surface determine the friction and wear properties of the entire tribosystem [51]. Since then, studying tribology from the materials science's point of view has become an additional focus in the field.

Neglecting the ploughing effect during the sliding contact, friction can be expressed as $F = A \cdot s$, where A is the real contact area and s is the shear strength of the softer metal. With any particular metal, the real contact area A is determined primarily by the load W, and $W = pA$, where p is the flow (yield) pressure of the softer metal [52]. The coefficient of friction (COF) in a sliding system is therefore expressed as the ratio of the shear strength to the flow pressure of the softer metal [51, 52]:

$$\mu = \frac{F}{W} = \frac{s}{p} = \frac{shear\ strength}{flow\ pressure} \tag{4}$$

Multiple strengthening and hardening mechanisms (e.g. grain boundary strengthening, work hardening) will be triggered in the material with a tribologically induced microstructure. The shear strength and flow pressure are then changed with a modified microstructure. Therefore, the subsurface microstructure has a strong influence on the frictional properties of the surface [53-55]. At the same time, the subsurface microstructure is strongly affected by plastic deformation and the corresponding dislocation activity under a tribological load [54, 56-62]. This can be described as a feedback loop (Figure 1.5) between grain size, stress field and friction force [63]. The microstructure evolution under the sliding contact is therefore key for tailoring materials that combine low friction and wear.

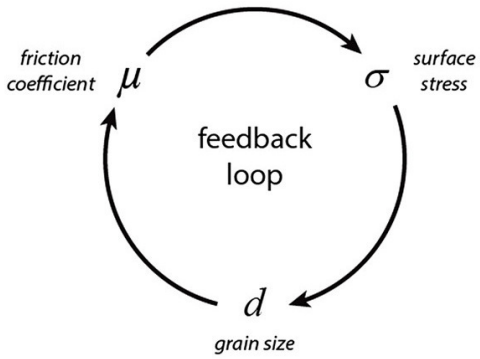

Figure 1.5: Feedback loop between friction coefficient, μ, surface stress, σ, and grain size, d. Figure adopted from reference [63].

Pioneering works have been implemented in this direction in the past decades by observing the microstructure under tribological loading [58, 64-66]. With the help of advanced and sophisticated electron microscopy, the understanding of the elementary mechanisms behind the tribologically induced deformation was deepened in the past ten years [33, 57, 67-72]. Computational materials science also stepped in, allowing for an understanding of the sliding contact at the atomic scale [39, 47, 73]. Due to the complexity of any tribological contact, the mechanisms for the phenomena such as materials' strengthening and fatigue which have been well studied under conventional loading (e.g. tensile and compression tests) cannot simply and directly explain materials' response to tribological loading. Fundamental knowledge of the elementary processes under tribological loading is still missing.

1.2.2 A generic discontinuity in subsurface microstructure

In the literature, there are two general directions of microstructure research under a tribological load: the first starts with an annealed, large-grained bulk material. Applying a tribological load then leads to modifications in the microstructure that result in a (ultra-) fine-crystalline microstructure near the surface [7, 58, 61, 65, 70, 74-78]. The second approach starts with samples exhibiting a fine or even nanocrystalline layer or thin film on the surface.

The published results demonstrate that recrystallization on the surface and grain boundary motion are dominant mechanisms for making the nanocrystalline grains grow bigger [33, 59, 79, 80]. Microstructure evolution and changes in wear properties under a tribological load, in engineering applications often referred to as the "running-in" of a tribosystem [81, 82], were investigated and explained in both directions for different materials systems such as copper [58, 65, 74, 77, 78, 83], steels [84, 85] and cobalt-based alloys for artificial hip joints [8, 86]. The consensus is that there is a change in the microstructure of ductile metals. Deformed layers, commonly named as "tribo-layers", have been observed in many types of contacts and for different loads (examples see Figure 1.6). The investigations of these tribo-layers' microstructure have shown potentially high capability to explain and to solve problems in mechanical engineering in macroscopic world, e.g. in a combustion engine's cylinder [87].

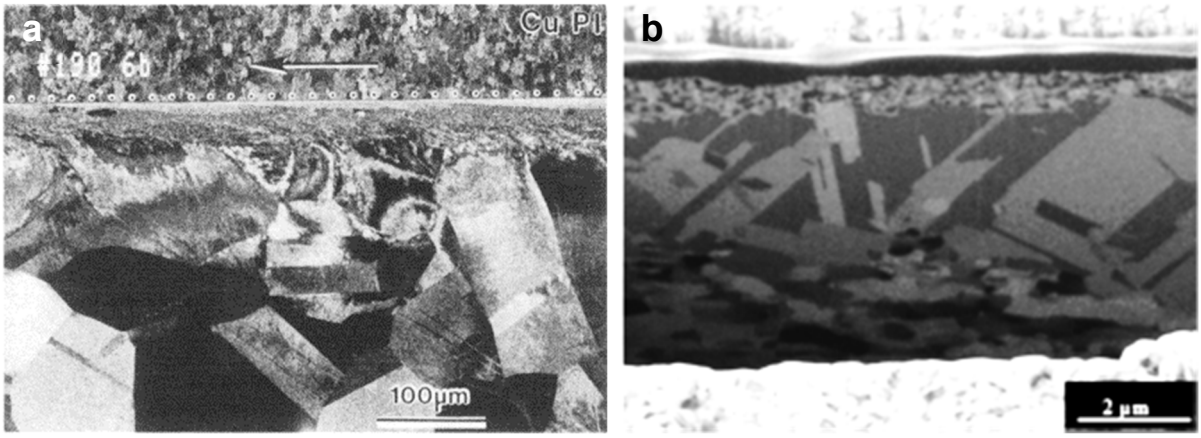

Figure 1.6: Different tribo-layers reported in literature. (a) Subsurface layer in copper during application of large loads in contact with a hardened 4340 steel platen. The sample surface is marked by a dotted line [88]; (b) A sharp transition of grain size in pure copper running against 440C stainless steel balls, separating the nanocrystalline layer and the coarse grain layer beneath (recrystallized, not seen in (a)) [74]. Both images are in a cross-sectional view.

The above mentioned tribo-layers have been characterized into different types, and their behavior been summarized [65, 89-92]. The grain size is observed regularly different in different layers, and sharp boundaries between different layers have been often observed.

This sharp transition of microstructure appears as a generic feature of the tribologically induced microstructure through different tribological systems. In both grain refinement and growth cases, experiments regularly show a distinct discontinuity in the microstructure between a surface layer and the underlying bulk material [7, 33, 60, 70, 77, 78]. The origin of this discontinuity remains elusive but is crucial to the understanding of friction and wear, because the surface layer carries most further plastic deformation, accumulates damage and is exposed to the environment. One of the main goals of the thesis is to find the source of these discontinuities and to reveal its formation mechanisms. This will help to understand the microstructure evolution in all later stages.

1.2.3 Numerical studies on the tribologically induced microstructure change

Atomic simulation can focus on modelling the contact surface, as well as the plastic deformation in the subsurface area with a small volume. Sliding speed [73, 93, 94], crystallographic orientation of the surface [73, 94], and existing lattice defects [94] are considered as variables during these simulations. Corresponding results of an amorphous adlayer on the surface and dislocation activity have been reported [73, 94]. With non-equilibrium conditions, the dependence of friction force on sliding speed has been simulated, and at a high sliding speed, stacking faults and perfect dislocation loops have been observed in both Cu and Ag contact bodies [93]. Crystallographic orientation has also shown its effect on the results [95, 96] and large scale atomistic simulations have demonstrated the self-organization of nanocrystalline grains until the optimal orientation for the plastic slip systems is established parallel to the sliding direction [95].

Dislocation activities under tribological loading are also accessible to discrete dislocation dynamics (DDD) simulations. Simplified microstructures are studied in DDD simulations, because the precise experimental conditions are usually unknown. As a first step to

understand sliding, the simplest contact type – indentation – has already been investigated [97]. It is expected that in the near future DDD simulations will help to understand the dislocation activity under sliding contacts and predict the dislocation structures formed there [98].

1.3 Approaches and directions for microstructure investigation

Based on the experimental and numerical results, different paths have been taken to explain the mechanisms behind changes in the subsurface microstructure. The principle processes for the microstructure evolution that are considered in the literature are plastic deformation, influence of environment (including counter body) and mechanical mixing [99-101]. However, due to the complexity of any sliding contact, the experiments and models in the existing works did not yield a satisfactory picture for the elementary mechanisms at play, especially for the initial stages of tribological loading. In this section, different thoughts, approaches and theories will be brought up in order to present the state of the art knowledge in the field.

1.3.1 Dislocation structure formation and subgrain formation

Dislocation structures were investigated in detail in the subsurface area under tribological loading with large strains [102]. Low energy dislocation structures were observed as expected [103]. Deformation mechanisms similar to severe plastic deformation and cold rolling processes have been applied to explain the grain refinement and dislocation cell formation. Geometrically necessary boundaries and incidental boundaries formation under deformation is considered as one of the main reasons [104, 105] (Figure 1.7).

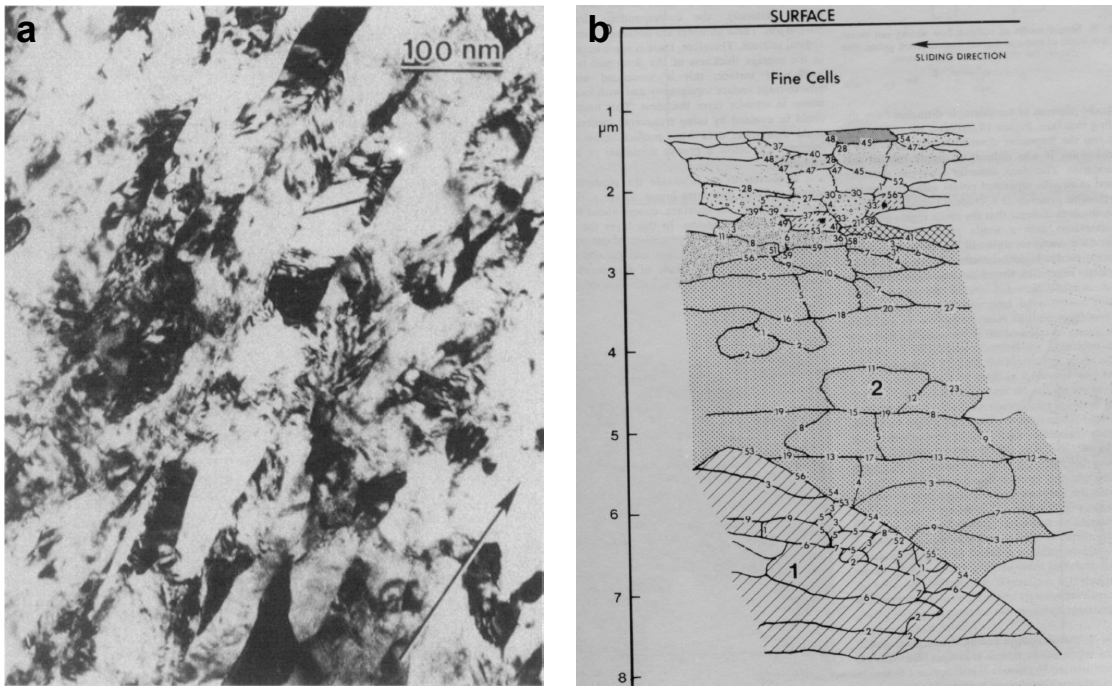

Figure 1.7: Dislocation structure observed in the subsurface area under tribological loading. (a) Lamellar boundaries, cells and deformation twins are formed in copper under large tribological loading [105]; (b) A schematic drawing of fine dislocation cells formed in the subsurface area under tribological loading in copper, the misorientation of the cell boundaries are shown as numbers in the picture [65].

Grains are found to be severely reduced in size in the subsurface area [58, 75, 76, 92, 106] when the initial structure is coarse-grained. On the other hand, an ultra-fine grain structure experienced grain growth under tribological loading through recrystallization [107-109]. Studies have shown that there seems to be an equilibrium surface grain size, in which different initial microstructure states will eventually end up via triggering different deformation mechanisms [63, 68]. The friction force level differs when different deformation mechanisms are triggered and different normal loads are applied [63].

1.3.2 Insight from crystallography

Most of the materials show anisotropy in their mechanical behaviors [110]. In single-phase polycrystalline metals, texture (a preferred crystallographic orientation) is a main reason for

the anisotropic properties [110]. Texture induced by the tribological loading has been an interesting topic for materials scientists [111, 112]. Works have shown that for both polycrystalline [113] and single crystal [112] materials, the crystallographic orientation influences and is influenced by the tribological loading [114, 115]. For example, a preferred crystal orientation for low friction force has been reported in ZnO coatings [116].

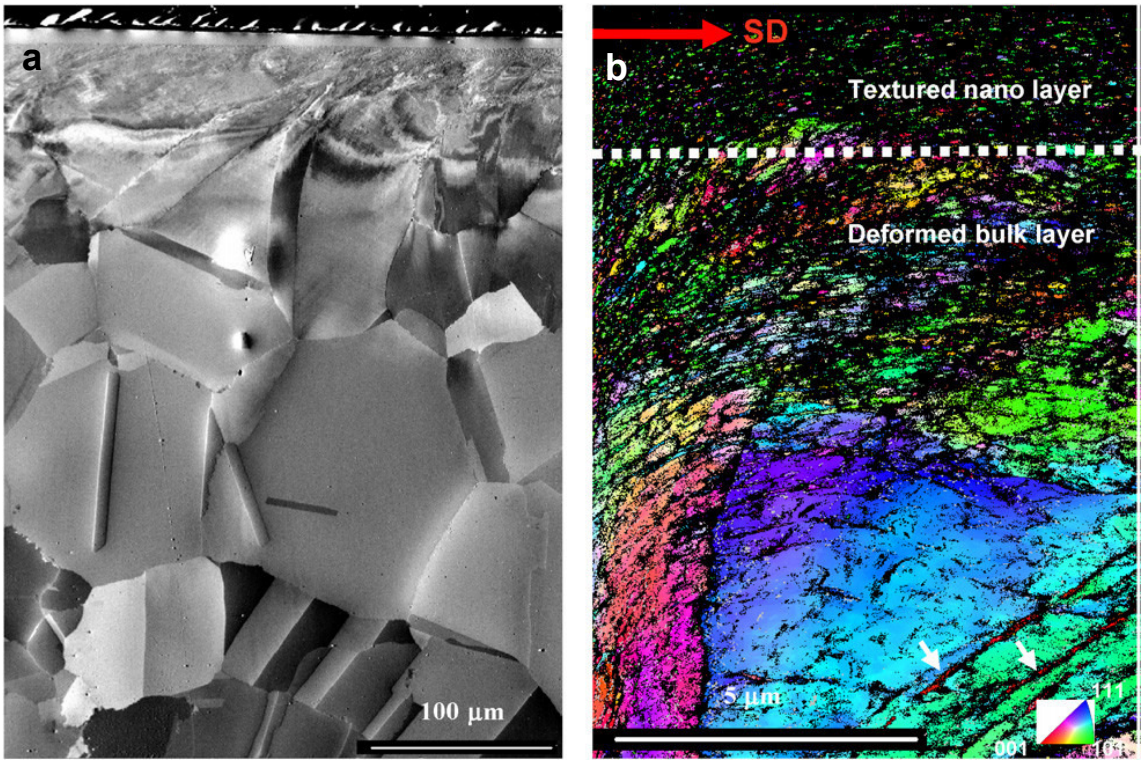

Figure 1.8: Crysallographic orientation imaging of the subsurface microstructure after tribological loading. The spinodally hardened bronze disc sample was worn under 98 N against Ni pin at room temperature. (a) Forward scattered SEM image; (b) crystal orientation mapping [117]. The sliding direction is marked by the red arrow and "SD". The boundary between the textured nano layer and the deformed bulk layer is marked by the white dashed line.

Accompanying the formation of the dislocation structures and the grain refinement, subgrain rotation, which may last for the whole sliding process, has been widely observed in the subsurface area [65]. The rotation axes have been reported to be perpendicular as well as parallel to the sliding direction [65, 118]. This subgrain rotation will likely lead to a surface

texture (Figure 1.8) [117]. In this example, the heavily deformed layer at the sample surface eventually lead to a nanocrystalline layer with a preferred crystallographic orientation. To understand the materials behavior in specific orientations, tribological investigations on single crystals have been performed [89, 112, 116, 118, 119].

The slip system and the path in which the subgrains are reoriented in the sliding contact of a copper single crystal was investigated establishing that the size and localization of the tribo-layer depends on the crystallographic orientation with respect to loading [89, 90]. In similar studies, the generation of wear particles was correlated with the parallelization of the sliding plane to a (111) plane [96, 119]. The orientation of grain boundaries was also observed to influence the tribological behaviors of the material [111].

1.3.3 Plastic flow observation and modelling

A fluid-like flow model has been used to describe the behavior of the near surface material [62, 120]. In these cases, vortex formation can be observed in the subsurface area together with folding of the surface material [59, 62, 96]. Kelvin-Helmholtz instability (Figure 1.9) is one of the common explanations to such vortex formation in the subsurface area. In-situ observation [121, 122] and numerical simulation [99] of their formation has been realized to support this theory.

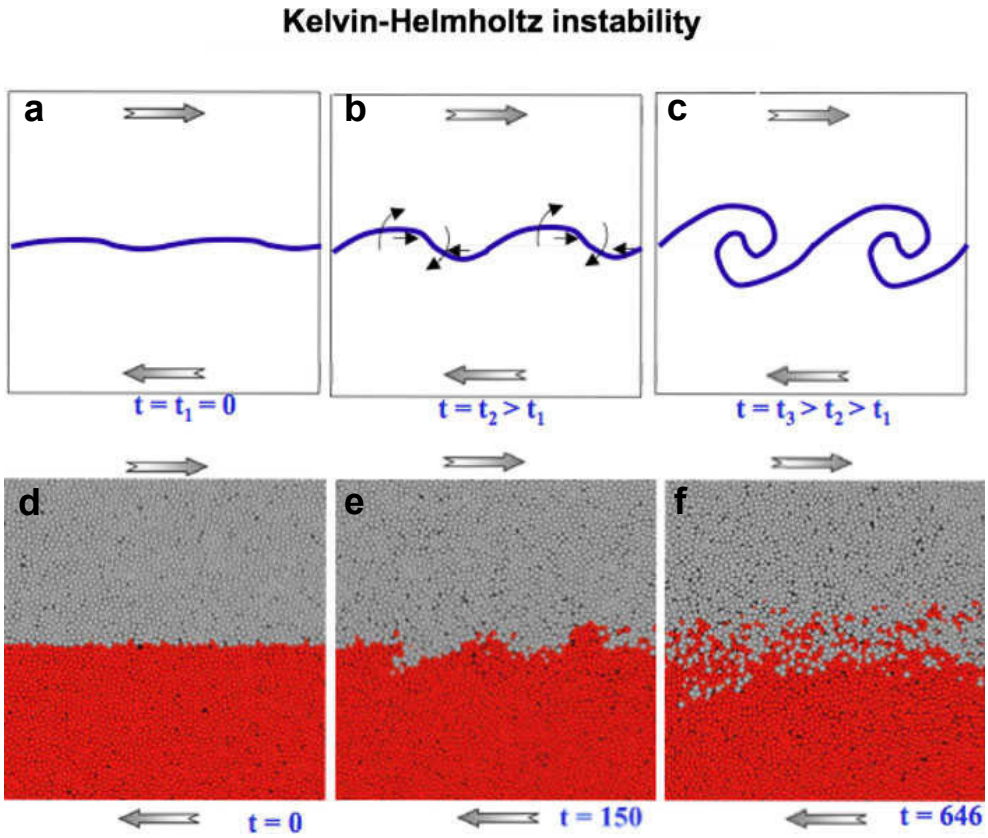

Figure 1.9: (a-c): Schematic diagram of Kelvin-Helmholtz instability (upper three images) and the MD simulation snapshots of evidence of Kelvin-Helmholtz instability; (d-f) a sequence of snapshots from a MD simulation in 2D of self-mated sliding of two-component amorphous material. [99]

Plastic flow through folding caused by plasticity instead of fluid-like instability can also lead to vortex-like structures [96]. Here, the formation mechanisms can be explained very differently to the Kelvin-Helmholtz instability theory (see Figure 1.10). The grains with slip systems orientated to a certain degree with respect to the slider's cutting plane tend to form bulges and the others tend to remain in a smooth surface. This localized grain-size-scale anisotropy in plasticity is interpreted as the elementary mechanisms for the formation of the vortex-like feature in the subsurface area in both experimental results and MD simulations.

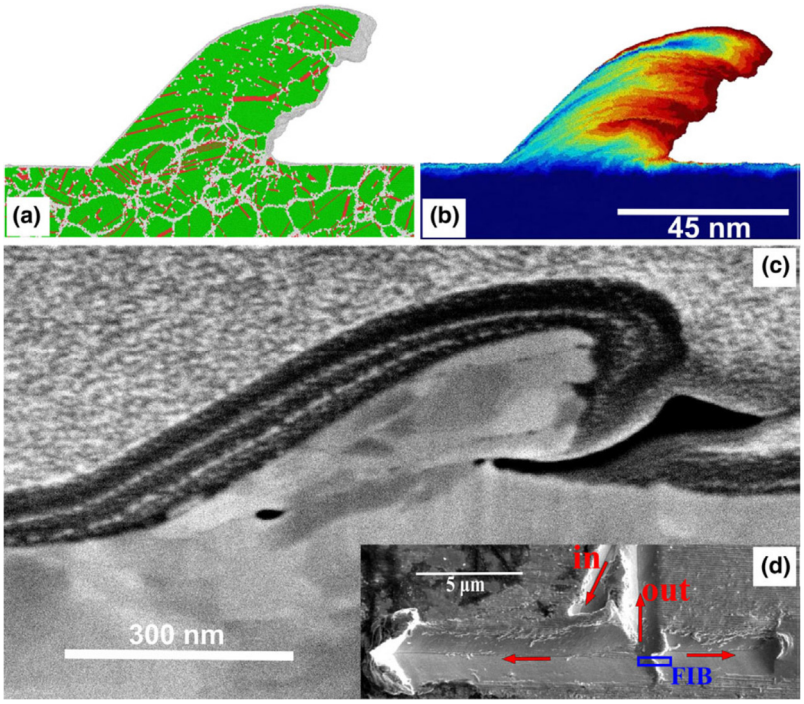

Figure 1.10: Comparison of the final chip in the plowing simulation (at t = 6.5 ns) with a chip formed by experimentally plowing a nanocrystalline copper surface with an AFM tip. Shown are chip cross sections from the atomistic simulation with (a) Common neighbor analysis color code [123] and (b) initial-z (initial vertical position) color code. (c) A FIB cross-sectional side view of the experimental chip. (d) Inset displaying a top view of the wear track with the motion of the tip marked by red arrows and the location of the FIB cut over the chip marked by a blue rectangle.

1.3.4 Strain and stress estimation under tribological loading

The tribologically induced strain and stress field in the subsurface cannot yet be fully predicted due to the commonly existing plastic deformation. Different methods have been implemented to estimate the strain and stress field under tribological loading.

One of the early approaches is from the 1990s [76, 106]. The tribological tests were performed with a special “sandwich” testing rig, where the loading condition can then be simplified to a simple shearing. The very localized stress and strain state is estimated in terms of the spacing between geometrically necessary boundaries, incidental dislocation boundaries and the flow stress of the material [76]. Similar methods using the dislocation cell size to

estimate the stress distribution under tribological loading have also been applied [124]. These methods do not render a continuous field of strain and heavily depend on the materials' properties. It is difficult to apply them in a more universal situation. When the strain is higher than a certain level, the dislocation structures will reach the size limit [125]. This causes the failure of the method in large strain conditions.

Grain boundaries have been used as markers to characterize the strain near the surface [67, 82]. By tracing the displacement of the grain or twin boundaries intersecting the surface, strain profiles can be acquired (Figure 1.11) [67].

The strain under tribological loading can be correlated to the strain in high pressure torsion (HPT) [126, 127] and cyclic loading combining compression and shearing [128]. Both of the processes do share the same loading concept and a well-developed method to calculate the strain in the latter case already exists. Good agreement was found between them, making it a valid estimate. The in-situ observation of plastic flow also offered a method for quantifying the strain in the subsurface area [121]. A strain estimation method [129] from texture generation in steel [130] has also been proposed. The initial state of the microstructure in this method is of critical importance. Only coarse-grained materials can be analyzed with this method. The initial shape and position of the boundaries can only be speculated about and the grain boundary migration may bring artifacts to the results.

The methods presented here are still speculative and may only be valid in a very limited range. However, they do offer a chance for a qualitative strain analysis under tribological loading and are of great help for understanding the microstructure change in the subsurface area.

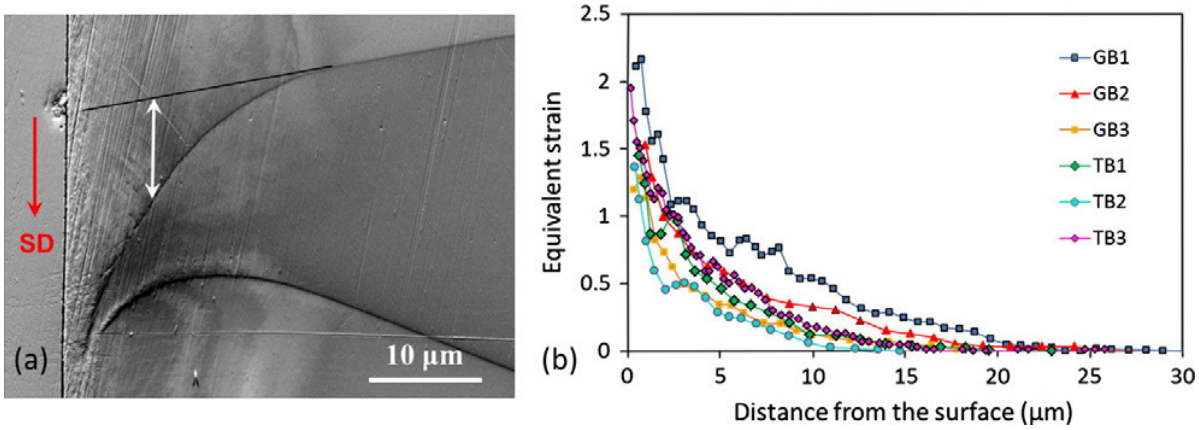

Figure 1.11: Example of using grain / twin boundaries as markers to estimate the strain [67]. (a) SEM image of a cross-section along the sliding direction with two grain boundaries. The red arrow and "SD" mark the sliding direction. The white arrow indicates the hypothesized displacement of the grain boundary; (b) the equivalent strain introduced by the tribological loading using different grain / twin boundaries. The results were acquired in a bronze disc running against a Ni pin.

1.4 Surface chemistry change during tribological loading

Among the different tribolayers in the last section [33, 49, 53, 54, 56-58, 63, 64, 70], the most important one is the top layer; not only because it is the material determining the level of friction force, but also because it is the layer where wear is generated [96]. In conjunction with research on thin films and surface coatings [131, 132], the tribological performance can be significantly improved by controlling the chemical and mechanical properties of this top layer [133].

Due to the potentially complex chemical composition of the tribological contacts (two contacting bodies and optional lubricants), significant local stress levels and uncertain local temperature, mechanically driven chemical reactions may happen during the contact exactly at the top layer. The sliding then results in products with significantly different mechanical properties as well as different chemical compositions [49]. If the surface layers are much harder and stiffer than the bulk material underneath, cracks and layer detachment can easily

occur and high friction and more wear will likely be generated on the surface [134], e.g. the high friction regime between pure metals like pure aluminum and stainless steel [135]. In mechanically softer tribologically induced surface layers, a certain amount of the sliding energy will be dissipated to grow and plastically deform the tribolayers [73]. Plastic deformation is, thus energy-wise, a competition to the generation of wear particles. In such cases, it is less likely to generate cracks inside the top or between different layers [136], eventually leading to reduced wear. This is for example why silicon is often added to aluminum alloys in order to build up a softer silicon-rich top layer for improving the friction and wear performance [137] (Figure 1.12). Another example can be found in the application of lubricous oxides in high temperature environments [138].

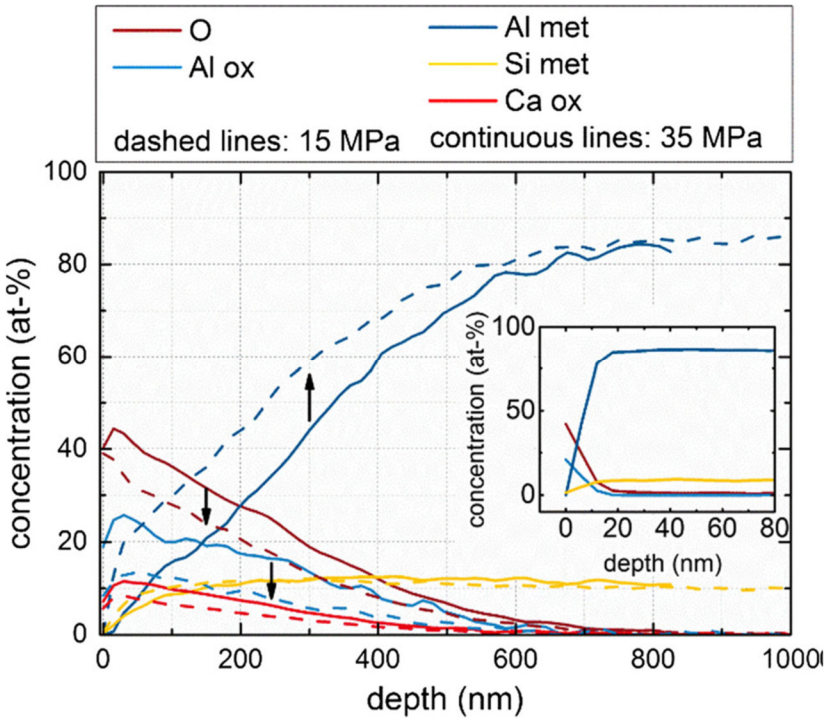

Figure 1.12: Chemical composition depth profile of the tribo-layer formed in aluminum-silicon alloys using X-ray photoelectron spectroscopy (XPS). Comparison of the depth profiles of metallic and oxidized Al, O, Ca, and Si measured by XPS on the worn surface created with a 15 MPa and 35 MPa contact pressure. The inset shows the depth profile of an unworn disk [137].

Surface chemistry holds the same importance as the materials' microstructure. The region of interest and the elementary mechanisms are very often different from the ones in single asperity contacts and subsurface microstructure problems. Yet the surface chemistry is critical to the tribological performance. The pathway for the development of a chemically different top layer yet is elusive. Once these mechanisms are understood, they will allow for surface engineering and superior tribological performance, and will eventually be a major boost to energy efficiency.

1.5 A summary and this thesis' mission

It has to be pointed out that many works aimed for improving the performance of the tribological systems by tuning the materials microstructure but only very few of them paid attention to the mechanisms for this improvement. This is due to a huge lack of fundamental knowledge in the field. It is true that the research in an aspect of basic science does not lead to an immediate improvement in a product's performance. Rational designing of tribosystems (in terms of being able to describe, model, predict and tune the tribosystems) and revolutionary improvements in the performance can, however, only be achieved with a profound understanding of the elementary mechanisms.

Due to the differences in testing methods (i.e. different contacting modes and test environments) and materials (i.e. different initial microstructures), comparing results between different works is currently almost impossible in tribology. This is why there is still no systematic understanding to the mechanisms for the microstructural changes under tribological loading, and why a systematic investigation in the field is urgently called for.

The microstructure in metals under tribological loading has been observed, yet only at certain loading conditions and certain stages of the sliding contact. Organizing the literature review chronologically in terms of following different stages of tribological loading (from early to intermediate to late stages of the sliding contact) has been attempted but it was found very

difficult, because the existing works mainly focus on the late stages of the sliding contact. Very little or even no attention has been paid to the microstructural changes in the very early and the intermediate stages of the sliding contact.

This is the point where the work in this thesis comes in, embarking on filling this gap by a systematic investigation of the microstructure evolution under tribological loading. The mission is to identify and to characterize the elementary processes in the subsurface microstructure evolution under tribological loading through different (especially the early) stages of the sliding contact and to understand the mechanisms for tribologically induced microstructure evolution.

Chapter 2: Materials and methods

2.1 Materials and sample preparation

The main sample material investigated in this thesis was oxygen-free high conductivity (OFHC) copper. Copper was chosen because as a ductile metal with a face-centered cubic (fcc) lattice structure, the dislocation activity during plastic deformation is well studied in various loading conditions [112, 125, 139-142]. The counter body was a sapphire sphere. Sapphire's hardness is only second to diamond [143]. It has proven to be chemically inert during tribological loading [143] and does not participate in the mechanical mixing in contact with copper in my experiments [70]. This has been a perfect pair of materials for this thesis' investigations to the microstructure evolution under tribological loading. Even though it is associated with a complex 3D stress field [25], a spherical counter body was chosen as it allows for a defined contact area. It was also expected that in engineering applications, involving tribological loading, complex stress fields would be encountered, making a sphere-on-plate contact a good model system.

Sapphire spheres with a diameter of 10 mm were provided by SWIP (Bruegg, Switzerland). OFHC copper plates (Goodfellow, Friedberg, Germany) with a purity higher than 99.95% were annealed in a vacuum of 1.5×10^{-6} mbar for 2 h at a temperature of 500 °C. The residual stress in the sample was eliminated during the annealing process and randomly oriented grains with a homogeneous grain size of 30-40 μm were obtained in all the samples (see Appendices Figure A2). The plates were then left inside the furnace under vacuum to cool down to room temperature (with an average cooling rate of 80 K/h). The annealing process was followed by grinding with SiC paper of #800 down to #4000 grid. Mechanical polishing was carried out with a 3 μm diamond suspension for 5 min and with a 1 μm diamond suspension for 8 min (both DP-suspension M products were from Struers, Willich, Germany).

The samples were then electro-polished in D2 electrolyte (Struers). The electro-polishing step was performed using a voltage of 24 V and a flow rate of 12 (calibration parameter to the machine), at 22 °C, for 20 seconds. Right before testing, the samples were sonicated in isopropanol for 15 min. This sample preparation process was developed in order to yield a reproducible surface chemistry and an initial microstructure with the least initial defect density possible (as verified by FIB and TEM, see Figure 3.2a). This initial microstructure was of crucial importance because the microstructure evolution can only be reasonably interpreted with a clearly known initial state. In the literature, characterization of the initial microstructure before tribological loading is often missing. This, on the one hand, led to a lack of knowledge of microstructure change in the very early stage of tribological loading and on the other hand, it made the comparison of the results between different works virtually impossible. Using the initial microstructure as a solid reference, all the microstructural features observed later in the subsurface area in this thesis can and will be interpreted as the results from the tribological loading, instead of the sample preparation.

Experiments using materials other than OFHC copper and sapphire sphere were also performed specifically to test the generality of my results. Cu-5wt.%Zn alloy (Wieland-Werk AG, Ulm, Germany) and pure nickel with a purity >99.99% (Goodfellow) were chosen as additional materials to be tested. The sample preparation method for both materials was very similar to that for the copper samples, and only the differences are described as follows: The annealing temperature for the Cu-5wt.%Zn alloy was 550 °C and for pure nickel 750 °C. For nickel, a second annealing step after mechanical polishing was followed by the final electro-polishing in A2 electrolyte (Struers). This allowed eliminating microstructural defects introduced during the mechanical polishing as well as removing any oxidation on the sample surface. Cerbec® silicon nitride (Si_3N_4) spheres with a diameter of 10.31 mm were provided

by Saint-Gobain Ceramics (Connecticut, USA) and used as a counter body containing no oxygen in contrast to sapphire spheres (Al_2O_3).

2.2 Tribological experiments

A reciprocating linear tribometer [144] was used for the sliding experiments (Figure 2.1a). A detailed schematic diagram demonstrating the sample setup and the position of the microstructure observation is presented as the diagram in Fig. 2.1b. The relative motion in this thesis was in two modes: pass and cycle. The pass mode refers to unidirectional motion (Fig. 2.1c) of the counter body on the sample surface. The cycle mode refers to reciprocating motion. The counter body going forth and back by two stroke lengths in total is one cycle. The sliding distance for a pass is half of that for a cycle. Multiple pass or cycle is the repetition of the one pass or cycle. Whenever an experimental parameter was changed, a new wear track on a physically different position on the sample surface was produced. A new sapphire sphere was used for each test, so that a previous test could not influence the next one through sharing the same counter body. For example, the worn copper, if there was any, transferred to the sapphire sphere during one test would not be carried to the next wear track. The copper samples were plates in size of 12 × 25 × 5 mm^3, allowing for three or four wear tracks on each sample without them interfering with each other. To describe the sample orientation and the view of the microstructure observation, the z-axis was defined as the sample surface normal, and the x-axis was defined as the initial sliding direction (Fig. 2.1b).

The experiments in this thesis were designed as simple as possible, in order to understand the elementary mechanisms for the microstructure evolution under tribological loading. In each set of experiments, only one parameter was changed and all the others were kept constant in order to keep a systematic investigation on the effect of that changed parameter.

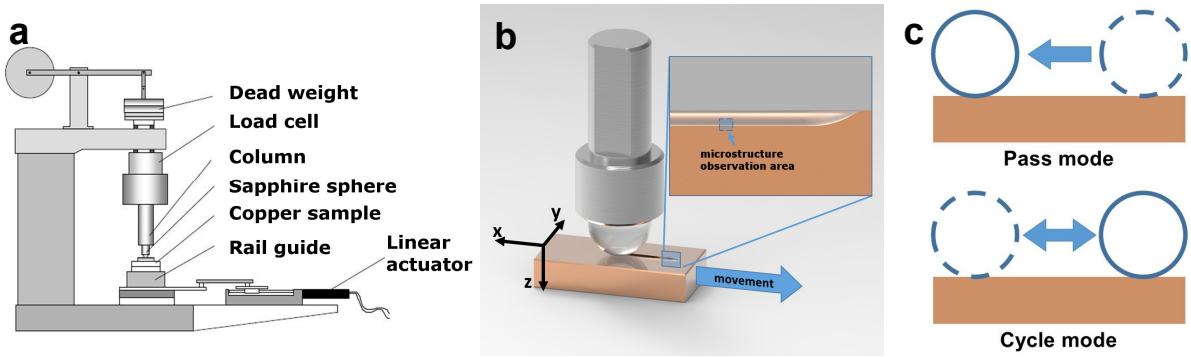

Figure 2.1: Schematic diagrams of the experimental setup. (a) Schematic diagram of the tribometer set-up used in the tribological experiments [144]; (b) Diagram of the sample setup as well as the position of the microstructure observation. A sapphire sphere (10 mm in diameter) was moved over the surface of an annealed OFHC copper sample under a mild normal load. Microstructure observation was typically performed on the cross-sectional area in x-z plane (cross-sectional view along the sliding direction in the blue rectangle in Fig. 2.1b), if not mentioned specifically [145]; (c) Diagram of the two motion modes: the upper diagram is the pass mode and lower one is the cycle mode.

The experiments started at the very early stage with the simplest tribological test: only one sliding pass of a sapphire sphere on the OFHC copper surface. The normal load was 2 N with a corresponding Hertzian pressure of 530 MPa using a Young's modulus of copper (117 GPa) and sapphire (345 GPa) and a Poisson ratio of copper (0.34) and sapphire (0.3). This relatively small (compared to the majority of the works in the literature) normal load allowed to focus on the microstructure changes induced by friction, instead of by ploughing. The sliding speed was as low as 0.5 mm/s so that there was not expected to be a noticeable temperature rise during sliding. The material's response to the temperature change could thus be neglected. The stroke length was 12 mm, such that on the one hand, there were enough grains in the wear track to have sufficient statistics, and on the other hand a stable sliding speed could be acquired in the most part of the wear track (considering the stage accelerated and decelerated near the two dead centers). The tests were conducted at room temperature

and in air with 50% relative humidity to approach to a controlled contact condition. No lubricant was applied in order to maintain a defined and simple contact environment.

Through different sets of experiments, two key parameters were changed in this thesis: the normal load and the sliding cycle / pass number. The sliding cycle number was changed in order to investigate different stages of the sliding contact. The normal load was changed in order to systematically change the stress magnitude and distribution in the samples.

- The normal load was changed in a range of 0.5 N, 1 N, 2 N to 14 N. The Hertzian contact pressures [25] were calculated for the above mentioned normal loads, which were 334 MPa, 420 MPa, 530 MPa and 1014 MPa, respectively. This elastic model was, in theory, not a proper fit for a precisely quantified prediction of the stress level under the contact, yet it still gives us a satisfying estimation of the stress distribution in the materials.
- The sliding cycle / pass number was changed to cover different stages of the sliding contact. Two types of motion were applied as the sliding distance increased: unidirectional multiple pass (referred to as “sliding pass number”) and reciprocating cyclic loading (referred to as “sliding cycle number”). The unidirectional pass numbers were 1, 2, 4, 6, 8, 10 to 20 and reciprocating cycle numbers were 1, 10, 100, 500, 1000 to 5000. The total sliding distance of 20 passes of sliding were equivalent to 10 cycles of sliding, only differing in sliding direction.

To specifically investigate the surface features during the tribological experiments, the normal load was set on 1.5 N for one set of experiments. The generation of wear was expected to be even less than the experiments using 2 N normal load, where wear has already been expected not significant, so that the focus was on the chemical and microstructural changes due to friction. All the other aspects of the experiments were kept exactly the same as the ones in the other experiments, in order to keep the work systematic.

Experiments under other conditions were not a major part of this thesis. They yet offered results of critical importance and stimulated valuable discussions. To explore the generality of my results in the single sliding pass experiments, single sliding pass tests were performed with different materials (Cu-5wt.%Zn brass alloy and pure nickel) and even with a different counter body (Si_3N_4 spheres). To track down the source of the oxygen in the oxide formed on the sample surface, experiments were performed in a dry nitrogen atmosphere to check if the oxygen in the surface oxide was from the sapphire (Al_2O_3). The chamber of the tribometer was flushed with dry nitrogen for one hour before the experiment. The relative humidity dropped below 10 %, which was the limit of the measurement device (from Greisinger electronic, Regenstauf, Germany). The dry nitrogen flow was kept during the whole experiment to guarantee a stable environment. A different counter body (Si_3N_4 sphere) was used to perform experiments in air to check if the oxygen in the surface oxide was from the air or the counter body.

2.3 Methods for microstructure investigation

The microstructure was observed in a cross-sectional and in a plan view. If not specifically mentioned, the microstructure observation was performed in the cross-section along the sliding direction (x-z plane, sample reference see Fig. 2.1b). Observations in x-y plane were also performed to reveal more microstructural information in the subsurface area.

The microstructure was examined using a focused ion beam / scanning electron dual beam microscope (FIB/SEM), (Helios NanoLab™ DualBeam™ 650 from FEI, Hillsboro, Oregon USA). Before the preparation of a cross-section or a TEM lamella, the surface of the area of interest was always protected from ion beam damage by depositing two platinum layers, the first one with a thickness of 0.26 µm employing the electron beam only, with an acceleration voltage of 2 kV and a beam current of 6.4 nA, the second layer with a thickness of 1.5 µm using the ion beam with an acceleration of 30 kV and a beam current of 0.77 nA. Cross-

sectional SEM images were taken to observe the thickness of the tribologically deformed layer, with an acceleration voltage of 2 kV and a beam current of 0.8 nA. A state of the art FIB lift-out technique with little ion beam damage was applied to prepare the (S)TEM lamellae for this study [146]. With a scanning transmission electron microscopy (STEM) detector installed on the FIB/SEM system, images with transmission electrons were available with an acceleration of 30 kV and beam currents of 50 pA and 100 pA. Transmission electron microscopy (TEM) was performed for detailed subsurface microstructure in both cross-sectional and plan view areas (using a FEI Titan^3 80-300 TEM, Hillsboro, Oregon USA, with a 300 kV acceleration voltage). The details of the subsurface chemistry were investigated with a FEI Titan^3 G2 80-300 TEM (Hillsboro, Oregon USA), using an acceleration voltage of 300 kV. STEM and energy-dispersive X-ray spectroscopy (EDXS) were performed together to map the chemistry in the subsurface area. When combined, a focused beam of about 1 nm diameter is scanned across a predefined area and for each pixel of the scan field, an EDXS spectrum is recorded. Within 15 to 50 minutes, 3D datasets (x and y spatial and y photon energy coordinates) are acquired. High-resolution TEM (HRTEM) was performed for detailed microstructural investigation with atomic resolution. Bright field (BF), dark field (DF) and high-angle annular dark field (HAADF) imaging modes were applied to acquire different contrasts. Selected area electron diffraction (SAED) was performed to compare the crystallographic orientations in different areas.

Electron backscatter diffraction (EBSD) on the cross-sectional area was performed using a lift-out technique similar to that for STEM sample preparation [71] with a sample thickness of 1 μm. This remarkably increased the pattern quality for the cross-sectional area compared to EBSD performed on volume material. EBSD on a FIB prepared cross-section without lift-out was geometrically inappropriate for my samples. The bulk sample was blocking the diffraction signal leading to Kikuchi patterns in poor quality. EBSD on a cross-section of the

bulk material prepared via mechanical polishing was extremely challenging for this work, because the microstructure observed in this thesis was induced by a friction force, and artifacts were foreseen to be introduced by mechanical polishing.

The cross-sectional EBSD scans were performed on a 70 ° pre-tilted surface with acceleration voltages of 25 kV and 30 kV and beam currents of 3.2 nA and 6.4 nA. The step size was 200 nm for cross-sectional EBSD, a commonly used step size in recent years [147]. The Kikuchi patterns were acquired by the detector NordlysMax^2 and were indexed by the software AZtecHKL (both, Oxford Instruments, Oxfordshire UK). EBSD mapping analysis was carried-out with MTEX, a well-developed Matlab toolbox for texture analysis [147, 148].

Transmission Kikuchi diffraction (TKD) was performed to acquire crystallographic orientation information in cross-sectional areas with a higher spatial resolution. As the samples for the TKD measurements in general had the same thickness as the ones for TEM, they were electron transparent. Due to the small thickness of the sample, the diffraction patterns are thus generated from a much smaller volume of material compared to conventional EBSD. This in theory allows for a much higher spatial resolution with a scanning step size down to 2 nm [149] with the regular beam spot size of SEM. However, it is known that the step size plays an important role in the estimation of the misorientation measured as the density of geometrically necessary dislocations [150]. A step size of 20 nm was chosen for the TKD measurements of this thesis to guarantee reliable results with enough spatial resolution and a sufficiently low level of artefacts caused by contamination. TKD measurements were performed with a setup almost the same as that for the conventional EBSD measurements in the FIB/SEM DualBeam microscope. The working distance in this method was 1 mm in order to bring the diffraction pattern center to the center of the phosphorous screen of the EBSD detector. The lamellae were prepared the same way as a TEM lamella (lift-out in the center of the wear track). Unlike the sample position for

conventional EBSD (pre-tilted by 70°), TKD lamellae were placed with a pre-tilt angle of -20°, with an in house manufactured sample holder. The diffraction pattern indexing was automated by AZtecHKL (Oxford Instruments). The recent version (AZtec 3.1) provided a solver setup specifically optimized for TKD, which yielded more reliable indexing results compared to the solver for conventional EBSD. Scans were taken near the surface on cross-sectional areas of 2.2 × 3 µm². The misorientation was determined by comparing all pairs of points with the same horizontal and different vertical positions (results will be shown in detail in Chapter 3).

From the cross-sectional area EBSD and TKD data, the local orientation changes can be interpreted as an estimate for the density of geometrically necessary dislocations (GND). The GND density analysis can expose microstructural features which are introduced by a non-uniform deformation during sliding [151, 152], like the beginning of plasticity related changes in the microstructure. Following Gao et al. [153, 154], the GND density ρ_{GND} was calculated directly from the misorientation angle ϑ irrespective of grain orientation:

$$\rho_{GND} = \frac{2\vartheta}{ub}, \tag{5}$$

where u is the distance between the two points used to calculate the misorientation and b the length of the Burgers vector of a $\frac{1}{2}\langle 110\rangle$ dislocation, which is 0.255 nm for copper. This method assumes a cube with an edge length of u and each (edge type) GND in this cube will stretch one edge with the length of one Burgers vector. The so-defined GND density can then be correlated with a misorientation tilt angle, regardless of slip system [147]. This angle is calculated as the average of misorientation angle comparing the orientation of each pixel in the map with its neighboring four pixels. Even though this method might appear like a simple estimation, its results are very similar to those from a more thorough analysis [154].

As far as the angular resolution limit of the EBSD and TKD measurements is 0.08° (technical limit of the NordlyMax^2 EBSD detector), the lowest GND density which could be detected

with this method is thus 5×10^{13} m^{-2} [155]. This limit also describes the minimum error of the GND analysis [155]. Another limitation of the cross-sectional EBSD and TKD measurements is that these methods cannot provide statistically reliable results due to the limited area of scans.

Chapter 3: Results

This chapter will focus on presenting the results of this thesis; the discussion will be concentrated in Chapter 4. The results are presented starting with the microstructure observation in the very early stages of tribological loading, followed by the intermediate and late stages' microstructure changes. A whole picture of the microstructure evolution will be revealed together with the surface oxidation characterization. In this thesis, the very early stages are referred to as the sliding distance equal or smaller than ten reciprocating cycles (or 20 unidirectional sliding passes). The intermediate and late stages of sliding is typically referred to as from ten to 5000 reciprocating cycles.

If not specially mentioned, the experiments were performed using OFHC copper sliding against sapphire spheres and the subsurface microstructure was observed in the cross-sectional view along the sliding direction (x-z plane in Fig. 2.1b).

3.1 Friction force and wear track characterization

The friction force and wear track profilometry is presented to show the level of friction force as well as the reproducibility of the experiments. It is necessary to present these data, yet they will not make a key point in the discussion, since the focus of this thesis is on the microstructure evolution in the material under tribological loading. Figure 3.1 shows the friction forces in the representative experiments in this thesis (Fig. 3.1a+b) as well as the wear tracks' profilometry (Fig. 3.1c+d). The friction forces for one sliding pass experiments are difficult to obtain, however, the data suggest that the friction coefficient is around 0.25. The tribological conditions were chosen particularly mild, not to plough the surface and not to cause any material loss from the surface (depth profiles of each wear track are presented in Fig. 3.1c+d). No loose wear particles were observed after any of these tests.

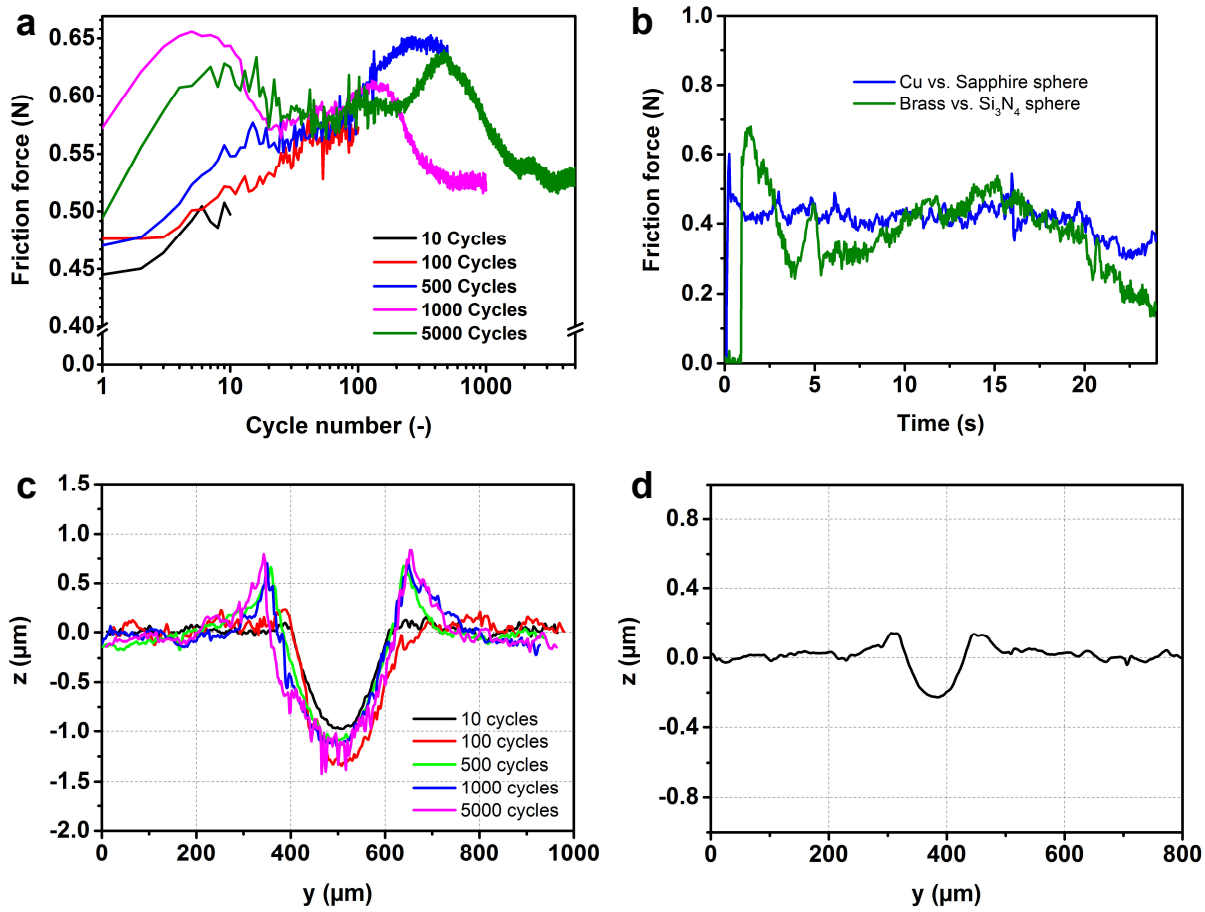

Figure 3.1: Results of friction forces and profilometry of the wear tracks from different tribological experiments. (a) Mean values of friction force measured in each sliding cycle plotted against the cycle number. OFHC copper samples were sliding against sapphire spheres with a normal load of 2 N in air without any lubricant. The results show a typical running-in effect; (b) Friction force in single pass sliding experiment with a normal load of 2 N; (c) Depth profiles measured in the middle of each wear track. Z-axis is the surface normal and x-axis (out of paper) is the sliding direction; (d) Depth profile of the wear track after a single sliding pass under 2 N normal load. Note that the z-axis scale is different between panel (c) and panel (d).

3.2 Microstructure observation for very early stages of sliding contact

At the very early stage of friction loading, single pass, one cycle and multiple pass experiments were performed. For single pass experiments, the normal load and the material

were changed in different sets of experiments. For multiple pass / cycle experiments the normal load was fixed as 2 N. As the features observed here are very close to the surface (at a depth of within 200 nm), it requires a high spatial resolution to characterize them. Most of the results in this section is thus acquired via (S)TEM.

3.2.1 Transmission electron microscopy in the subsurface area

Cross-sectional STEM images are shown in Figure 3.2 for the undeformed sample (Fig. 3.2a) and the single sliding pass experiments at different normal loads (Fig. 3.2b-e). Figure 3.2a shows no sign of prior microstructure modifications at the surface, demonstrating the quality of the sample preparation technique.

In the cross-sectional STEM image for 0.5 N normal load (Fig. 3.2b), a sharp line contrast is observed at a depth of 120 ± 8 nm beneath the surface. This sharp line feature is later interpreted as a trace of dislocations left in the subsurface area by the sliding pass(es) of the sapphire sphere on the copper surface – effectively a trace of dislocations - and henceforth referred to as the "dislocation trace line" or simply the "trace line". The depth of the trace line is measured by taking five points on the line and averaging their distance to the surface along the sample's surface normal (z-axis). The area above the trace line appears clearer, whereas the area below shows a darker contrast. For the wear tracks with higher normal loads (Fig. 3.2c+d), the depth of the trace line does not show an obvious change. When the normal load is increased to 14 N (Fig. 3.2e), two trace lines are observed. The one closer to the surface is at a depth of 90 ± 4 nm.

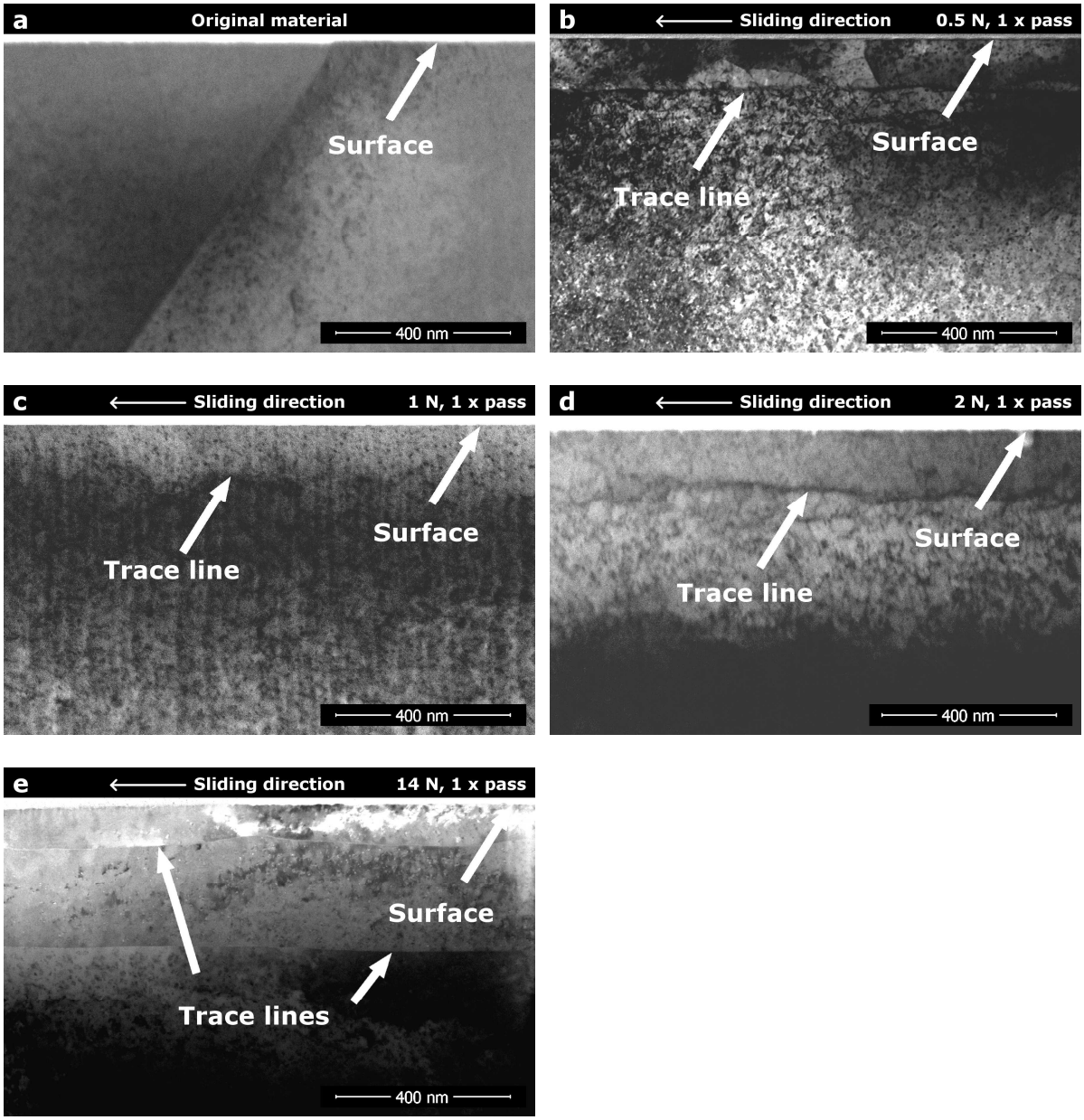

Figure 3.2: STEM cross-sectional images of OFHC copper under a single pass tribological load with four different normal forces. (a) Original material before tribological loading; (b) 0.5 N load; (c) 1 N load; (d) 2 N load; (e) 14 N load. All lamellae were prepared perpendicular to the sliding surface (cross-sections) and along the sliding direction (x-z plane in Fig. 2.1b). The bright contrast at the very top of the images is caused by the protective platinum layer. The sample's surface and the trace line are marked by white arrows.

To further identify the dislocation structure in the trace line, HRTEM was performed on a trace line after 2 N single pass loading (results see Figure 3.3). The sample is different to the

one used for STEM imaging in Fig. 3.2d. In Fig. 3.3a, the trace line is observed at a depth of 114 ± 8 nm. The zone axis of the image is [103], as determined from the fast Fourier transform (FFT) image of the area beneath the trace line (see bottom right corner of Fig. 3.3b). The most visible atom planes in Fig. 3. 3b are (100) planes, which have been rotated towards the sliding direction by an angle of 7.9 ° (marked as α in Fig. 3.3b) at the position where the trace line appears.

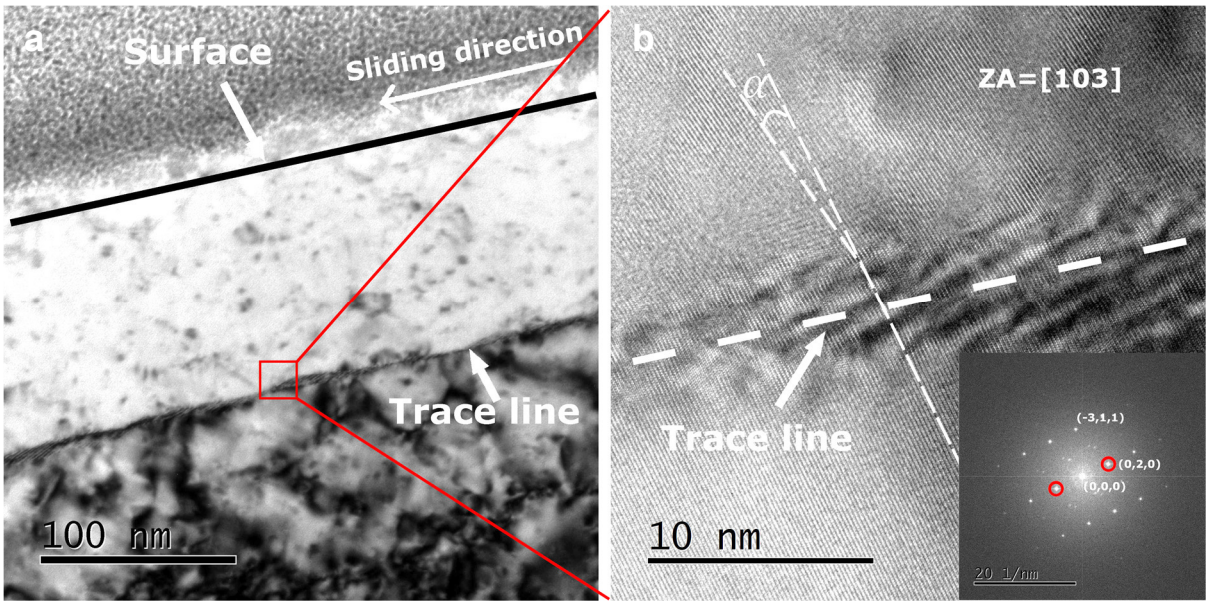

Figure 3.3: (HR)TEM cross-sectional images of OFHC copper under a single trace tribological load of 2 N normal load [156]. (a) TEM bright field image; (b) HRTEM image of the trace line in the red rectangle area in (a), with the fast Fourier transform (FFT) image of the lattice beneath the trace line in the right-bottom corner (available enlarged, see Fig. A3). An inverse-FFT is perfromed using only the two spots marked by the red circles.

To investigate the evolution of the trace line with further loading, unidirectional multiple sliding pass tests with 2 N of normal load in a second set of experiments were conducted (see Figure 3.4). The depth of the trace line remains around 120 nm until ten passes (Fig. 3.4a-c). After ten passes (Fig. 3.4d+e), two trace lines appear. The trace line closer to the surface shares the same feature as the trace line in the experiments with lower pass numbers (Fig.

3.4a-c). The trace line which is deeper is not as sharp and as straight as that shows up under 14 N single pass loading. The depth of the trace line is plotted in Fig. 3.4f.

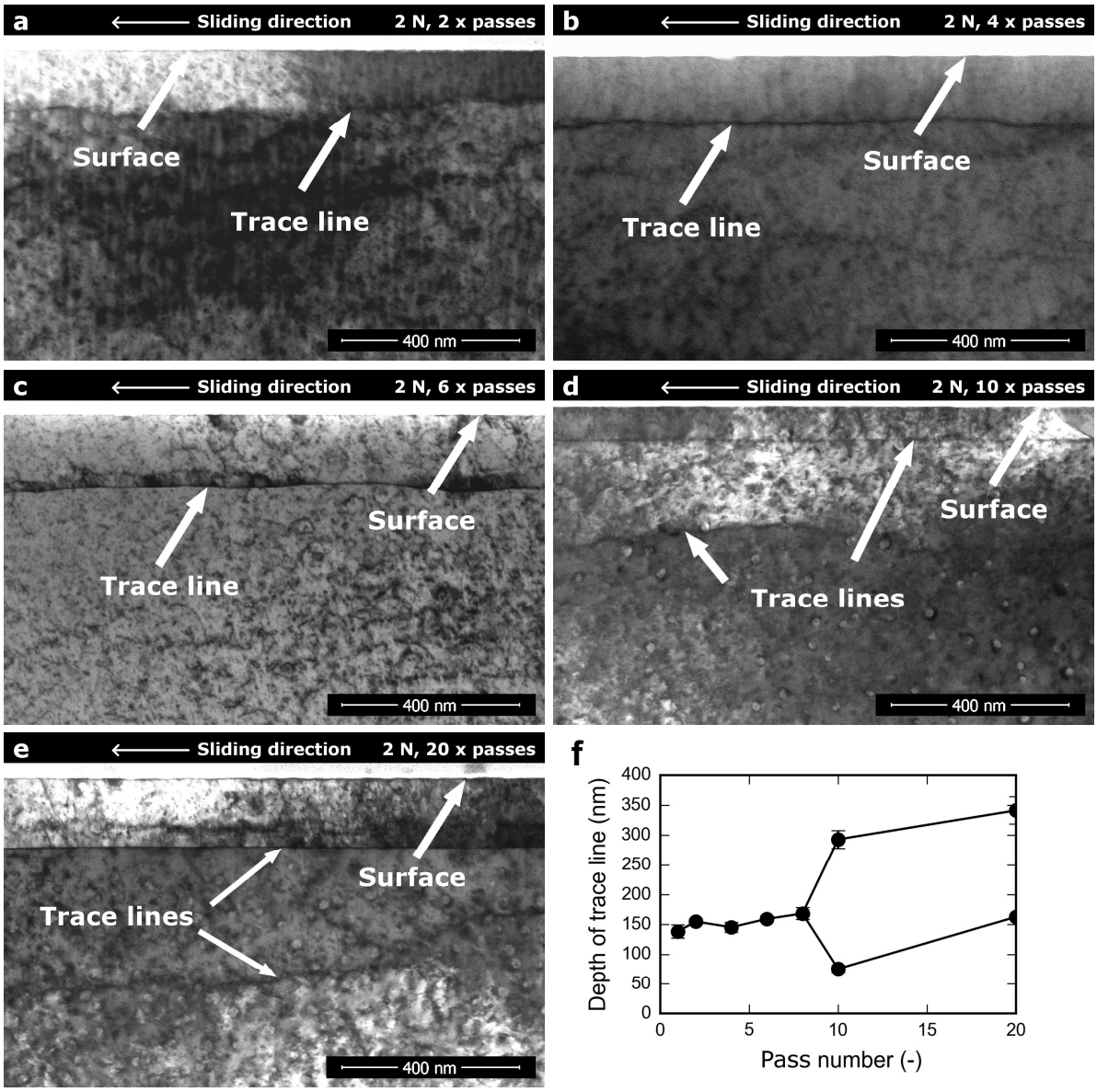

Figure 3.4: STEM cross-sectional images of OFHC copper under a linear multi-trace tribological load with seven different pass numbers and 2 N of normal load. (a) 2 passes; (b) 4 passes; (c) 6 passes; (d) 10 passes; (e) 20 passes; (f) The depth of the trace line(s) plotted against the number of passes. The lamellae were prepared perpendicular to the sliding surface (cross-sections) and along the sliding direction. Sample surfaces and trace lines are marked by arrows.

3.2.2 Transmission Kikuchi diffraction on the dislocation trace line

To determine whether the trace line is associated with any crystallographic misorientation, TKD scans were taken above and below the trace line on cross-sectional areas of 2.2 × 3 μm² (Figure 3.5). The samples for TKD measurement are different to the ones used for STEM and HRTEM. The color of each pixel in the maps in Fig. 3.5 represents the number of geometrically necessary dislocations per square meter (GND density). Yet as described in Chapter 2, the GND density is obtained from the misorientation angle of each pixel through a simple, and efficient model. The GND density maps thus are essentially misorientation maps. The trace line is visible as the feature with high GND density or the non-indexed pixels. The appearance of multiple trace lines under 14 N normal load (Fig. 3.2e) can also be observed in TKD results (Fig. 3.5c).

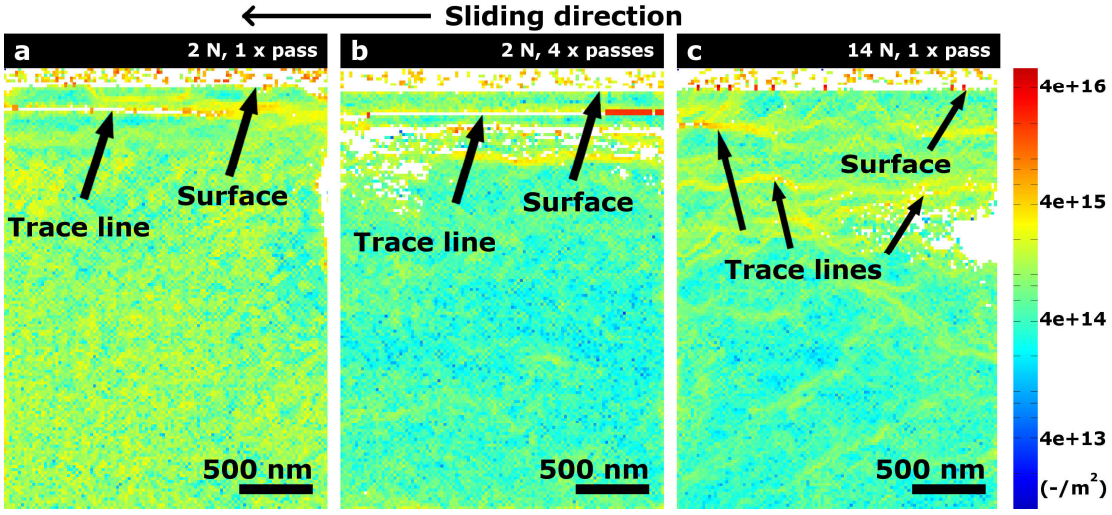

Figure 3.5: Geometrically necessary dislocation (GND) density analysis of OFHC copper in contact with a sapphire sphere. (a) 2 N normal load, single pass loading; (b) 2 N normal load, four passes loading; (c) 14 N normal load, single pass loading. The color bar for the GND mapping is in number of GNDs per unit area in m^2. The sample surfaces and the trace lines are marked by arrows. The lamellae were prepared perpendicular to the sliding surface (cross-sections) and along the sliding direction. The non-indexed and high GND density areas in (b) other than the dislocation trace line show up as features also parallel to the surface. They are, however, not visible in the STEM results (Fig. 3.4b) and therefore are not marked as dislocation trace line.

A TKD measurement on the sample after one reciprocating sliding cycle under 2 N normal load was performed. The trace line can be clearly seen in the STEM image as the sharp line feature (Figure 3.6a) with a high GND density (Fig. 3.6b). Pairs of points with the same horizontal position from 60 nm above and beneath the trace line are picked out to calculate the misorientation for 2 N normal load. The average misorientation value after one sliding pass is 4.6°, after four sliding passes 15.4° and after one cycle sliding 0.6°.

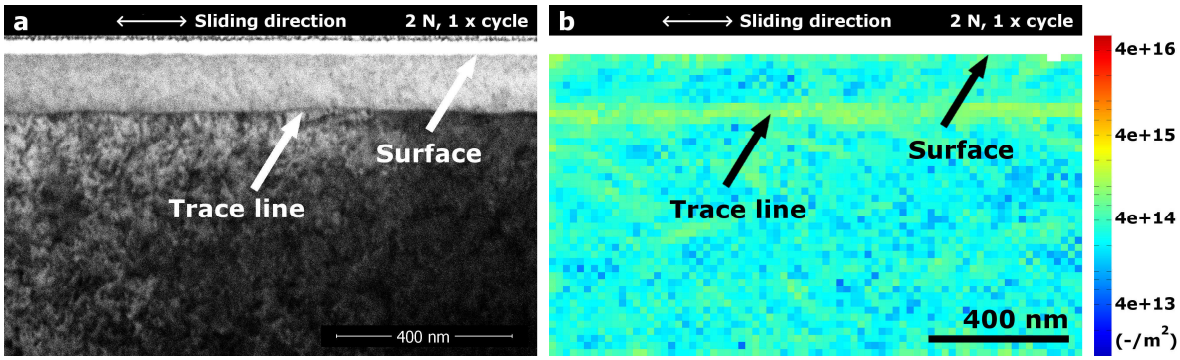

Figure 3.6: STEM result and GND density analysis on the microstructure after 1 reciprocating cycle of loading under 2 N normal load. (a) STEM image; (b) GND density map. The sample surfaces and the trace lines are marked by arrows. The lamellae were prepared perpendicular to the sliding surface (cross-sections) and along the sliding direction.

3.2.3 Plan view scanning transmission electron microscopy of wear tracks

The observation of the subsurface microstructure in a cross-sectional view (x-z plane) shows the trace line as a sharp line feature parallel to the sliding surface. To gain further insight into the 3-D microstructure of the trace line, plan view (in the x-y plane) STEM images of the area in question were taken.

The typical thickness of a TEM lamella prepared with FIB is around 50 nm. It is very challenging to prepare a lamella exactly at the position where the trace line can be "captured" (the trace line's depth is around 120-150 nm underneath the surface). Therefore, a lamella almost parallel to the sliding surface, but with an intended tilting angle to the surface (e.g. 3 ° and 5 ° along the y-axis) was cut using FIB. Inside such a lamella, material from

different depth is then covered. The microstructure of the trace line is captured in part of the STEM image.

Figure 3.7 presents two plan view (x-y plane in Fig. 2.1b) STEM images of two lamellae, both from a wear track under 2 N normal load after a single sliding pass. The lamellae were prepared with 3.10 ° (Fig. 3.7a) and 5.36 ° (Fig. 3.7b) to the sliding surface (tilt around y-axis in Fig. 2.1b), respectively. If the lamella is tilted a small angle only along the y-axis, the transition between the copper sample and the platinum layer (sample surface) should be a vertical line in the image. However, the uncertainty in rotation along the x-axis (sliding direction) leads to the non-vertical appearance of the sample surface in the STEM image in Fig. 3.7. The depth contour is marked by dashed white lines, indicating the material's distance normal to the sample surface (along the z-axis). From the right-hand side to the left-hand side, the material in the lamellae is from deeper positions from the sample surface. For both lamellae, from the surface to a depth of around 150 nm, the contrast (right side half of each image) shows sharp line features parallel to the sliding direction (some of these lines are marked by the arrows in Fig. 3.7). For each of these line features, as it goes deeper into the materials (towards the left-hand side in the image), the sharpness of the line suddenly gets less pronounced in contrast at a certain depth and eventually the line disappears completely when it goes even deeper. The depths where the sharp contrast of the line features end are analyzed for both lamellae presented in Fig. 3.7 and marked by white crosses. The average depth is found to be approximately 127 ± 14 nm and 136 ± 27 nm respectively.

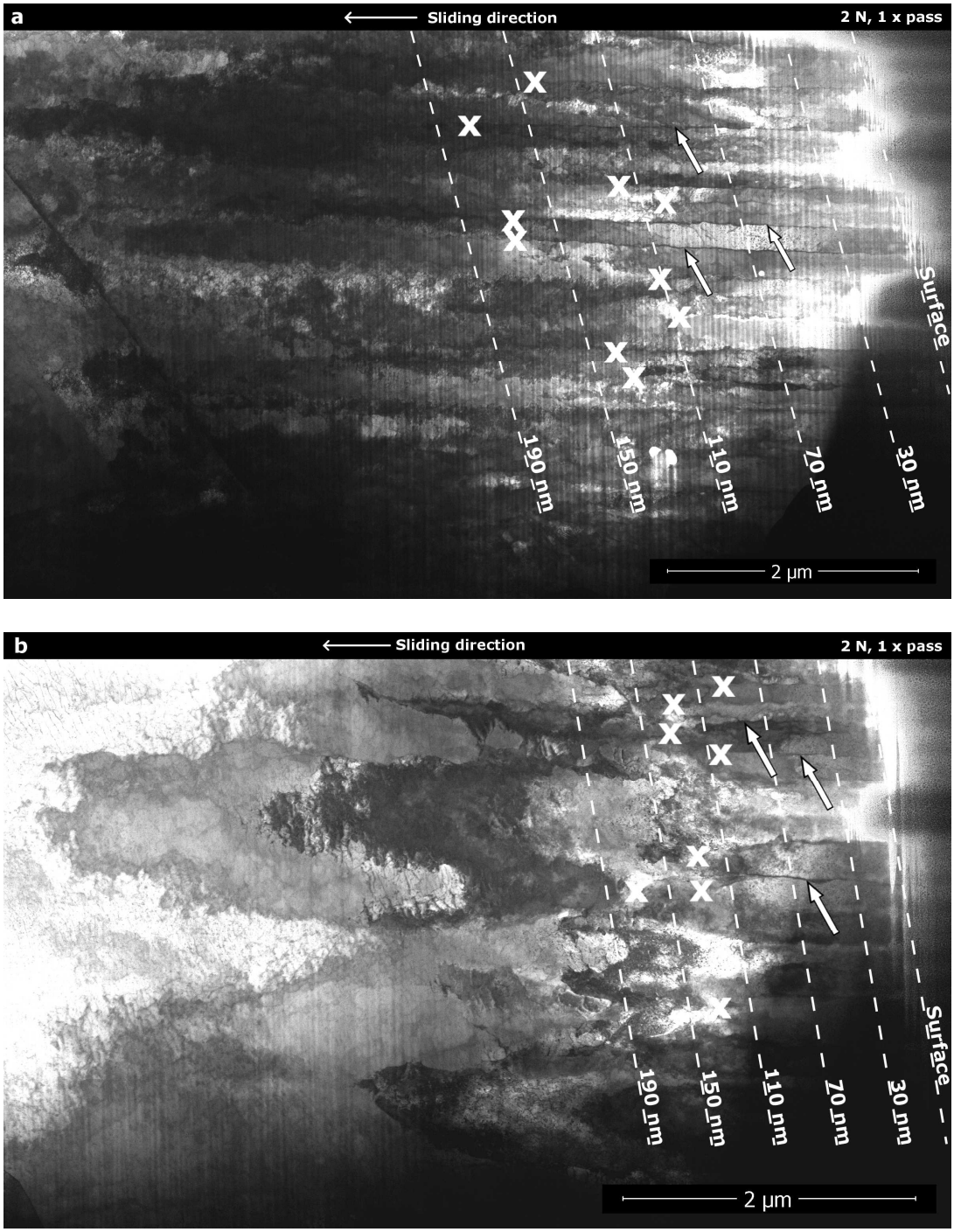

Figure 3.7: STEM in-plane images of OFHC copper under a single trace tribological load with 2 N normal load. The lamellae were prepared with a small tilt angle to the sliding surface: (a) 3.10 ° to the sliding surface, with a rotation of 0.83 °; (b) 5.36 ° to the sliding surface, with a rotation of 0.91 °. Sample surfaces and discrete depths into the material are marked by white dashed lines. Some of the sharp line features are marked by the white arrows. The ends of the sharp line feature parallel to the sliding direction are marked by white crosses.

The same lamella shown in Fig. 3.7a was investigated in TEM for greater microstructural details (see Figure 3.8). The line features (marked by white arrow in Fig. 3.7a) parallel to the sliding surface observed in STEM using an acceleration voltage of 30 kV is still visible in the TEM bright field image (Fig. 3.8a), now with a much higher acceleration voltage (300 kV). The SAED pattern of the imaging area in Fig. 3.8a is presented at the upper-right corner of Fig. 3.8a. The dark field image using the diffraction spot marked by the solid red circle in Fig. 3.8a is presented in Fig. 3.8b. The image appears clearly to have brighter and darker areas.

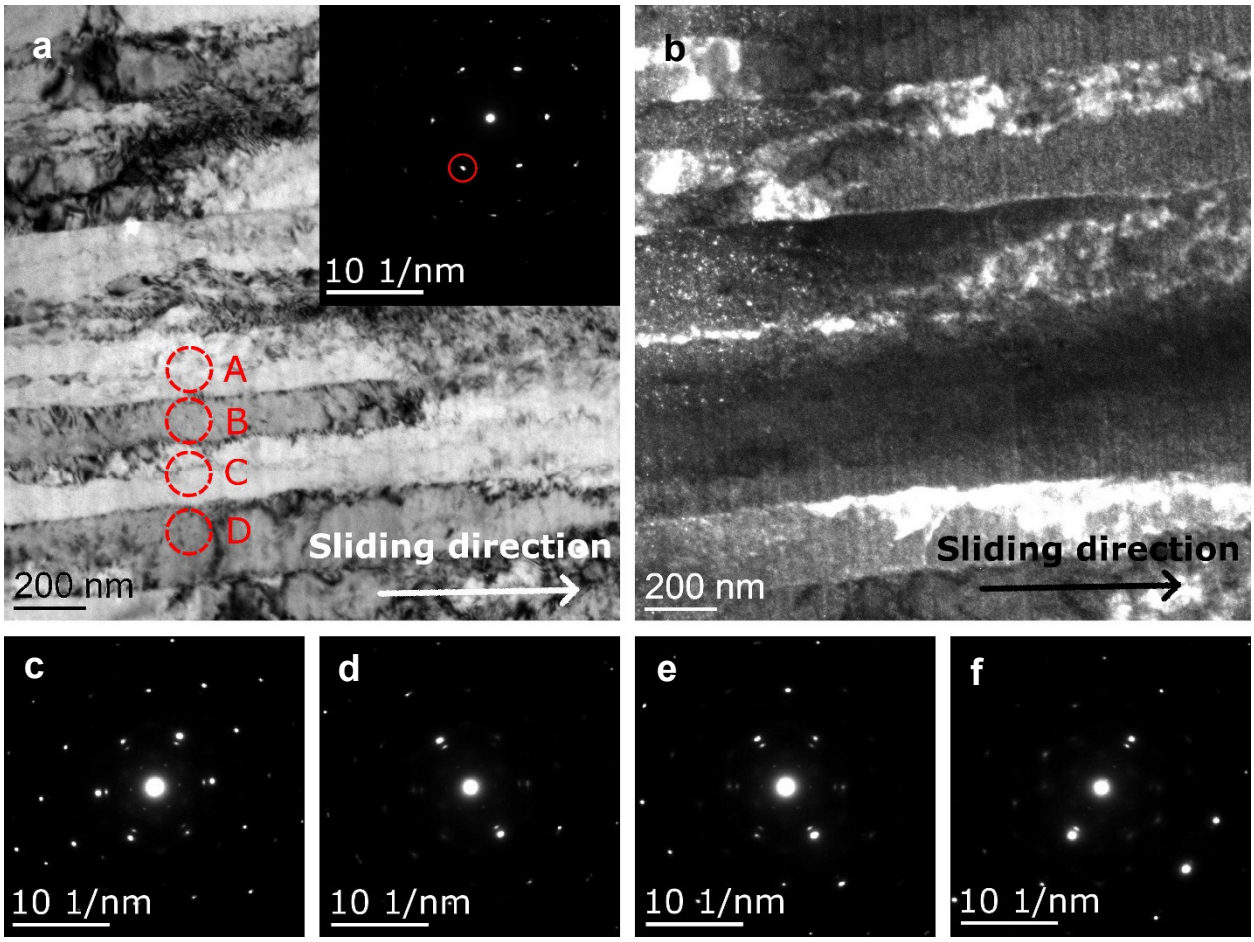

Figure 3.8: TEM plan view investigation of OFHC copper under a single trace tribological load of 2 N normal load [156]. (a) TEM bright field image, with the SAED pattern in the upper-right corner, taken in the zone-axis close to [111]; (b) Dark field image taken using the diffraction beam marked with the solid red circle in (a); (c-f) SAED pattern taken in the area A-D in (a) marked by dashed red circles in (a), respectively. The lamella is the same as the one in Fig. 3.7a, but in a horizontally flipped position, resulting in a sliding direction, marked by the arrows in (a) and (b), opposite to that in Fig. 3.7a.

A series of SAED measurements using the smallest aperture possible have been performed in four areas across three neighboring lines (areas A-D marked by the dashed red circles in Fig. 3.8a). Their SAED patterns are presented in Fig. 3.8c-f, respectively. From area A to B (Fig. 3.8c+d), the diffraction pattern changes its intensity on different spots, without obvious rotation; from area B to C (Fig. 3.8d+e), the diffraction pattern shows a small rotation (around 1.5 ° clockwise) and changes its intensity as well; from area C to D (Fig. 3.8e+f), the diffraction patterns appear to be in two different axes.

3.2.4 Dislocation trace line reproduced in different conditions

Dislocation trace lines have been observed in almost all the grains (34 out of 37 grains investigated) in the TEM lamellae that were randomly lifted out in the center of the wear tracks. Figure 3.9 presents a few cases where the trace line intersects with a grain boundary.

In most of the cases, the trace line goes through a grain boundary as if there is no grain boundary at all. For example, in a sample under 2 N normal load after two passes loading (Fig. 3.9a), the trace line's depth does not change in the two grains. The grain boundary is bent towards the sliding direction though. There are few cases where the trace line's depth is changed when going across a grain boundary. An example is given in Fig. 3.7b under 2 N normal load after ten cycles of sliding.

An extremely rare case is that the trace line appears in one grain and is cut off at the grain boundary. For example, in Fig. 3.9c after a single sliding pass under 2 N normal load, no trace line or other features can be observed in the left grain. A "nose" shape feature is formed at the grain boundary where the trace line is cut off and a very short boundary is formed going against the sliding direction.

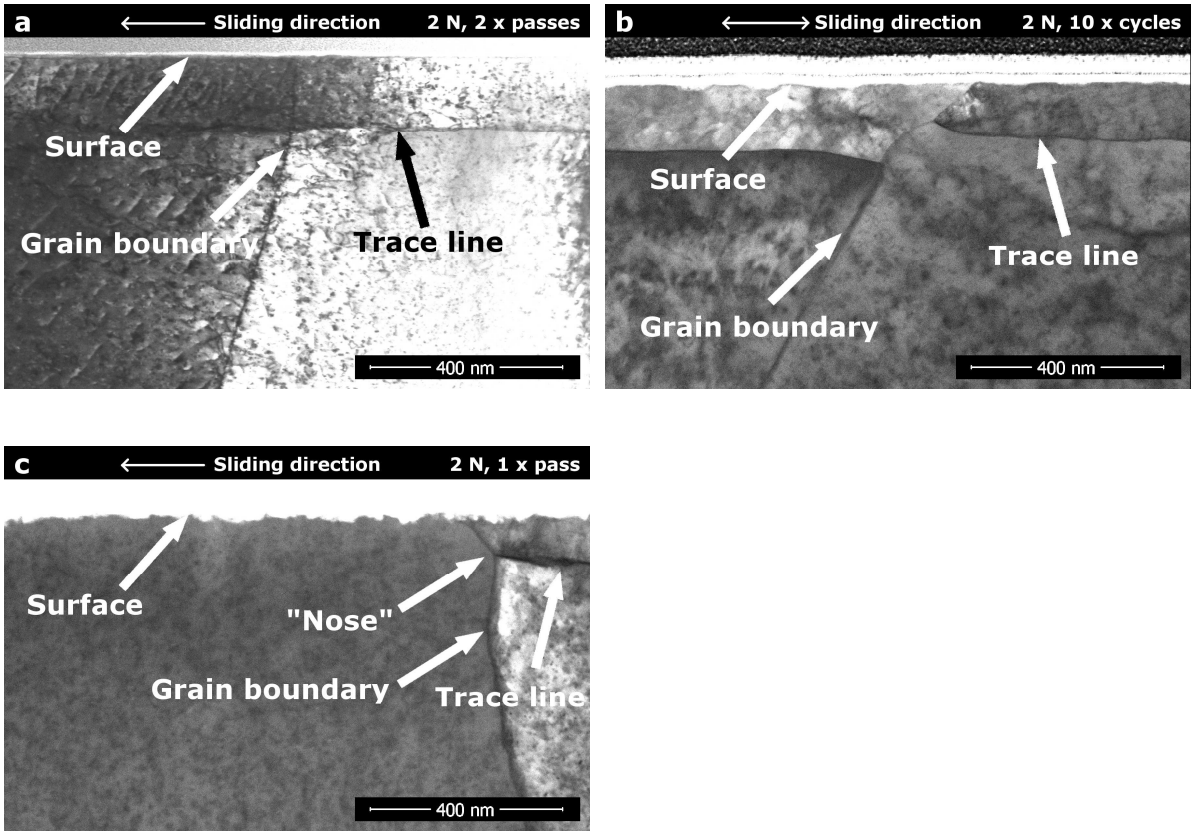

Figure 3.9: STEM cross-sectional images of OFHC copper under tribological loading. Three examples of dislocation trace line intersecting with grain boundaries. (a) Most common case, the trace line goes through the grain boundary without depth change, for example after 2 N, 2 passes loading; (b) Rare case, the trace line appears in both grains with different depths, for example after 2 N, 10 cycles loading; (c) Extremely rare case, the trace shows up in the right grain and stops at the grain boundary and does not appear in the left grain, for example, under 2 N normal load, after a single pass loading.

To investigate the generality of the appearance of the dislocation trace line, different materials for samples and counter bodies were used. Experiments of single sliding pass under 2 N normal load were performed using Si_3N_4 spheres running against α-brass alloy (copper containing 5 wt.% zinc) samples and sapphire spheres against pure nickel samples. The other experimental parameters were kept exactly the same as those for the OFHC copper samples. The results for these tests are presented in Figure 3.10. The dislocation trace line is observed

in both cases. It is located at a depth of 134 ± 13 nm in brass (Fig. 3.10a) and 138 ± 6 nm in pure nickel (Fig. 3.10b).

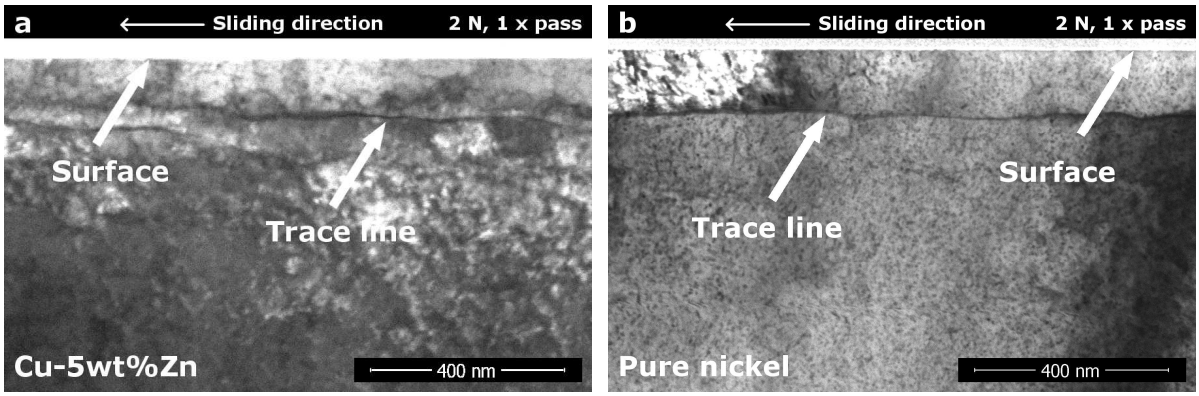

Figure 3.10: STEM cross-sectional images of the dislocation trace line under 2 N of normal load after single pass experiments in different materials. (a) Brass alloy containing 5 wt.% zinc run against a Si_3N_4 sphere [157]; (b) Pure nickel run against a sapphire sphere. The bright contrast at the very top of the images is caused by the protective platinum layer. The sample surfaces and the trace lines are marked by arrows.

3.3 Microstructure observation for intermediate and late stages of sliding contact

For intermediate and late stages, reciprocating linear cyclic sliding tests were performed. By only changing the sliding cycle number, the microstructure evolution is revealed for different stages of the sliding contact. The microstructure was examined from different aspects using different methods, for example, SEM, EBSD and STEM. A possible chemistry change on the sample surface was monitored at intermediate and late stages of sliding. TEM and EDXS results will be presented.

3.3.1 Scanning electron microscopy results on cross-sections with different sliding cycle numbers

FIB cross-sections were prepared in sliding direction in the middle of the wear tracks after all sliding cycles investigated (Figure 3.11) and also at the two dead centers of each wear track

(Fig. A4) to investigate the evolution of the deformed layer in the subsurface area. In the unloaded material (Fig. 3.11a), there is no contrast change in the vicinity of the surface, and no deformed layer observed in the subsurface area. After ten cycles (Fig. 3.11b), a subsurface area with a slightly changed microstructure is observed. A tribologically deformed layer with a thickness of 0.52 ± 0.19 µm is found. This thickness is defined as the distance from the surface - along the sample's normal direction - to the point where the contrast no longer changes after enhancing contrast and brightness of each SEM image. This distance is determined by measuring its extension from the surface into the bulk of the material at five different positions on each image, and then calculating the average mean value as well as its standard deviation. This deformed layer increases in thickness with cycle number (Fig. 3.11b-f). The thickness of the deformed layer can be very different in grains with different orientation (Fig. 3.11c) and at grain boundaries (Fig. 3.11c), where it often is higher than inside a grain. The pronounced difference in depth of the tribologically deformed layer with respect to the crystallographic orientation, however, has not been seen in the depth of the dislocation trace line. For the highest cycle number of 5000 (Fig. 3.11f), the deformed layer has grown as thick as 15.73 ± 1.12 µm. Except very near the surface, this deformed layer appears homogeneous in the normal direction of the samples, in classical SEM secondary electron contrast. In Fig. 3.11g, the thickness of this layer is plotted against the cycle number in a double logarithmic fashion. The deformed layer's depth has exceeded the vertical viewing range of the SEM images when the sliding cycle number is higher than 1000 (Fig. 3.11e+f). Instead of the whole layer, only the upper part of this layer is thus shown in Fig. 3.11e+f. The depth is measured in cross-sections imaged with lower magnification. The same cross-sectional investigation was also performed at both dead centers of all wear tracks (see Fig. A4 in the Appendices). No systematic difference for the thickness of the deformed layer can be found between the middle of the wear track and the two dead centers. The appearance

of the deformed layer (thickness and the orientation dependence) is very similar to that in the middle of the wear tracks. Only the middle of the wear track is therefore presented in detail in this thesis.

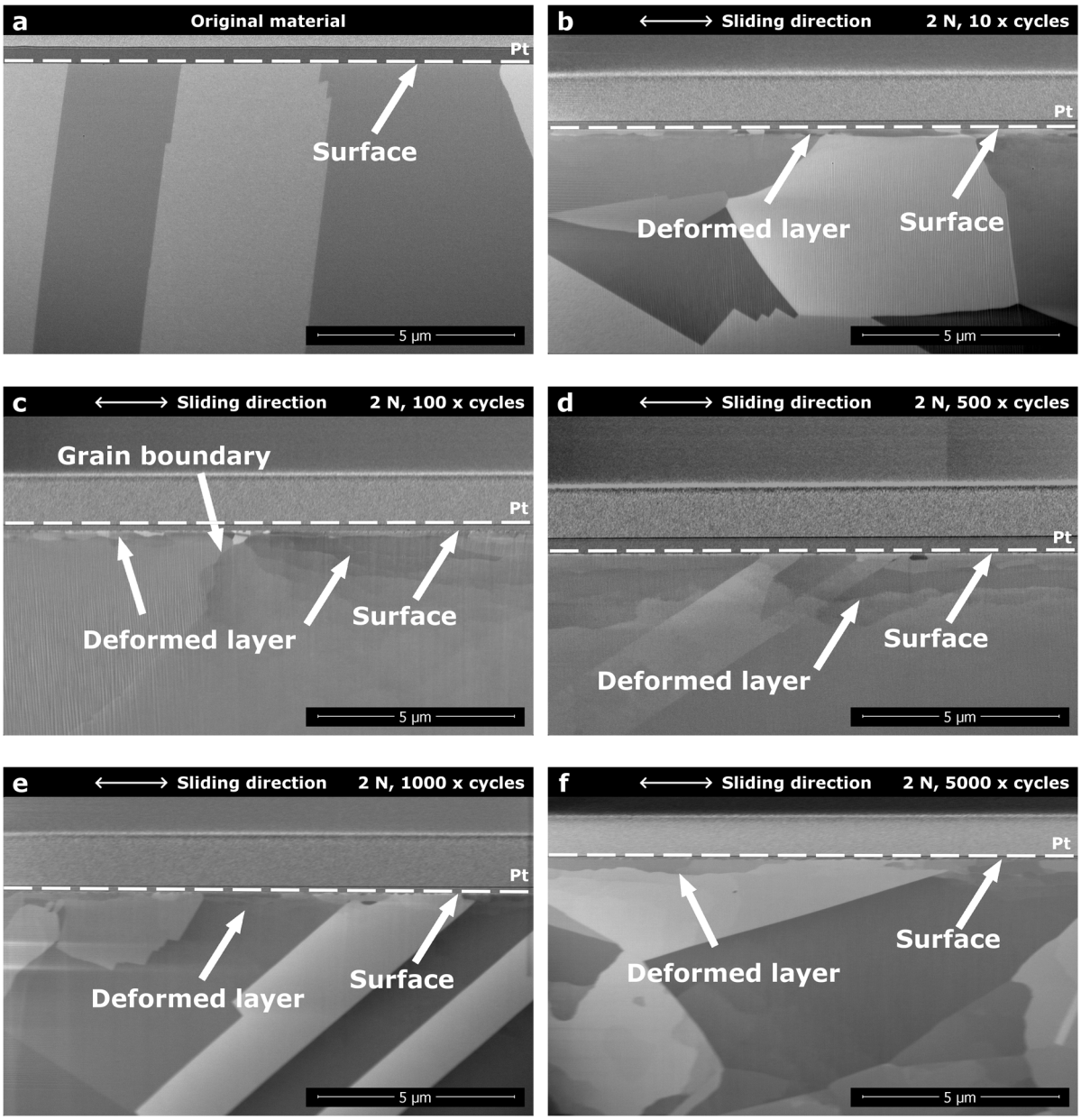

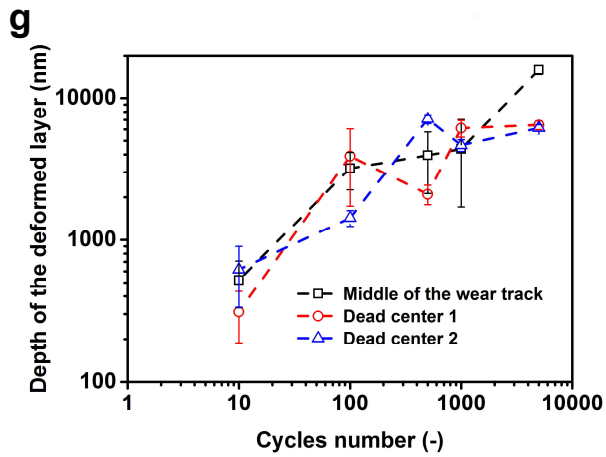

Figure 3.11: SEM images of OFHC copper under reciprocating tribological loading after different cycle numbers. (a) original material before tribological testing; (b) after 10 cycles; (c) after 100 cycles; (d) after 500 cycles; (e) after 1000 cycles; (f) after 5000 cycles; (g) thickness of the deformed layer, plotted against cycle number. The cross-sections were performed at the middle of the wear track, perpendicular to the sliding surface and parallel to the sliding direction. The contrast at the top of the images is from the two protective platinum layers, the copper surface is marked by white arrows and white dashed line. The data from the dead center of wear tracks are plotted in (g).

The observation of the tribologically deformed layer (Fig. 3.11b-f), the change of its thickness with increasing cycle number (Fig. 3.11g) and an apparent orientation dependence (Fig. 3.11c), required further investigation of the microstructure. Therefore, cross-sectional EBSD measurements were performed.

3.3.2 Cross-sectional electron backscatter diffraction with different sliding cycle numbers

Cross-sectional EBSD measurements were performed in the middle of the wear tracks. The aim of these measurements was to further characterize the crystallographic orientation and the GND density. The results for the crystallographic orientation mapping and the GND density analysis of the cross-sectional areas are shown in Figure 3.12. Orientation gradients

are observed in the cross-sections for higher cycle numbers (Fig. 3.12e+g). In some cases, especially in the area right underneath the surface, the quality of the diffraction pattern was not sufficient for reliable indexing. The amorphous protective platinum layers are also not indexed.

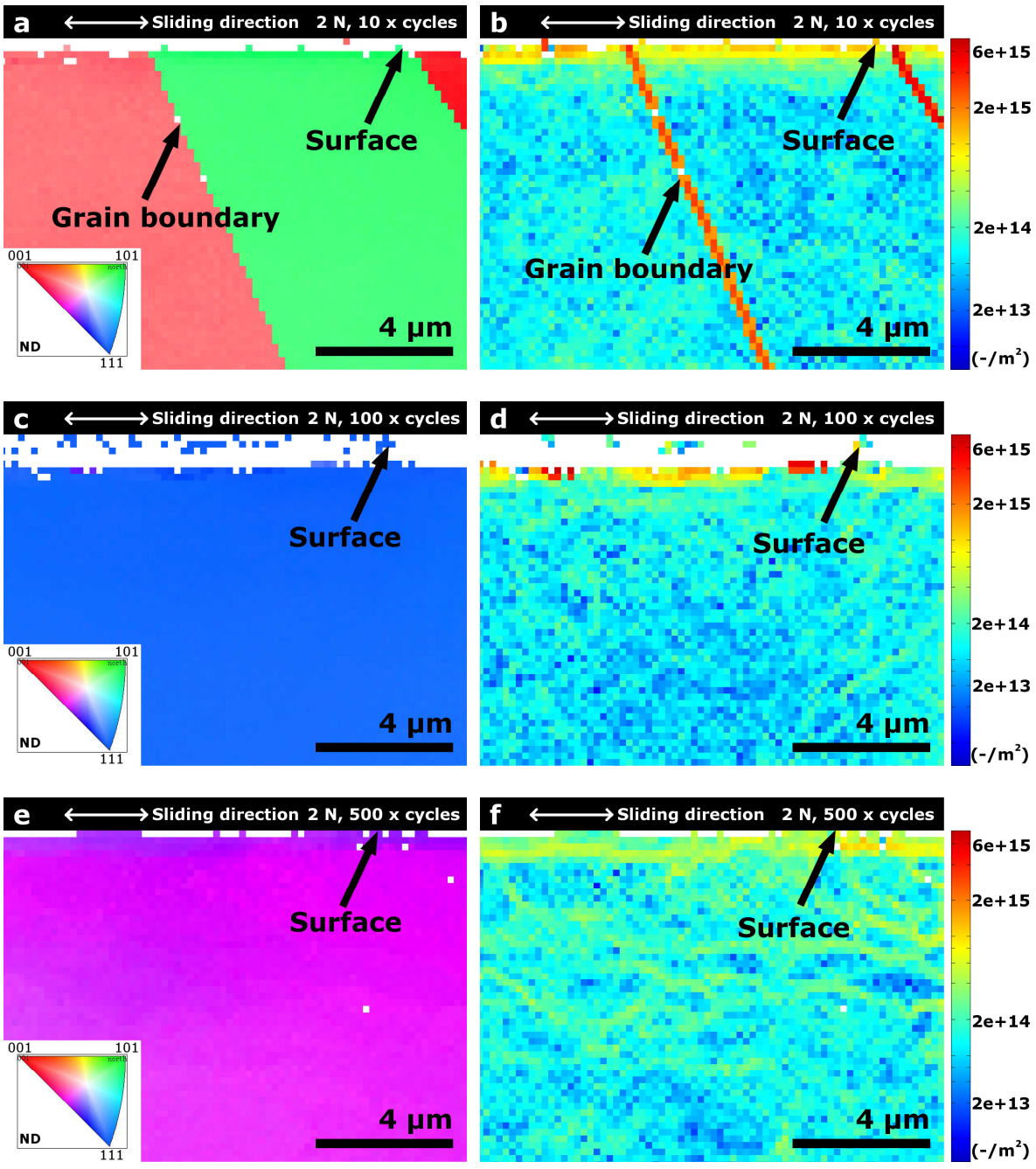

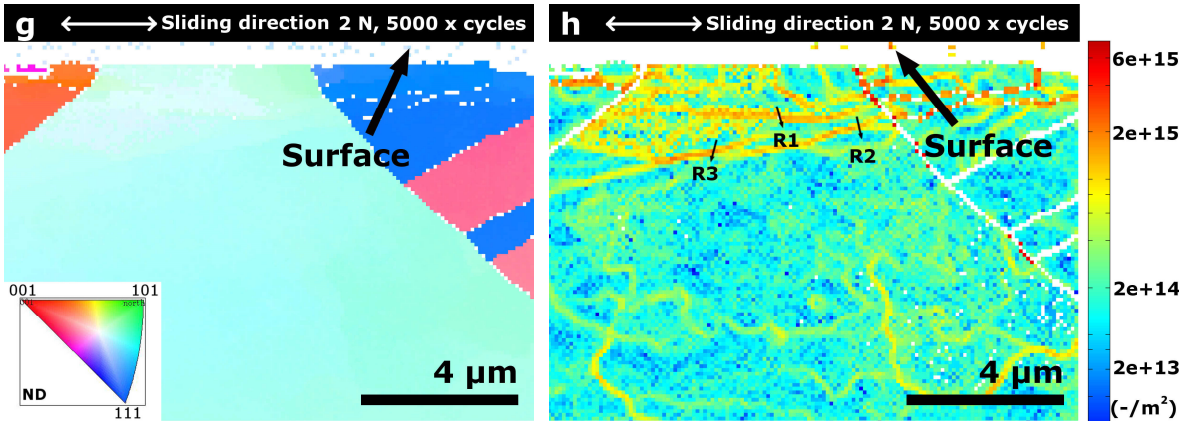

Figure 3.12: Crystallographic orientation mapping and GND analysis in the cross-sectional area of wear tracks of OFHC copper under tribological loading after different cycle numbers. (a) and (b) after 10 cycles; (c) and (d) after 100 cycles; (e) and (f) after 500 cycles; (g) and (h) after 5000 cycles. (a), (c), (e) and (g) are inverse pole figure orientation maps with respect to the samples' normal direction. (b), (d), (f) and (h) are GND density maps in the corresponding area. The color bar in the GND density mapping represents the number of GNDs per unit area (m^2). The cross-sections were milled perpendicular to the sliding surface and parallel to the sliding direction. The samples' surfaces are marked by black arrows.

From the sample after ten cycles to the one after 5000 cycles (Fig. 3.12b, d, f and h), the average GND density continuously increases with cycle number. In all samples, the area from the surface to a depth of 1 µm has a much higher GND density than deeper inside the material, indicating heavy plastic deformation near the surface. In the sample after ten cycles (Fig. 3.12a), a grain boundary is covered in the mapping. The average GND density in the left grain with a surface normal orientation close to [001] is higher than that in the right grain with an orientation close to [101] (Fig. 3.12b). In the mapping after 100 cycles (Fig. 3.12c+d), only one grain is covered. The initiation of a network of lines of high GND density appears at depths of more than 1 µm. After 500 cycles (Fig. 3.12e+f), a high GND density network is clearly visible and after 5000 cycles (Fig. 3.12g+h), the network has developed further. These high GND density networks for higher cycle numbers are invisible in the

crystallographic orientation map (Fig. 3.12e+g) and can only be observed with the GND analysis (Fig. 3.12f+h).

3.3.3 Scanning transmission electron microscopy results with different sliding cycle numbers

Dislocation networks at several micrometers depth (Fig. 3.12f+h) appear to evolve underneath a very highly deformed surface layer (non-indexed area right underneath the samples' surface) which cannot be resolved well in EBSD. STEM was thus applied to overcome the limited resolution of EBSD. Figure 3.13 presents STEM images for the samples after tribological loading for ten to 5000 cycles. After 100 cycles (Fig. 3.13b), a line-shape feature that shows bright contrast from one side and dark contrast from the other (highlighted by an arrow and labelled SAGB) is observed at a depth of 200 nm. At the same time, some hemispherical features (henceforth referred to as "clusters") with brighter contrast begin to appear at the surface (also highlighted by an arrow in Fig. 3.13b-e). With the cycle number increasing to 500 the clusters at the surface grow deeper into the material and cover more area at the surface (Fig. 3.13c). In Fig. 3.13c, one can also observe a subgrain forming in the subsurface area.

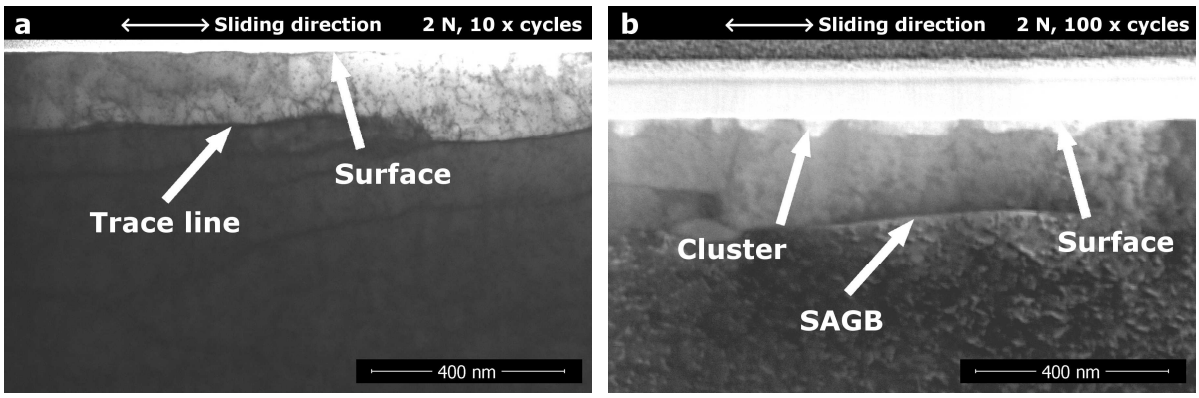

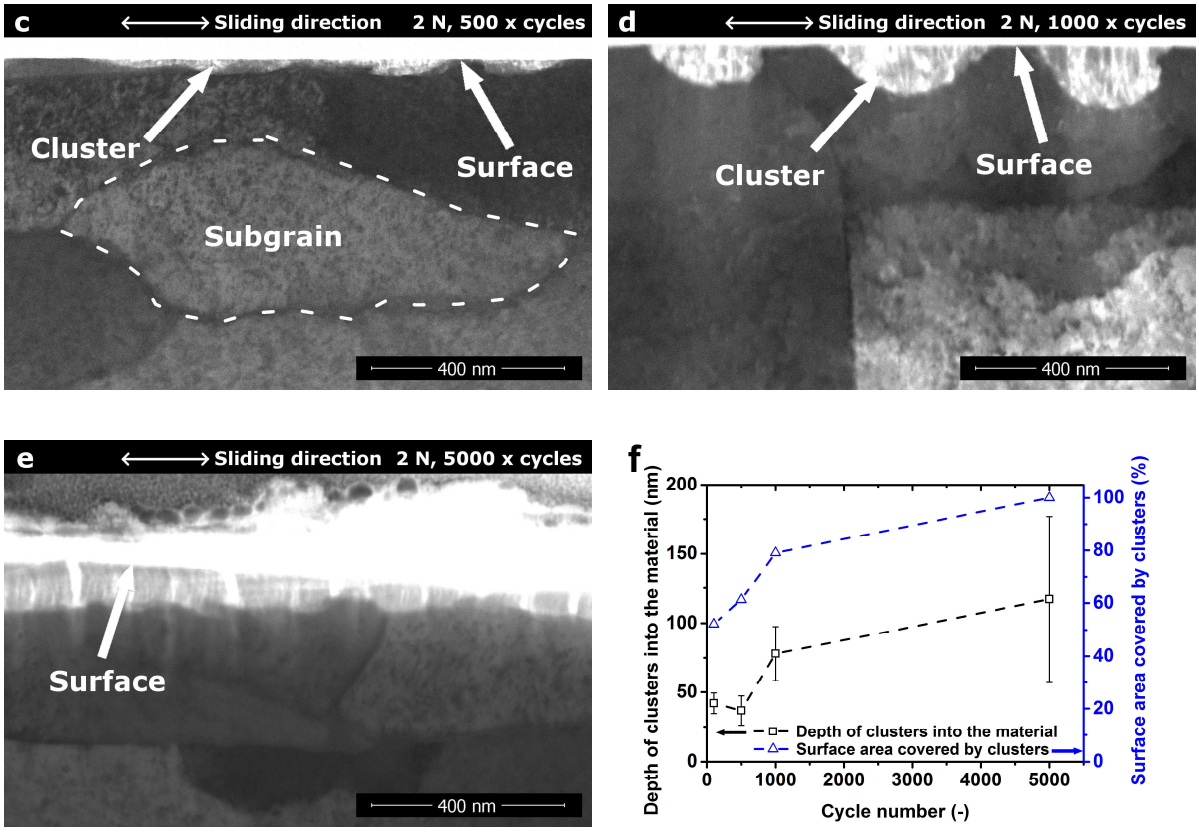

Figure 3.13: STEM images of OFHC copper under tribological loading after different cycle numbers. (a) after 10 cycles; (b) after 100 cycles, small angle grain boundary (SAGB) and clusters are marked by write arrows; (c) after 500 cycles; (d) after 1000 cycles; (e) after 5000 cycles; (f) the depth of the clusters and the surface area covered by clusters, plotted against the cycle number. The cross-sections were cut at the middle of the wear track, perpendicular to the sliding surface and parallel to the sliding direction. The contrast at the top of the images is from the two protective platinum layers and the sample surface is marked by write arrows.

With the cycle number increasing to 1000 and 5000, the clusters at the surface grow deeper into the material and cover more area at the surface (Fig. 3.13d+e). After 5000 loading cycles (Fig. 3.13e), the subsurface area is so heavily deformed that the interface between copper and the protective platinum layer can no longer be clearly distinguished. In the area very close to the surface, the microstructure appears to be very similar to that of the clusters observed for the tests with lower cycle numbers (Fig. 3.13d+e). The depth of these clusters as well as the surface area covered by them, are plotted against the cycle number in Fig. 3.13f. The depth is

measured at the lowest point of each hemispherical cluster (mean value of the measurements from all the clusters in the images). The covered surface area (in percent) is measured on the surface in each STEM image as the ratio of the length covered by clusters to the total length of the TEM lamella.

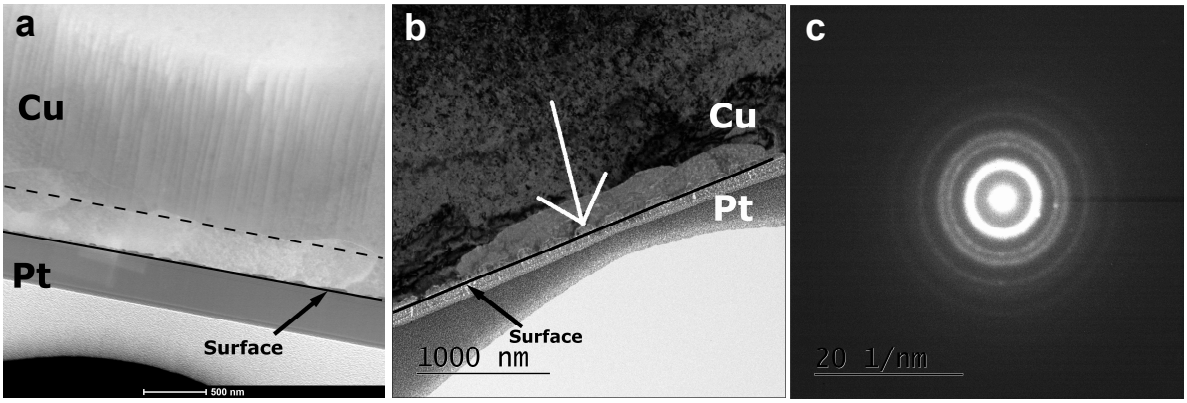

Figure 3.14: TEM images of OFHC copper under tribological loading [158]. (a) the lamella prepared in the wear track after 500 cycles loading; the surface is marked as the solid black line in the image and the position of the dislocation trace line is marked as the dashed black line; (b) the lamella prepared in the wear track after 100 cycles of loading; the surface is marked as the black line in the image and the diffraction area is marked by the white arrow; (c) the diffraction pattern taken in the center of panel (b). Both lamellae in panel (a) and (b) were prepared in the middle of the wear tracks, parallel to the sliding direction.

The lamella shown in Fig. 3.13c was also observed in the TEM (see Figure 3.14a). At a depth of roughly 350 nm, a contrast change can be seen which was not observed in the STEM image. TEM images were taken from the lamella shown in Fig. 3.13b and a selected area diffraction analysis was performed on one of the clusters, in order to further determine the nature of these clusters. A TEM image and the diffraction pattern are presented in Fig. 3.14b. The diffraction pattern shows a halo which appears to be slightly spotty.

3.3.4 Transmission electron microscopy characterization of surface clusters

The experiments for a detailed investigation on the surface clusters were conducted with a set of experiments under a normal load of 1.5 N. It should be stressed here that the microstructure from all my samples were examined right after the tribological tests to keep a minimum effect from environmental oxidation during sample storage.

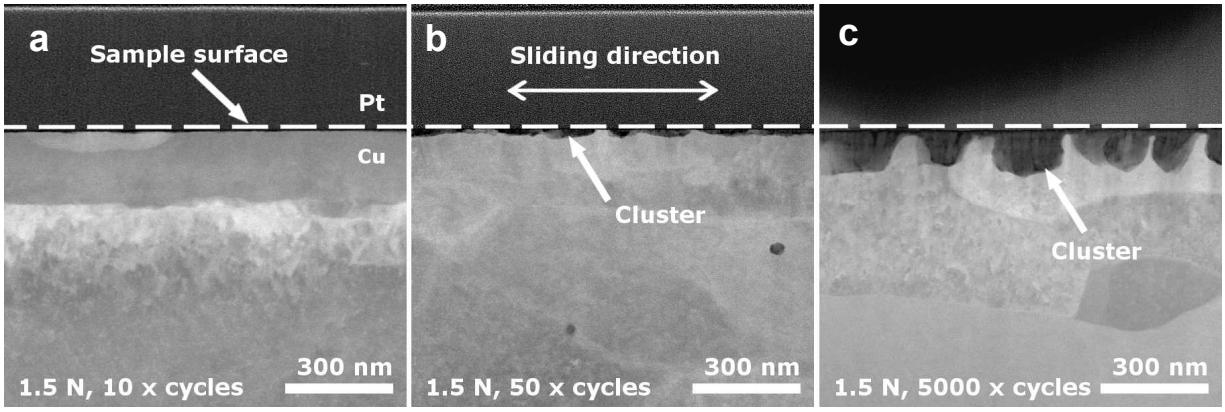

Figure 3.15: STEM results of the clusters at OFHC copper samples' surface under 1.5 N normal load after different numbers of cycles loading in HAADF mode [159]. (a) after 10 cycles; (b) after 50 cycles; (c) after 5000 cycles. The TEM lamellae were prepared in the middle of the wear track, along the sliding direction perpendicular to the sliding surface. The dashed white lines together with white arrows mark the sample surface. The sliding direction is marked by a white double arrow. The contrast above the sample surface is from the protective platinum layer.

Figure 3.15 presents the STEM images in HAADF mode for samples after different numbers of sliding cycles. Compared to BF and DF, HAADF mode yields the most contrast induced by the atom mass difference of the material, which is ideal for observing differences in chemical composition. The contrast at the very top of all the three images is from the protective platinum layer and the copper sample surface is marked by the white dashed line. After ten sliding cycles (Fig. 3.15a), there is no drastic HAADF contrast change in the copper sample. Some features can still be observed, for example, the dislocation trace line shows up at a depth around 200 nm. After 50 cycles of sliding (Fig. 3.15b), a somewhat wavy and

discontinuous layer appears at the sample surface with a depth of around 30 nm. The wavy edge at the bottom of this layer suggests that some probable hemispherical features are being developed (similar appearance as the "clusters" in Fig. 3.13b-e). Inside this layer, the contrast appears to be darker. After 5000 cycles (Fig. 3.15c), the clusters with a hemispherical shape can be clearly observed as the darker contrast appearing at the sample surface.

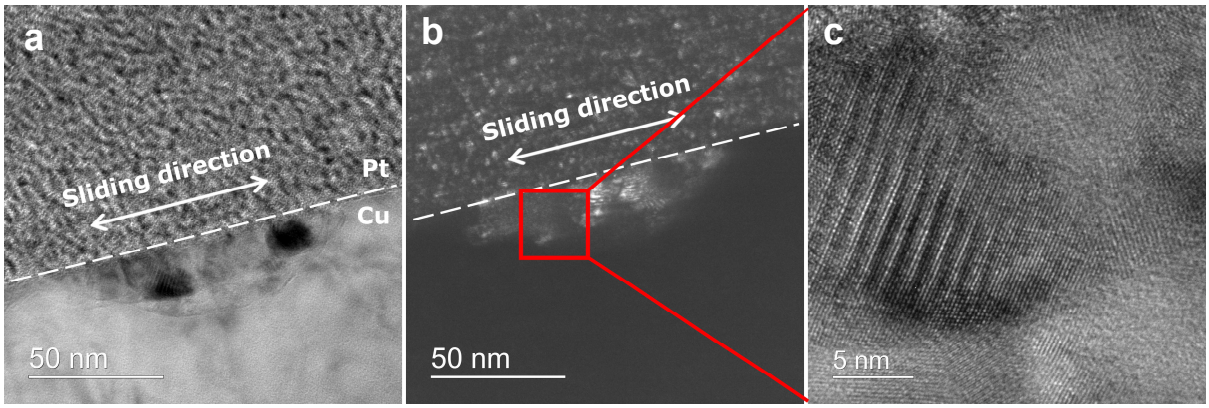

Figure 3.16: (HR)TEM images of a cluster after 50 cycles of tribological loading [159]. (a) BF image; (b) DF image using one of the diffraction beams; (c) HRTEM image from the area in the red rectangle in (b). The results are taken from the same lamella as shown in Fig. 3. 15b. The sample surface is marked by dashed white lines. The sliding direction is marked by white double arrows.

To reveal the microstructure of the clusters in greater detail, (HR)TEM is applied to the clusters after 50 cycles loading (see Figure 3.16). Figure 3.16a presents one of the clusters using BF contrast. Figure 3.16b is the DF image of the same area as in Fig. 3.16a, taken using one of the diffraction spot in SAED patterns. Areas with bright contrast can be observed in the cluster. In the HRTEM image (Fig. 3.16c) taken at the area inside the cluster marked by the red rectangle in Fig. 3.16b, the crystalline structure are clearly visible with a possibly amorphous matrix.

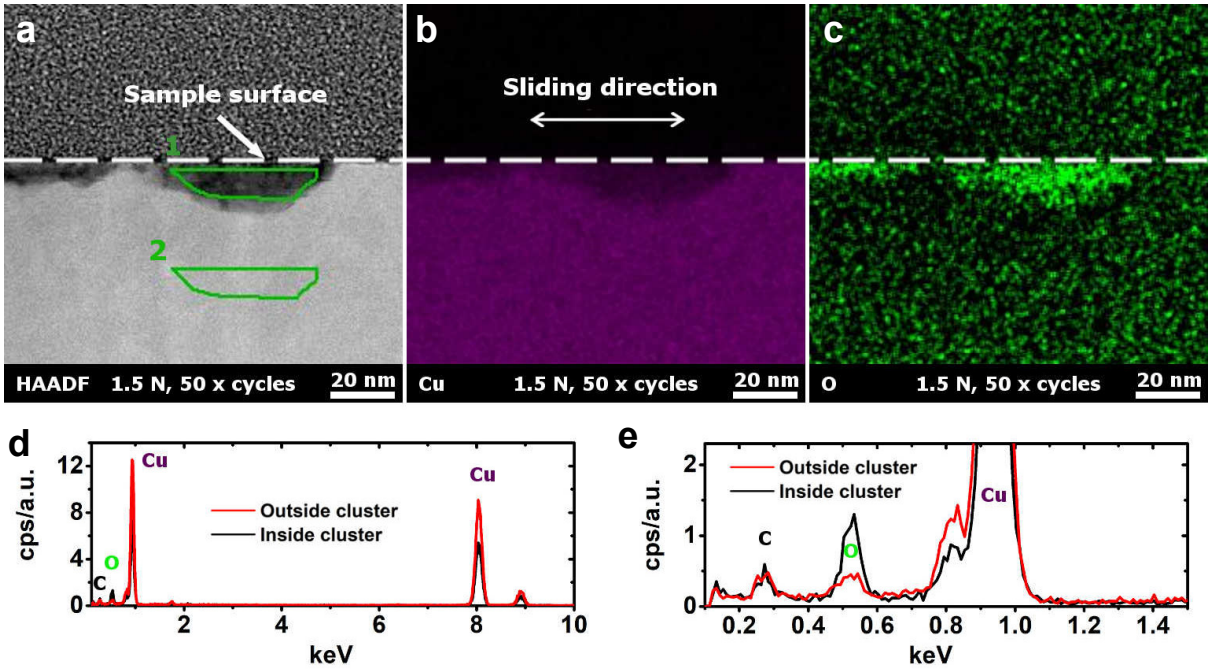

Figure 3.17: EDXS analysis on a sample after 50 cycles of loading [159]. (a) HAADF imaging of the scanned area. The two green polygons mark the area where the spectra of (d) and (e) were taken: window 1 is inside, window 2 is outside the cluster. The sample surface is marked by the white dashed line; (b) copper map of the scanned area in (a); (c) oxygen map of the scanned area in (a); (d) spectra for the two windows in (a) for a range in X-Ray photon energy of 0.1-10.0 keV; (e) spectra for the two windows in (a) for a range in X-Ray photon energy of 0.1-1.5 keV.

EDXS and STEM was applied to identify and map the chemical elements in the subsurface area after 50 cycles of sliding (see Figure 3.17). The mapping area as well as the two windows in which the spectra were taken is shown in the STEM image in Fig. 3.17a. The brightness contrasts in the EDXS maps (Fig. 3.17b+c) give a quasi-quantitative distribution of the elements in the map. The clusters appear to be oxygen-rich and copper-poor (Fig. 3.17b+c). The spectra in Fig. 3.17d+e demonstrate that there is no significant amount of other elements inside the clusters, but copper and oxygen. A quantitative analysis of the chemical composition in the two windows in Fig. 3.17a yielded that the oxygen concentration is 7 wt.% inside the cluster and 2 wt.% outside.

The subsurface microstructure is examined after ten cycles of tribological loading to reveal these clusters' origin. No cluster-shape contrast is observed at the surface in the HAADF image (Fig. 3.15a and Figure 3.18a). The EDXS oxygen mapping (Fig. 3.18b) of the same area as in Fig. 3.18a shows, however, some bright pixels grouping as a somewhat discontinuous, extremely thin layer with a thickness of less than 10 nm at the sample surface (fragments of the layer are highlighted by the red circles in Fig. 3.18b).

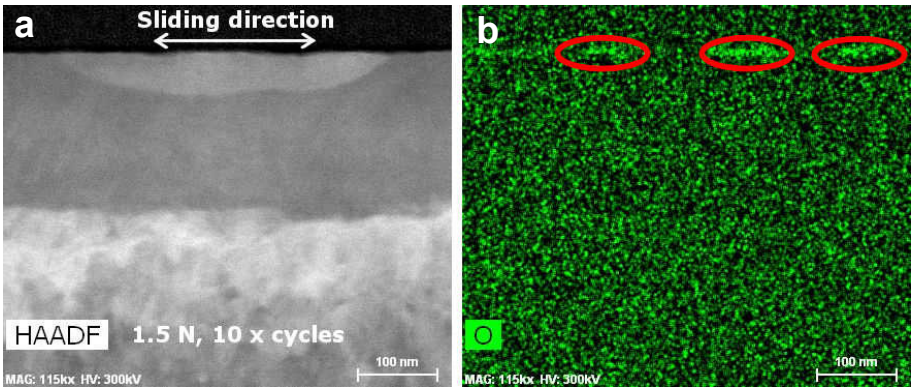

Figure 3.18: STEM-EDXS results on a sample after ten cycles of loading [159]. (a) HAADF image; (b) oxygen map of the scanned area in (a). The surface oxidation thin layer is highlighted by the red circles.

3.3.5 Scanning transmission electron microscopy observation of surface clusters in different atmosphere and different counter body materials

Two experiments were conducted specifically to reveal the source of the oxygen in the clusters. In each experiment, the oxygen from one of the possible sources was removed. First, Si_3N_4 instead of sapphire (Al_2O_3) spheres were used eliminate the oxygen in the counter body. Second, exactly the same experiments using sapphire spheres and copper were performed in dry nitrogen atmosphere, to eliminate the oxygen from the atmosphere.

The STEM image taken after 1000 cycles of sliding using copper against sapphire sphere in dry nitrogen atmosphere are shown in Figure 3.19a. Yet at the sample surface, no cluster

shape feature is observed. The interface between the protective Pt layer and the copper surface appears to be perfectly sharp with no other features in between.

The microstructure in copper after 1000 cycles of loading against a Si_3N_4 sphere is shown in Fig. 3.19b. Compared to the experiments with sapphire spheres (Fig. 3. 12d and Fig. 3.19a), the sliding contact of Si_3N_4 - Cu generates a large amount of wear on the surface. Loose wear particles were visible on the wear sample surface after the test. A layer with very fine microstructure is observed at the sample surface (marked as "Nanocrystalline layer" in Fig. 3.19b). A crack is observed in Fig. 3.19b. Grain refinement and increased dislocation density is visible in the delaminated copper as well as in the bulk underneath.

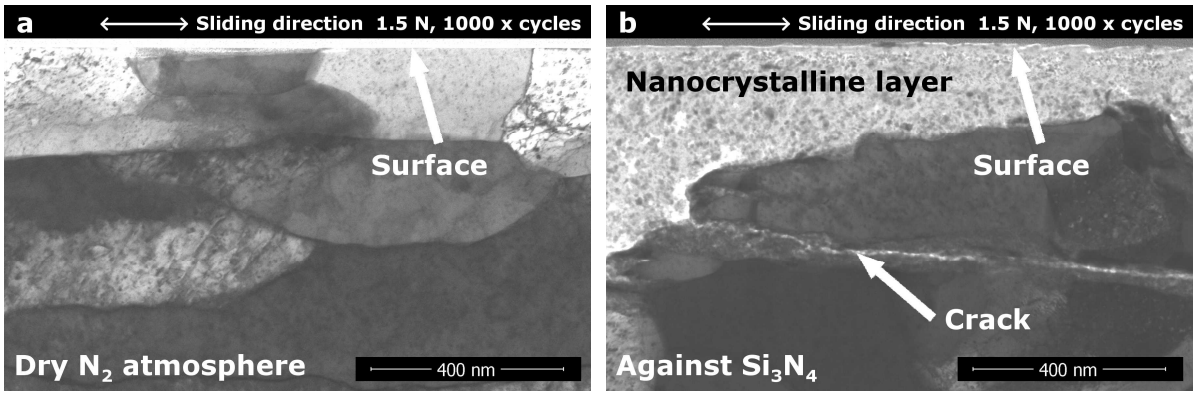

Figure 3.19: STEM results on the subsurface microstructure to investigate the source of oxygen in the surface clusters. (a) OFHC copper sample run against a sapphire sphere under 1.5 N normal load for 1000 reciprocating cycles, in dry N_2 atmosphere; (b) OFHC copper sample run against a Si_3N_4 sphere under 1.5 N normal load for 1000 cycles in air with 50% relative humidity. Samples' surface and crack are marked with white arrows.

Chapter 4: Discussion

4.1 Origin of microstructural discontinuity: dislocation trace line and its formation mechanisms

Even though the results for microstructural changes under tribological loading show great variation (as mentioned in Chapter 1), a common theme is that experiments regularly show a distinct discontinuity in the microstructure between a surface layer and the underlying bulk material [7, 33, 60, 70, 77, 78]. The origin of this discontinuity remains elusive but is crucial to the understanding of friction and wear, because the surface layer carries most further plastic deformation, accumulates damage and is exposed to the environment. The observation of the microstructure evolution in this work shows that even after only one sliding pass, under mild sliding condition, a definite and sharp microstructural feature – the dislocation trace line – develops. This feature is discussed in this section which reveals the very origin of the microstructural discontinuity generated by tribological loading.

4.1.1 Details of the microstructure of the trace line

The dislocation trace line is observed as a sharp line feature in STEM images through many different conditions in a cross-sectional view (x-z plane in Fig. 3.2-3.6, 3.9, 3.10 and 3.13a). TKD scans over this line reveal an average misorientation of 4.6 ° between the region above and below after one sliding pass under 2 N normal load. This indicates that the trace line effectively has the character of a small angle grain boundary (SAGB). HRTEM results further clarify the nature of the trace line. The brighter appearance of the near surface layer in Fig. 3.3a above the trace line indicates a different diffraction condition and a possibly reduced dislocation density. The trace line seen in the center of the HRTEM image in Fig. 3.3b is similar to a typical SAGB and the misorientations measured by TKD suggest the same.

It is shown, however, in the HRTEM image (Fig. 3.3b) that the trace line itself consists of many dislocation-like contrast features and has a width of 5-8 nm. Hence apparently, it is not an ideal SAGB, but rather a complex self-organized dislocation network.

The SAGB model in which a lattice rotation is introduced by an array of edge dislocations is presented in Figure 4.1. The spacing between neighboring dislocations in such an array is inversely proportional to the sine of a half of the rotation angle (if the angle is small, approximately equal to the angle itself). Applying this model to an array of ½ <110> dislocations, which are the common dislocations in a fcc crystal, using the measured rotation angle of 7.9 ° (Fig. 3.3b), the dislocation spacing is calculated to be 1.79 nm. Since the zone axis in the HRTEM image (Fig. 3.3b) is [103], only the edge component of ½ <110> dislocations (with a Burgers vector inclined about 26 ° to the imaging plane) projected to the (103) plane is visible. The length of the Burgers vector of a ½ <110> dislocation in this projection is thus 0.23 nm. Therefore, the visible dislocations are expected to have a spacing of 1.6 nm in the trace line.

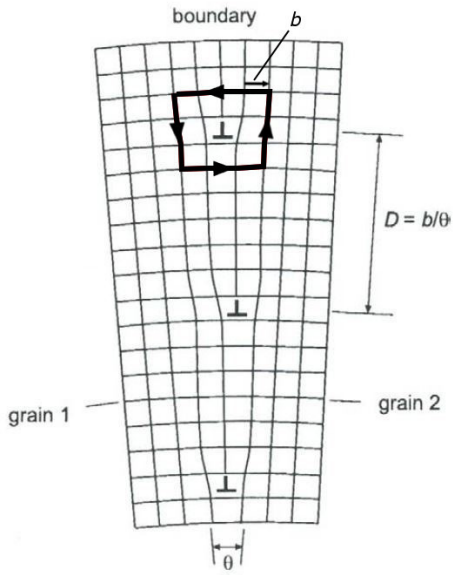

Figure 4.1: Model of an array of pure edge dislocations well aligned. The lattice rotation angle is inversely proportional to the average dislocation spacing in the array [160].

As the lattice is highly distorted in the dislocation trace line, it is very challenging to determine the actual spacing between dislocations by locating individual dislocations in Fig. 3.3b. Dislocations might also form dipoles inside the trace line and thus are not contributing to the total lattice rotation. The spacing between dislocations was measured with a method relying on an inverse fast Fourier transformation to only visualize the (200) planes (using the two spots in red circles in Fig. 3.3b). With this method, 15 extra (200) lattice planes were found, indicating 15 net dislocations inside the trace line. Given the length of the dislocation trace line in Fig. 3.3b, this yields an average dislocation spacing of 1.8 nm. This value agrees very well with the 1.6 nm spacing calculated using the pure edge dislocation array model (Fig. 4.1).

All these features of the trace line in both the cross-sectional view show similarities to the dislocation structure reported before in copper with very large strain for both sliding contact and cold rolling [88, 105]. The trend in which the size of the dislocation structures seen in this thesis' results also agrees with the equilibrium grain size reported in the literature [63]. Yet the trace line observed in this thesis is distinct from the reported results [65, 77, 105, 161] for a) the microstructure between the trace line and the surface appears to be dislocation free; b) the trace line is almost perfectly parallel to the sample surface and continuous with little change in depth; c) the trace line appears to be a quasi-2-D network parallel to the sliding surface.

The central role that dislocations play in the microstructural changes under tribological loading was previously reported by other authors [58, 75, 76, 106]. However, since most of these studies were performed at significantly higher contact stresses, they quickly resulted in the generation of wear particles [58, 75, 76], mechanical mixing with the counter body [76] and the beginning of recrystallization (which was not observed in my experiments even after high cycles of loading, see Figure A6) [75, 76]. The early stage of dislocation self-

organization which is identified in this thesis, has not been reported previously. The relatively small depth at which the trace line forms as the first microstructural change due to tribological loading, and its independence from the specific microstructural state of the material, e.g. grain orientation, suggests that the mechanism behind its formation must be a general property of the tribological experiment, a prime candidate being the stress field near the sample surface or of the surface geometry.

4.1.2 Formation mechanism: a model based on the stress field

Dislocation trace line appears with many generic features, such as being parallel to the sample surface and appearing at an almost constant depth. It is expected that the formation mechanisms for the trace line are generic as well. This is why the following hypothesis is sketched up based on the stress field in the copper sample induced by the sliding contact.

When the contact stress is estimated, the maximum Hertzian pressure appears at a depth of around 20 μm, which cannot be correlated to the depth where the trace line is observed (120-150 nm). Considering a relatively low yield strength of copper, the magnitude of contacting stress cannot explain the formation of the trace line. However, a sign change in the stress field instead of the magnitude of the stress is found to correlate well with the depth of the dislocation trace line.

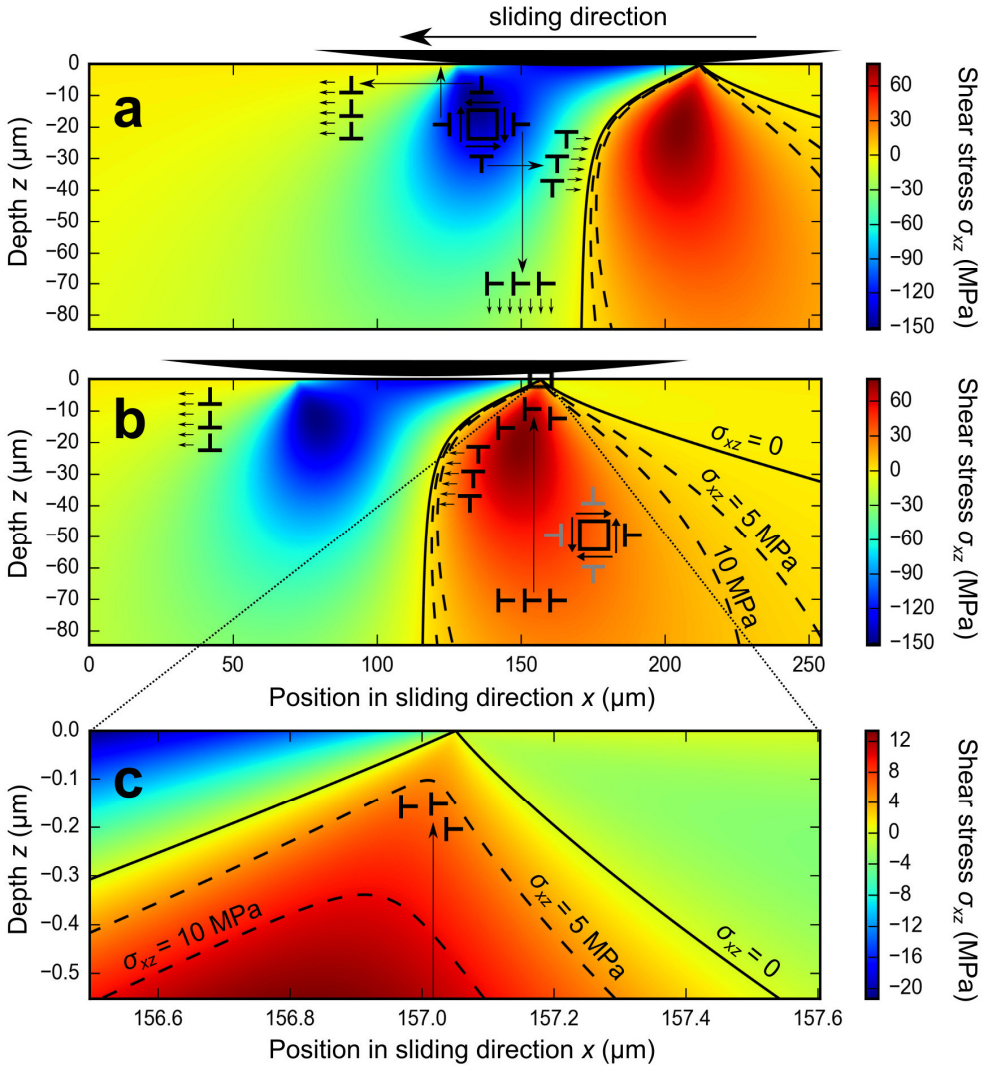

Figure 4.2: Stress field under the sliding contact [162]. The xz-component of the stress field in the middle of the wear track along the sliding direction for a friction coefficient μ = 0.25. Sliding is in positive x-direction. Solid and broken lines show contours of constant stress. Panels **a** and **b** display the same stress field but translated by the motion of the sphere. The arrows indicate the movement of the respective dislocations. Panel **c** shows a blowup of the near-surface region at the trailing edge of the contact.

It is hypothesized that the motion of dislocations within the strongly inhomogeneous stress field below a sliding spherical indenter determines the formation of the trace line. Dislocations are driven by the shear stress resolved onto their respective slip systems. The discussion is simplified here to four hypothetical (perpendicular) slip systems that illustrate general features of dislocations moving underneath the indenter (see Figure 4.2), assuming

that the indenter is moving over preexisting dislocations – no dislocation generation. Dislocations with a Burgers vector parallel to the surface either follow the motion of the slider or are left behind. Dislocations with a Burgers vector perpendicular to the surface are either pushed into the bulk or they disappear at the surface. This generates an area of reduced dislocation density near the surface, which explains the brighter contrast above the trace line in the TEM image in Fig. 3.3a. The Peach-Köhler force on these dislocations is roughly proportional to the in-plane (x-z) shear-component of the stress tensor, σ_{xz}. Dislocations are assumed to be arrested if this stress drops below a yield stress τ_Y. The ideal hypothetical limit for a single dislocation in an ideal crystal is the Peierls stress which for copper is lower than $\tau_Y \approx 1$ MPa. For pure polycrystalline copper the yield stress ranges from 1 MPa to several hundred MPa depending on the grain size and the dislocation density [139]. For the well annealed pure copper in this thesis a value of approximately ~ 5-10 MPa is used.

The main contribution to the force on dislocations moving in the cross-sectional area underneath the indenter is the stress field's shear component σ_{xz} [160]. Figure 4.2a shows σ_{xz} obtained from a superposition of Hertz's solution and a frictional surface traction [29]. To estimate the stress field (and therefore σ_{xz}) underneath the sliding contact, a constant local coefficient of friction μ is assumed. Experimental values are difficult to obtain from a single trace, but the data suggest that the friction coefficient is on the order of $\mu \approx 0.25$. The local traction $Q_x(x,y)$ in sliding direction x is then proportional to the normal load $P(x,y)$: $Q_x(x,y) = \mu P(x,y)$. $P(x,y)$ as obtained from Hertz theory. The total subsurface stress is calculated by adding the contributions from traction and normal load. The analytical formulation of the subsurface stress by Hamilton are used for both contributions [29].

As the sphere continues to move, the sign of σ_{xz} changes for a material point below the indenter (the solid line in Fig. 4.2b+c shows the location of the sign change), pulling dislocations that were previously pushed into the bulk back up towards the surface again (Fig.

4.2b). In the near surface region at the trailing edge of the indenter, σ_{xz} steeply goes to zero underneath the surface. The exact location of zero stress depends on friction coefficient and load. Dislocations stop moving towards the surface where the stress drops below the yield stress τ_Y of the material (Fig. 4.2c) and self-organize into the trace line.

As evidenced by the character of the trace line, it is effectively formed from dislocations with a Burgers vector perpendicular to the surface plane (see Fig. 4.2). These are arrested when $\sigma_{xz} \equiv \tau_Y$. Black solid lines in Fig. 4.2 show contours of $\sigma_{xz} \equiv 0$, and the contours for finite values (dashed lines in Fig. 4.2) of σ_{xz} follow similar trends. In the slow speed tribo-experiments the trace line is expected to form at the point of closest approach of this contour to the surface.

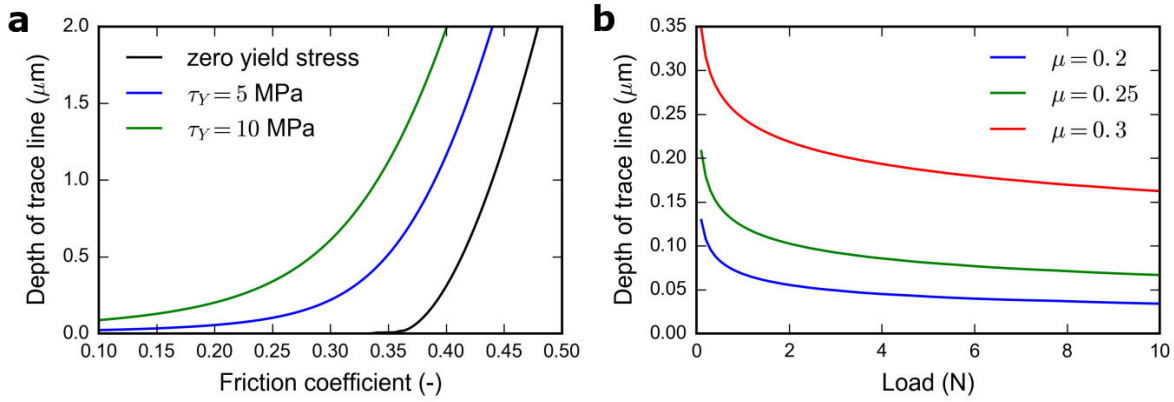

Figure 4.3: Depth of the trace line obtained as the closest distance to the surface of contours of constant stress [162]. Dislocations are arrested as the stress reaches the yield stress. The trace line forms around the closest point to the surface where the stress drops below the yields stress. (a) Depth of the trace line as a function of friction coefficient under a normal load of 2 N. The legend indicates the respective yield stress that was used to obtain these curves. (b) Depth of the trace line as a function of load for a yield stress of 5 MPa. Different lines show results for different friction coefficients as indicated in the legend.

Figure 4.3 shows the depth of the trace line obtained from this model for different values of the yield stress. Contours of zero stress touch the surface for friction coefficients below a

critical value of $\mu_c \approx 0.35$; for the Poisson number $\nu = 0.34$ used for copper (Fig. 4.3a). The depth of the trace line is only weakly dependent on friction coefficient (Fig. 4.3a) and load (Fig. 4.3b) below μ_c. Above μ_c, the depth of the trace line becomes sensitive to the friction coefficient and will be pushed deeper into the material as friction increases.

4.1.3 Predictions from the model and corresponding experiments

The model above leads to a couple of immediate predictions:

- The character of the arrested dislocations corresponds to the direction of the observed net experimental tilt in Fig. 3.3.
- The trace line is expected to be found across variation in loads, in other materials than copper and for different crystallographic orientations, since the dislocation trace line is solely explained with the stress field of the sliding contact.
- A second sliding pass in opposite direction should decrease the tilt angle at the trace line, because dislocations of opposite Burgers vector are pulled from the bulk to the surface, thereby partially compensating dislocations in the trace line.
- Multiple passes in the same direction are expected to result in more misorientation between the areas above and below the trace line. The trace line should have a weak dependency on the coefficient of friction.

These hypotheses were successfully tested experimentally (corresponding results can be found in Fig. 3.2-3.6, 3.9 and 3.10). According to the small angle grain boundary model (Fig. 4.1), the arrested dislocations in the trace line are supposed to generate a lattice rotation towards the sliding direction (see HRTEM results in Fig. 3.3 and TKD results in Fig. 3.5). At low normal load of 0.5 N (Fig. 3.2b), the dislocation trace line is observed at a depth of 120 ± 8 nm beneath the surface. For higher normal loads (1 N and 2 N), the depth of the trace line remains approximately constant. The depth of the trace line (the one closer to the sample surface if there are two trace lines) in Fig. 3.2 are plotted against the normal load. The

experimental results demonstrate a decreasing depth with increasing normal load in Fig. 4.3. For realistic values of the yield stress between 5 to 10 MPa, as used here, the model predicts the position of the trace line somewhere between 50 nm and 200 nm (Figure 4.4) with a coefficient of friction of 0.25. This is in excellent agreement with the experimentally observed value of ~100 nm.

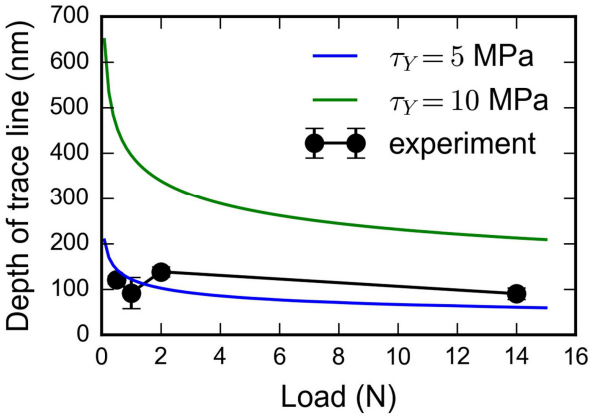

Figure 4.4: Depth of the dislocation trace line plotted against the normal load [162]. The points are the experimental results from Fig. 3.2b-e; The blue and green curves are the expected depth calculated using the model described in section 4.1.2 with different yield stresses of copper.

Further tests on different metals (nickel and a brass alloy containing 5 wt.% zinc) all show the appearance of the trace line after the very first pass (Fig. 3.10). All the grains, in which the trace line appears, are randomly lifted out and therefore are supposed to be crystallographically oriented randomly. The trace line appears at a constant depth in almost all these randomly oriented grains, demonstrating its independence of the crystallographic orientation. Fig. 3.9a demonstrates that the dislocation trace line (after two passes in the same direction) passes almost unperturbed through a grain boundary and appears to be independent of crystal orientation.

With one sliding cycle, the misorientation over the trace line is reduced (from 4.6° to 0.6°), yet the trace line is still visible because the already developed dislocation structure cannot be

fully annihilated with just one sliding pass against the previous sliding direction. With increasing number of passes (Fig. 3.4), the trace line increases in misorientation (e.g. from 4.6° after one pass to 15.6° after four passes) until after ten passes two trace lines are visible, one of which is somewhat closer to the sliding interface (75 ± 6 nm deep, Fig. 3.4d).

4.1.4 A glimpse of the trace line's microstructure in 3-D

Together with the plan view (S)TEM results, the subsurface microstructure in the vicinity of the dislocation trace line can be revealed in 3-D. The contrast of the sharp line features (Fig. 3.7, marked by the arrows) parallel to the sliding direction in the plan view appears to be very similar to the dislocation trace line in the cross-sectional STEM images (Fig. 3.2 and 3.4). These lines are thus speculated to be structures formed through dislocation self-organization as well and therefore should carry a rotation and / or tilt character leading to different crystallographic orientations on each side of a line. This is supported by the observation of the darker and brighter contrast in the dark field image in Fig. 3.8b, and also by the different diffraction patterns in Fig. 3.8c-f. The same diffraction pattern observed with only a minor rotation (1.5 °) (Fig. 3.8d+e) indicates that the line feature carries a rotation character along the normal of the TEM lamella (along the z-axis of the copper sample); the change in spots' intensity (Fig. 3.8c-f) indicates that the orientation of the crystal has been tilted slightly (along the x-axis and / or y-axis of the copper sample) [156]. The latter can be correlated with the observation of the lattice rotation observed in the cross-sectional view (Fig. 3.3b).

In addition, the depth where the line features in the plan view end (marked by the white crosses) corresponds, with a difference smaller than 8 %, with the depth of the dislocation trace line as observed in the cross-sectional STEM images (Fig. 3.2 and 3.4). Even though these depths match almost perfectly, one has to keep in mind that the standard deviation of the measurement is higher than 10 % in Fig. 3.7. Hypothetically connecting the white crosses in Fig. 3.7, results in a wavy feature at a depth of around 150 nm. This wavy feature is

probably the dislocation trace line observed in another projection (plan instead of cross-sectional view). In other words, the dislocation trace line may occur with a waviness observed in the plan view and this waviness still renders the depth of the trace line 100-150 nm in the cross-sectional view.

Interestingly, combining the cross-sectional view and the plan view results, different sharp line features observed in one view are not observed in another. More specifically, the dislocation trace line observed in the cross-sectional view images does not appear as a sharp line feature, or a band-shape feature (considering the thickness of the TEM lamella which is estimated to be around 50 nm) in the plan view images; The lines (Fig. 3.7, marked by the white arrows) parallel to the sliding direction in the plan view have not been observed in the cross-sectional view (Fig. 3.2 and 3.4). A possible reason is that during the TEM lamella preparation, the dislocations may rearrange and those with line direction parallel to the surface of the TEM lamella can and probably slip towards the lamella's surface and eventually disappear at the lamella's surfaces, due to the effect of thin film relaxation [163]. Since the trace line has a higher dislocation density (Fig. 3.5), the relaxation effect of the TEM lamella is expected to be especially strong in its vicinity. The dislocations forming the trace line in the cross-sectional view (Fig. 3.2 and Fig. 3.4) may no longer appear as a sharp line / band but as a wavy feature (Fig. 3.7). The same relaxation may happen to the lamellae prepared in a cross-sectional view, leading to the disappearance of plan view line features (Fig. 3.7, marked by arrows) in cross-sections. This effect, however, has only been taken into account for the investigation of individual (partial) dislocations in form of a small loop [164, 165]. The well-developed microstructural features in a TEM lamella (the trace line as well as the line features in the plan view) reported in this thesis, should not be majorly influenced by the image force. This is also supported by the dislocation trace line observed in both thinner (around 50 nm for TEM) and thicker (around 100 nm for TKD) lamellae with the same lattice

rotation character. On the contrary, an actually complex 3-D dislocation structure may lose a significant part of its complexity due to the thin film relaxation, which straighten the dislocations perpendicular to the film. For example, the tilting observed between SAD patterns from area A and B in Fig. 3.8a (patterns shown in Fig. 3.8c and 3.8d, respectively) indicate that the sharp feature between area A and B has the character of a twist boundary, most likely generated by dislocation that originally had a predominant screw character. Removal of materials for a cross-section when preparing a TEM lamella will expose such screw dislocations to a nearby surface where image forces should extract them from the lamella and leave a thereby dislocation free area above the trace line in the sample as observed in TEM (Fig. 3.3).

Another possible reason why the line features in the plan view images (marked by arrows in Fig. 3.7) are not visible in the cross-sectional view is that these line features may not be "captured" in the TEM lamellae for cross-sectional STEM imaging. The spacing between the neighboring line features in Fig. 3.7 and Fig. 3.8 is between 100 and 200 nm. The TEM lamellae prepared for the cross-sectional view (Fig. 3.2 and 3.4) are so thin (with a thickness of around 50 nm) that all of them are prepared between two neighboring lines in the plan view. The low dislocation density between the plan view line features (Fig. 3.7 marked by arrow) agrees very well with the low dislocation density observed in the area above the trace line (Fig. 3.3a).

The formation of these lines (marked by arrows in Fig. 3.7) parallel to the sliding surface needs to be further investigated and the mechanisms remain to be elucidated in the future. Based on the observation of the plan view microstructure, the following speculations are made:

The first possible cause for the formation of the line features (marked by arrows in Fig. 3.7) is the geometrical change of the sample surface: The surface of the wear tracks undergoes the

deformation from a flat surface into a curved one due to the sliding of the sapphire sphere. This inhomogeneous deformation requires a number of GNDs to accommodate, and it is reasonable to assume that the GNDs may be arranged in line features parallel to the sliding direction for this geometrical transition. However, the radius of the sapphire sphere used in the tests is 5 mm and the spacing of the line features is 100-200 nm. On such a scale, the contact may be considered as the contact between two flat surfaces. Even if the wear track's curvature is strictly taken account, the number of Burgers vectors of GNDs required for the curved profile is less than one. This is way too small for such complex, well-defined line features (marked by arrows in Fig. 3.7) and thus must not be the only reason for their formation. Another possibility is that the line features are generated by the surface roughness of both the sapphire sphere and the copper sample. Both contacting bodies' surface roughness has been measured earlier. The sapphire sphere's area roughness is smaller than 5 nm [166], and the copper surface's smaller than 20 nm [166]. The sole influence of such small indentation / scratch depths, as expected from such nanoscale roughness, is insufficient to generate complex dislocation microstructures, as reported in the literature [104] and therefore not considered to be the reason for the line features' formation. It is therefore very reasonable to assume these line features are generated by the complex stress / strain condition in the subsurface area under tribological loading, similarly to the formation of the dislocation trace line. A detailed examination of the stress field in all three dimensions is therefore critical to understand the microstructure. The estimation of the stress field considering only the elastic character of the contact may also not be sufficient for a fully-detailed understanding.

At the end of this paragraph, it must be pointed out that the unambiguous interpretation of the plan view (S)TEM results is a significant challenge, because, on the one hand, the thinning process for these TEM lamella is not protected by deposited Pt layer due to geometrical constraints during the preparation process, and therefore the lamella is expected to carry more

artifacts due to a relatively higher ion beam damage; On the other hand, the unusual tilting angle of both preparation and observation brings about additional difficulties in interpreting and understanding the features observed. What remains conclusive however is that a discontinuity in the subsurface microstructure is observed in the plan view images at a depth very much in the same order as the dislocation trace line in cross-sectional view, as the very origin of the tribologically induced discontinuity.

4.2 Evolution of dislocation structures under tribological loading

The dislocation trace line is the very origin of the microstructural discontinuity in the subsurface area under tribological loading. This discontinuity originated from the trace line remains in the later stages of the sliding contact. In this section, the evolution of dislocation structures under tribological loading after the formation of the trace line will be discussed in detail.

4.2.1 From dislocation trace line to small angle grain boundary

The pronounced contrast change above and below the dislocation trace line and the misorientation measured from HRTEM and TKD indicate a distinct orientation change in the subsurface area. The line-shaped feature in Fig. 3.13b (after 100 cycles, marked as “SAGB” by the white arrow) at a depth of approximately 200 nm shows a local orientation gradient which is compatible with a SAGB. The GND density analysis for the cross-sectional EBSD scans also gives strong evidence for a high concentration of dislocations at a larger depth of at least 0.5 μm (Fig. 3.12d+f). The depth of the line in Fig. 3.13b (after 100 cycles) is only somewhat deeper at about 200 nm, indicating that the dislocation trace line, which may already be interpreted as a small angle boundary of very small misorientation, may evolve into an SAGB with a larger misorientation with increasing cycle number. From this it is

hypothesized that dislocations keep accumulating in the dislocation trace line at a depth of around 150-200 nm for up to 100 cycles, before the formation of subgrains starts for higher cycle numbers. Subgrains may then move deeper into the material or be generated at greater depths.

When the cycle number reached 500, dislocation cells were formed and led to other new subgrains at greater depth (Fig. 3.13c). This being said, in the TEM image in Fig. 3.14a for a lamella after 500 cycles, the contrast change which could correspond to a SAGB from the original dislocation trace line can still be seen at a depth of about 350 nm.

4.2.2 Geometrically necessary dislocations networks

The direct information in the EBSD results is the crystallographic orientation of each pixel, which can be used to calculate a crystallographic orientation gradient. The misorientation between neighboring pixels can be interpreted as the GND density. The GND density analysis directly indicates that the primary mechanism behind the microstructure evolution in my experiments is dislocation activity. The GND density inside a grain becomes higher with increasing cycle number as non-uniform plastic deformation is increasing with progressing tribological loading.

A weak orientation dependence of the GND density can be seen in the two grains in Fig. 3.12a+b; With the left (100) grain having a higher GND density than the right grain which is close to a (110) orientation. This is expected considering both elastic and plastic anisotropy for compression normal to these surfaces reported in the literature [142, 167]. The GND density after 100 cycles (Fig. 3.12d) does not appear much higher than that after ten cycles (Fig. 3.12b) which may be because the grain picked by chance for 100 cycles is close to a (111) orientation (Fig. 3.12c). This orientation facilitates glide parallel to the surface and has unfavorably oriented slip systems for dislocation motion into the depth of the material, leading to an unexpected low GND density (Fig. 3.12d).

Besides the observation of the high GND density network, a net grain rotation can also be found in the cross-sectional area after high cycle number loading. Three rotations across the lines in the GND network (R1, R2 and R3 in Fig. 3.12h) are analyzed in terms of misorientation between pairs of points at both sides of them (shown as the two ends of short black arrows in Fig. 3.12h) in a cross-sectional area after 5000 loading cycles. The rotation angles around an out-of-plane axis are 2.5 °, 2.7 ° and 2.2 ° respectively, indicating mostly a rotation around the transverse direction (y-axis in Fig. 2.1b). This is another direct observation of the formation of small angle boundaries near the surface, and a further indication of (sub) grain rotation induced by dislocation activity.

4.2.3 Tribologically deformed layer

In the results, no systematic difference between the middle of the wear track and the two dead centers was found. This is contrary to some literature, e.g. in the case of combustion engines, where wear at the two dead centers of the cylinder has been reported to be higher than that for other in-cylinder parts [168]. In combustion engines, of course the sliding speed difference between the dead centers and the middle of the track is much larger than in the experiments in this thesis. As one of the main purposes of this work was to study the early stages of microstructural changes and to investigate the elementary mechanisms for these changes, the loading conditions - normal load and sliding speed - were chosen to be very mild. Therefore, a possible explanation for the difference between the results in this thesis and the published results with respect to the dead centers is most likely found in the difference in normal loads (Hertzian pressure) and the low sliding speed (strain rate).

The observation and the significance of a tribologically deformed layer has been widely reported in the literature [33, 53, 58, 79]. What is observed and now interpret is the contrast change in the images in Fig. 3.11, which can be correlated to the plastic deformation taking place in the subsurface area. The thickness of the deformed layer increases with cycle number

(Fig. 3.11g), indicating that the plastic deformation is getting more and more severe. The thickness of the deformed layer is different in grains with different crystallographic orientations due to the elastic and plastic anisotropy of copper [169, 170]. The thickness of the deformed layer is larger at grain boundaries (Fig. 3.11c), indicating that the plastic deformation is locally higher around grain boundaries compared to inside a grain. One explanation for this behavior is that the grain boundaries can be considered as dislocation obstacles where dislocations are accumulated. Consequently, it is expected to find more dislocations in the vicinity of grain boundaries.

When plotting the depth of the deformed layer versus the number of sliding cycles (Fig. 3.11g), the slope of the resulting curves reflects the sensitivity of the material's microstructure to the sliding distance (or time). Thus, the slope might be used as a parameter to characterize the dynamics of the microstructure evolution under reciprocating tribological loading. For my experiments, the slopes of the curves in Fig. 3.11g are about 0.5 (in this double-logarithmic plot). This corresponds to a square root growth law which agrees well with observations in the literature for the formation of an amorphous layer between two sliding diamond surfaces [73]. This might be an indication that this growth law is of a more general nature.

4.3 Tribologically induced oxidation at the sample surface

In this section, this thesis embarks on investigating the chemical changes combined with the microstructure of the top layer (or the clusters) under mild sliding conditions. The aim is to shed light on the mechanisms for tribologically induced surface oxidation.

4.3.1 Nature of the clusters at the surface: nanocrystalline Cu_2O in an amorphous matrix

In the HAADF images, after ten cycles of loading (Fig. 3.15a), no chemistry change can be observed in the subsurface area. The features such as the dislocation trace line observed here (Fig. 3.15a) are not due to and do not cause immediately a difference in chemistry (Figure A8) in such an early stage of loading. The formation mechanisms of the dislocation trace line are explained in the section 4.1. The wavy and discontinuous layer at the sample surface observed after 50 cycles of loading (Fig. 3.15b) with a much darker contrast strongly suggests a different chemical composition in this layer compared to the bulk underneath. The darker HAADF contrast indicates that the average atom mass of the material is smaller compared to pure copper. The wavy shape stems from the hemispherical clusters.

The bright areas in Fig. 3.16b suggests that the material in these areas have the same diffraction conditions, in other words, the same crystallographic orientation. This demonstrates the existence of a crystalline structure inside the clusters. The HRTEM image (Fig. 3.16c) shows evidence of a nanocrystalline structure. These nanocrystals possibly are in an amorphous matrix. The volume of the clusters, however, is too small for SAD patterns or power spectra to provide solid evidence and its amorphous nature remains speculative.

The clusters are observed through the intermediate and the late stages of the sliding contact and their growth can be seen in Fig. 3.13c-e. The clusters' shape remains hemispherical, however, their depth, as well as the surface area covered by them, changes with increasing sliding cycle number (see Fig. 3.13f). The comparison of the EDXS results between 50 and 5000 cycles of sliding under 1.5 N normal load suggests that the clusters change only quantitatively in shape and size with an increasing sliding cycle number (Fig. 3.15b+c shows the microstructure, and Fig. A7 shows EDXS spectra). This is why only the earlier stage (50

cycles and earlier) of the sliding contact is further analyzed to investigate the nature and formation mechanisms of these clusters.

A difference in chemistry between the clusters and the pure copper has already been suggested by the darker contrast inside the clusters in the HAADF images (Fig. 3.15b+c). EDXS chemistry mapping further reveals that the clusters appear to be oxygen-rich and copper-poor (Fig. 3.17b+c). The EDXS spectra for different ranges in X-Ray energy in Fig. 3.17d+e show that there is no significant amount of any other element inside the clusters, indicating the formation of copper oxides. This, and especially the lack of aluminum, reveals that there is no mechanical mixing between copper and sapphire (Al_2O_3). The quantitative chemical composition in (7 wt.% of oxygen) and outside (2 wt.% of oxygen) the cluster in Fig. 3.17a suggests that the amount of oxygen involved in the formation of the cluster is insufficient to generate purely cupric (CuO) or cuprous (Cu_2O) oxides (which would have 20 wt.% and 11.2 wt.% of oxygen instead, respectively). Looking into the thermodynamic of a Cu-O system, with an increasing oxygen concentration from zero, the first stable state is expected when the solubility of oxygen in copper is reached. This solubility has been reported as 0.075 wt.% oxygen in liquid copper at 850 °C [171], and this value can only be imagined dramatically smaller for oxygen in solid copper at room temperature. The second stable state with further increasing oxygen content will typically be the formation of Cu_2O [172] (11.2 wt.% of oxygen). The oxygen concentration inside the clusters is in-between these two states and therefore expected to be in an instable state. Under high local stress level of tribological loading and possible locally-high temperature, any instable solid state is expected to transform into stable ones. The persistent existence of the clusters (sharp interfaces with pure copper and the hemispherical shape) suggests that the material in the clusters is in a local free energy minimum and its nature can be interpreted as a non-trivial solid copper oxide phase different to the known ones. It is at least reasonable to assume that

this is a stable mixture of Cu_2O and Cu at an nanocrystalline scale. These hemispherical clusters of combined nanocrystalline and amorphous nature is probably not only generated by chemical but also by additional mechanical driving forces. In the following section, the source of oxygen in the clusters will be discussed, which allows for getting one step closer to revealing their formation mechanisms.

4.3.2 Source of oxygen in the oxides

The source of the oxygen in the clusters is key knowledge to understand the formation mechanisms of the clusters. Chemical reactions and mechanical mixing are two main approaches for oxygen to enter the sample surface during tribological loading [49]. Even though the sapphire spheres are not expected to have any chemical reaction with the OFHC copper samples [143], one cannot totally rule out the possibility that oxygen in sapphire (Al_2O_3) may get into copper. The spectra from the area both inside and outside the cluster in the cross-sectional area of the sample (Fig. 3.17d+e) show that aluminum is not present in the copper sample, indicating that there is no mechanical mixing between sapphire and copper. The oxygen in the clusters should thus not be from the sapphire sphere and therefore should be from the ambient air.

The results from the two additional experiments (dry N_2 atmosphere and Si_3N_4 sphere) further demonstrate evidence that the oxygen in the clusters is from the air. The absence of the clusters in the dry N_2 experiment (Fig. 3.19a) indicates that air (most probably O_2, possibly together with H_2O) is necessary for the formation of the clusters. The dislocation structure and the grain refinement (Fig. 3.19a) is generally similar to those in the experiments run in air (Fig. 3.13d+e). This is an indication that the formation of the oxide clusters at the sample surface is a separate process, distinct from the ones caused the dislocation mediated plastic deformation in the subsurface area.

The resulting microstructure in copper run against Si_3N_4 spheres is non-trivial to interpret (Fig. 3.19b). Changing the counter body material triggered a different wear mechanism for high sliding cycle numbers compared to the experiments using sapphire spheres (Fig. 3.13d+e). Copper being transferred to a Si_3N_4 roll during cold rolling has been reported before [173]. The large amount of wear particles in this experiment may be of the same origin. The detached copper may adhere to the Si_3N_4 sphere and then agglomerate at the interface in forms of loose wear particles. Due to the extreme environment (e.g. high stress level, local temperature, exposure to air) at the interface, these copper particles are more likely to be involved in a chemical reaction and oxidize prior to the bulk copper. These particles together with the possible wear particles of Si_3N_4 eventually form a refined structure (Fig. 3.19b) which appears to be nanocrystalline. Such a layer is widely reported in the literature and commonly referred to as the mechanical mixing layer [92, 105]. The existence of these wear particles makes the contact conditions much more complex than the situation using sapphire spheres. What remains conclusive, however, is that the oxygen (in form of O_2 or H_2O) in the air is the source of oxygen in the copper oxides at the sample surface.

4.3.3 Formation processes of the clusters at the surface

Following the same train of thought during the investigation of the subsurface microstructure evolution, the formation mechanisms of the clusters may very well be revealed at the very early stage of the sliding contact. The origin of the clusters is investigated after ten cycles of loading. No feature suggests any cluster or wavy layer at the surface in the HAADF image (Fig. 3.15a and Fig. 3.18a). The clusters may either be absent due to insufficient driving forces (low cycles of tribological loading), or be too small compared to surface roughness (RMS roughness around 4 nm) to be observed in this image. Some oxygen-rich areas, however, are visible in the EDXS oxygen map presented in Fig. 3.18b. They appear as a discontinuous, extremely thin layer with a thickness of less than 10 nm at the sample surface

(Fig. 3.18b, marked by red circles). Since such features were not observed in the unloaded material, this layer has formed during and due to the first ten cycles of tribological loading. It is interpreted as the precursor to the clusters observed in the later stages of sliding. This thin layer is almost certainly not formed after the tribological test since it would be expected to be more continuous then (Fig. 3.18b).

Based on the discussion above, the formation processes for the oxide clusters at the sample surface and therefore the tribologically-induced oxidation of copper, are hypothesized as follows:

The formation of Cu_2O is commonly reported as the first step in the oxidation of copper [174-176], and has been found in wear debris from a tribologically loaded copper coating [177]. In this thesis' case, it appears that amorphous cuprous oxide (Cu_2O) first grows in the form of small islands stochastically distributed over the tribologically loaded sample surface. The distribution of these islands at the sample surface is statistically random, as even though the sample preparation was performed with extreme caution, surface-defects, like surface steps, are expected to be randomly distributed at the sample surface. The surface area to volume ratio at these defects is higher than in the defect-free areas and the energy barrier for oxidation is therefore lower at these positions [178, 179]. The growth of individual oxide islands is also widely reported during the standard, non-tribologically induced, oxidation of copper [180-182].

In such a classical scenario, oxygen diffuses into copper through both the copper-ambient and the copper-copper oxide interface [183]. Under a tribological load, and as sliding progresses, these copper oxide nuclei grow into larger islands of amorphous Cu_2O at and into the sample surface, seen as the thin, oxygen-rich areas at the sample surface after ten sliding cycles (Fig. 3.18b). The exact mechanisms remain speculative. At the same time, literature [183] and this thesis' results suggest that beneath the surface, with an apparent lack of copper-oxygen

surface diffusion, the main path for oxygen to enter the material is the interface between copper and copper oxide. This suggests that oxidation is most effective along this interface, explaining the growth of copper oxide islands into hemispherical clusters as they were observed experimentally. Literature does not report values for the mechanical properties of amorphous copper oxides. For crystalline Cu_2O Young's moduli between 30-82 GPa were published [184-186]. Compared to the Young's modulus of copper (117 GPa), this might explain the lower friction forces observed experimentally once sliding happens mainly on copper oxide [49, 51, 70].

After the formation of the oxide islands, the later coming oxygen has the choice between pure copper surface and oxidized surface under tribological loading. If the oxygen favors entering the pure copper surface, new islands will form and the surface will soon be covered with a continuous layer. The absence of such a layer indicates that oxygen favors the oxidized surface. Since oxygen is mechanically driven into the sample surface by tribological loading, the non-trivial copper oxide phase in the clusters is in a condition neither as stable as with oxygen saturated in copper nor as Cu_2O compound. It may possess the tendency to further react into Cu_2O and is therefore more "oxygen-demanding" with a lower barrier for oxygen to enter. This can explain the oxygen's preference of oxidized surface to pure copper.

If the growth of the clusters is dominated by the surface diffusion of oxygen [175], the diffusion rate should be negatively correlated to the depth to the surface. This effect slows down the clusters' growth speed to the depth and encourage the parallel-to-surface growth of the oxide and eventually yields a continuous layer on the surface [183]. The result in this thesis shows that even after 5000 cycles, there is still some areas on the sample surface which is not covered by the clusters (Fig. 3.15c). This requires a much higher efficiency of oxidation at the Cu_2O-Cu interface, which is supported by the interface diffusion reported in the literature [183]. The higher Cu_2O-Cu interface oxidation efficiency, anyway, will

probably lead to a continuous layer at the surface in the future stages of tribological loading eventually (which is not covered in this thesis), but it can be reconciled with the hemispherical growth of the clusters This sequence of processes is illustrated in Figure 4.5. Interestingly, a similar sequence of events was suggested for the growth of an aqueous oxide on copper [174].

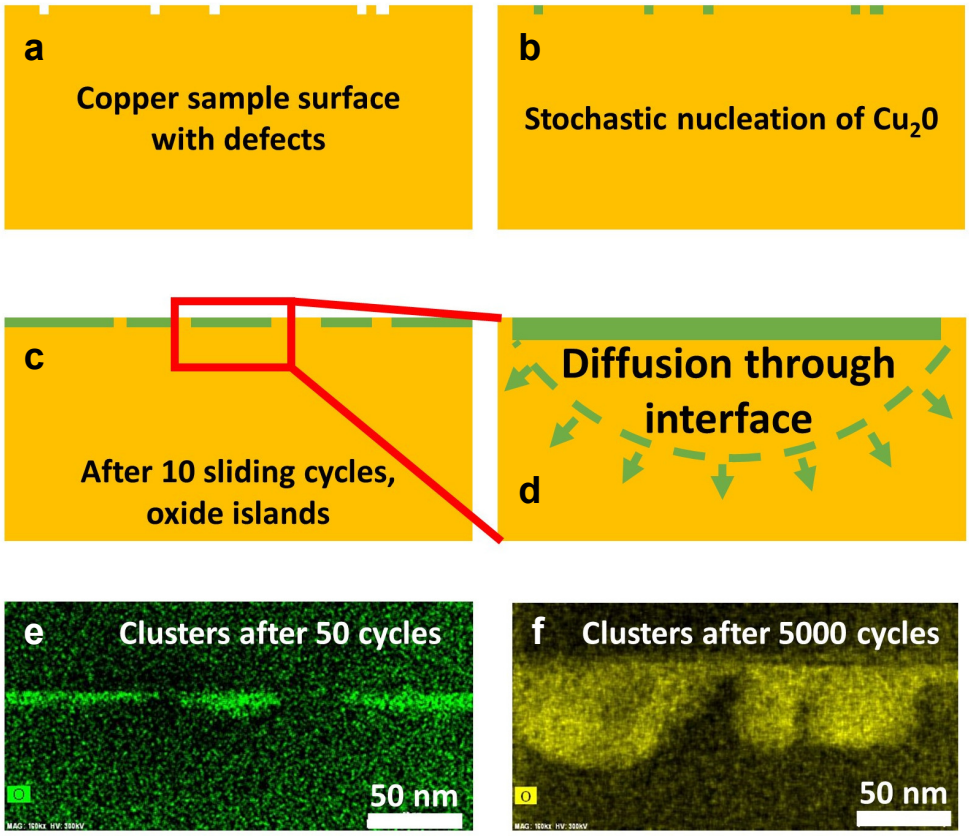

Figure 4.5: Diagram and EDXS oxygen maps illustrating the sequence of formation processes of the nanocrystalline / amorphous clusters. All images were presented in a cross-sectional view along the sliding direction. The orange blocks in (a-d) represent the copper sample. The green dots or lines represent the Cu_2O at the surface. (a) Randomly distributed defects at the sample's surface; (b) Stochastic formation of amorphous Cu_2O at the position of surface defects; (c) Growth of amorphous Cu_2O islands; (d) a zoom-in picture of the red rectangle in (c). The diffusion of oxygen through the cluster-copper interface is represented by the green arrows, and the hemispherical shape is illustrated by the green dashed line; (e) EDXS oxygen map after 50 cycles of loading [159]; (f) EDXS oxygen map after 5000 cycles of loading [159].

As part of this course of events, it is speculated that with an increasing volume of the amorphous copper oxide clusters, copper oxide nanocrystals start to nucleate inside the amorphous matrix due to the inherent thermodynamic instability of the amorphous phase. The assumption that the amorphous phase is generated first at the sample surface, then growing deeper into the material, followed by the nucleation of nanocrystals is supported by the TEM results for 50 sliding cycles (Fig. 3.16c). Here nanocrystalline / amorphous oxides together can be observed, whereas the oxygen-rich layer after ten cycles (Fig. 3.18b) is indirect evidence of the amorphous phase formed first. For such small cycle numbers, dislocations have just started to self-organize forming structures similar to small angle boundaries [70]. No grain refinement is observed yet [70]. This is a strong indication that the formation of these nanocrystalline / amorphous copper oxide clusters is not a subsequent process to grain refinement, as previously reported in the literature [77]. Generally, metal amorphization during tribological loading is not trivial, but has been demonstrated in atomic simulations [48, 94]. Also the mechanically driven amorphization of diamond has been reported experimentally [187, 188] and in simulations [73]. While the amorphization of copper is very rarely observed experimentally, it has been reported for experiments conducted at ultrahigh hydrostatic pressures [189]. Similar molecular dynamics simulations of copper embedded in a metallic glass, demonstrate the coexistence of amorphous and crystalline copper [190].

Chapter 5: Conclusions

Systematic work on the microstructure evolution in copper under tribological loading and its mechanisms as presented in this thesis has not been implemented in the literature before. A rational design of tribological systems from a materials science point of view has been hindered by this lack of fundamental knowledge, e.g. for the origin of microstructure changes and the different stages of the evolution progress. This thesis embarks on filling this gap and has made significant progress on understanding the elementary mechanisms for the microstructure evolution under tribological loading.

In summary and based directly on my observations, the following sequence of elementary processes governing the microstructural changes in copper under a mild tribological load is concluded:

1. The sliding contact between the sapphire sphere and the copper plate first generates and emits dislocations into the material. A significant amount of dislocations are emitted several micrometers deep into the material forming a deformed surface layer and this layer extends deeper with continued reciprocating loading.
2. Simultaneously a straight dislocation trace line forms during the very first sliding pass 100-150 nm beneath and parallel to the surface (Fig. 3.2+3.3). This dislocation self-organization is the very origin of the microstructural discontinuity commonly observed in the literature. The trace line's formation is explained by a contact mechanics model revealing a sign change in the stress field induced by the sliding contact (Fig. 4.2). For further tribological loading, this dislocation trace line accumulates successive dislocations resulting in an increase in misorientation.
3. With increasing sliding cycle number, for example after 100 cycles, the dislocation trace line evolves into a SAGB at a somewhat larger depth of around 200 nm (Fig. 3.13b).

4. With an additional increase in cycle number, GND networks begin to appear in the deformed layer for underneath the trace line of several micrometers. They evolve (Fig. 3.12f+h) into SAGBs which eventually form subgrains (Fig. 3.13c).

   It appears important to note that the formation of the dislocation trace line and the evolution of the GND density networks at greater depth underneath the surface must clearly be considered as two distinct processes.

5. Yet a separate process is surface oxidation. The formation mechanisms for surface oxides is dominated by mechanically driven chemical reactions and solid phase transformations, different to the ones for the dislocation activities.

It appears that any modelling aiming at predicting the performance of a tribosystem with respect to the evolution of friction and wear, especially during the early stages of sliding, must consider these different processes since each of them changes the local properties in a very significant way:

- The dislocation trace line is of importance not only as a precursor for all following microstructural changes, but it also initiates a spatial discontinuity in the shear resistance of the tribologically loaded material. The appearance of the discontinuity after the very first loading pass and its persistence in subsequent and cyclic passes [70] underlines its importance for the microstructure evolution and the importance that running-in [191] plays for the performance of a tribological system.
- The formation of SAGB and the evolving dislocation networks elucidate the progress of grain refinement during tribological loading which influences the level of friction force and the wear mechanisms. The three factors: grain size, stress field under tribological loading and friction force form a feed-back loop with their influence on each other [63].

- The nanocrystalline / amorphous clusters introduce a yet different phase in the contact area of as yet unknown mechanical properties. They may either be softer and act as a solid lubricant to lower friction and reduce wear [138], or be harder and more likely to cause cracks and delamination to happen. The understanding of their formation mechanisms will allow for modelling the reaction and tuning the surface for superior tribological performance.

Chapter 6: Outlook

This thesis contributes to the fundamental knowledge of microstructure evolution in ductile metals under tribological loading. It raises many interesting and valuable questions as well, inviting investigations for a further and deeper understanding of these processes. There is definitely more to come in this field and only some examples are given in this chapter.

The dislocation trace line discovered in this work is the very origin of the microstructural discontinuity in the subsurface area under tribological loading. However, one could even go further back to the very origin of the trace line. The subsurface microstructure after indentation does not show such a dislocation structure (in both experiments [192] and DDD simulations [97]). There must then be a point where the dislocation trace line initiates. By reducing the sliding distance, I believe that such a starting point can be discovered. This is of major interest because it will then reveal how the dislocations are organized into the trace line in detail.

The effect of grain boundaries on the appearance of the trace line has not been investigated in detail. Characterization of grain boundary types combining with a detailed study with the crystallographic orientation will bring insight into the formation mechanisms of the trace line. For example, the reason why the trace is absent in one of the grains may be explained crystallographically (Fig. 3.9c).

Since the model to explain the formation of the trace line in this thesis is purely based on the stress field under the sliding contact, further changing the loading conditions (e.g. varying the contact pressure by changing the diameter of the spheres and the normal load) would possibly show influences on the formation of the trace line (e.g. the misorientation across and the depth of the trace line). Even though the model does not indicate a strain rate dependence, strain rate (e.g. different sliding speeds) and temperature might be able to affect the formation of the trace line.

The contact mechanics model in this thesis for the formation of the trace line predicts the generality of the trace line and the trace line does show up for various conditions. Further changing the contact materials will support or challenge the generality of the trace line. For example, varying the elastic properties of the material should change the depth of the trace line within a predictable range. The trace line has only been observed in fcc metals such as α-brass (Cu-5wt.%Zn) and pure nickel in this work. Cross slip will be more challenging in materials with lower stacking fault energies (e.g. varying stacking fault energy can be simplified into varying the Zn content in an α-brass alloy), and slip systems are different in body-centered cubic (bcc) metals (e.g. pure iron). This hopefully will be the key to a generic law to describe the microstructure evolution in many metallic materials.

Since the samples used in this work are well annealed, the dislocations in the trace line are considered to be generated at the contacting surface and emitted into the material. Another possibility is that the trace line is formed by moving the existing dislocations in the material. It would be interesting to investigate the influence of the initial dislocation density in the sample on the formation of the trace line. This helps to elucidate the source of the dislocations forming the trace line. Samples which are plastically pre-deformed to different strains may serve this investigation properly by increasing the initial dislocation density. A long-term annealing process may allow for an even lower initial dislocation density compared to the samples in this work. This is a very decent point to collaborate with discrete dislocation dynamics (DDD) and molecular dynamics (MD) simulations. During modelling in simulations, the initial dislocation density as well as the crystallographic orientation of the sample with respect to the sliding direction can be very well defined.

The trace line is observed at a depth of 120-150 nm. The volume from the sample surface to the trace line is still very large to reproduce in simulations at the atomic scale. However, if the depth of the trace line can be tuned (e.g. by changing the sphere radius or the normal load)

up to very close to the surface, i.e. a few nanometers, MD simulations might be able to directly model its formation and will further lead to a full understanding of the elementary mechanisms behind the tribologically induced microstructure changes in the subsurface area.

More details of the mechanical properties and the tribological performance of the surface oxides should also be investigated. Understanding and controlling the surface chemical reactions will allow for superior tribological performance. For example, tribological tests on cuprous oxide bulk or thick films might reveal the friction and wear behavior of these materials. The effect of the surface oxidation on the tribological performance could then be interpreted more quantitatively.

Many achievements in tribology in history, like any other engineering subject, are mainly the results of empirical approaches to improve system performance. Thereby, methods for improving the performance of tribological systems have been found with great success. For example, via surface structure modification (i.e. laser surface texturing), friction forces can be reduced by more than 40% [144, 193, 194]. The microstructure in the subsurface area can also be designed into a gradient structure at the nanometer scale for low friction and little wear [136, 161, 195, 196]. The running-in process can be controlled and improved for better performance in later stages [81, 191, 197]. This direct and quick improvement in performance is indeed valuable. However, I do call here for more systematic investigations in the field aiming for a profound understanding of the elementary mechanisms behind these effects. Only this way, shall we be able to rationally design our materials, tune our surfaces, and revolutionarily boost the tribological performance of our systems. This is still a wide-open field and the accomplishments in this field will greatly contribute to our science, engineering and economy.

Bibliography

[1] B. Bhushan, Introduction to Tribology, John Wiley & Sons, New York, 2002.

[2] N. Lapusta, J.R. Rice, Y. Ben-Zion, G.T. Zheng, Elastodynamic analysis for slow tectonic loading with spontaneous rupture episodes on faults with rate- and state-dependent friction, J. Geophys. Res.-Solid Earth 105(B10) (2000) 23765-23789.

[3] T.D.B. Jacobs, R.W. Carpick, Nanoscale wear as a stress-assisted chemical reaction, Nat. Nanotechnol. 8(2) (2013) 108-112.

[4] M. Urbakh, J. Klafter, D. Gourdon, J. Israelachvili, The nonlinear nature of friction, Nature 430(6999) (2004) 525-528.

[5] K. Holmberg, P. Andersson, A. Erdemir, Global energy consumption due to friction in passenger cars, Tribol. Int. 47 (2012) 221-234.

[6] M.P. de Boer, T.M. Mayer, Tribology of MEMS, MRS Bull. 26(4) (2001) 302-304.

[7] R. Buscher, G. Tager, W. Dudzinski, B. Gleising, M.A. Wimmer, A. Fischer, Subsurface microstructure of metal-on-metal hip joints and its relationship to wear particle generation, J. Biomed. Mater. Res. B 72(1) (2005) 206-14.

[8] R. Pourzal, R. Theissmann, B. Gleising, S. Williams, A. Fischer, Micro-structural alterations in MoM hip implants, Mater. Sci. Forum 638-642 (2010) 1872-1877.

[9] Q.Y. Li, T.E. Tullis, D. Goldsby, R.W. Carpick, Frictional ageing from interfacial bonding and the origins of rate and state friction, Nature 480(7376) (2011) 233-U112.

[10] Z.L. Wang, Triboelectric nanogenerators as new energy technology and self-powered sensors - Principles, problems and perspectives, Faraday Discussions 176(0) (2014) 447-458.

[11] Y. Qin, X.D. Wang, Z.L. Wang, Microfibre-nanowire hybrid structure for energy scavenging, Nature 451(7180) (2008) 809-U5.

[12] M. Dienwiebel, G.S. Verhoeven, N. Pradeep, J.W.M. Frenken, J.A. Heimberg, H.W. Zandbergen, Superlubricity of graphite, Phys. Rev. Lett. 92(12) (2004) 126101.

[13] J. Yang, Z. Liu, F. Grey, Z. Xu, X. Li, Y. Liu, M. Urbakh, Y. Cheng, Q. Zheng, Observation of high-speed microscale superlubricity in graphite, Phys. Rev. Lett. 110(25) (2013) 255504.

[14] C. Lee, Q. Li, W. Kalb, X.-Z. Liu, H. Berger, R.W. Carpick, J. Hone, Frictional characteristics of atomically thin sheets, Science 328(5974) (2010) 76-80.

[15] D. Berman, A. Erdemir, A.V. Sumant, Few layer graphene to reduce wear and friction on sliding steel surfaces, Carbon 54 (2013) 454-459.

[16] I.M. Hutchings, Leonardo da Vinci′s studies of friction, Wear 360–361 (2016) 51-66.

[17] A. Fall, B. Weber, M. Pakpour, N. Lenoir, N. Shahidzadeh, J. Fiscina, C. Wagner, D. Bonn, Sliding friction on wet and dry sand, Phys. Rev. Lett. 112(17) (2014) 175502.

[18] H.P. Jost, Lubrication: Tribology; Education and Research; Report on the Present Position and Industry's Needs (submitted to the Department of Education and Science by the Lubrication Engineering and Research) Working Group, HM Stationery Office1966.

[19] J. Field, David Tabor. 23 October 1913 — 26 November 2005, Biographical Memoirs of Fellows of the Royal Society 54 (2008) 425-459.

[20] H. Hertz, Ueber die Beruhrung fester elastischer Korper, J. Reine Angew. Math. 92 (1882) 16.

[21] J.N. Israelachvili, Intermolecular and Surface Forces, Academic press 2011.

[22] N. Gane, J. Skinner, Generation of dislocations in metals under a sliding contact and dissipation of frictional energy, Wear 25(3) (1973) 381-384.

[23] K. Autumn, Y.A. Liang, S.T. Hsieh, W. Zesch, W.P. Chan, T.W. Kenny, R. Fearing, R.J. Full, Adhesive force of a single gecko foot-hair, Nature 405(6787) (2000) 681-685.

[24] D. Maugis, Contact, Adhesion and Rupture of Elastic Solids, Springer-Verlag Berlin Heidelberg, Berlin Heidelberg, 2013.

[25] K.L. Johnson, Contact Mechanics, Cambridge University Press, Cambridge, 1987.

[26] D. Tabor, Surface forces and surface interactions, J. Colloid Interface Sci. 58(1) (1977) 2-13.

[27] R.D. Mindlin, Complicance of elastic bodies in contact, J. Appl. Mech. Trans. ASME 16(3) (1949) 259-268.

[28] G.M. Hamilton, L.E. Goodman, Stress field created by a circular sliding contact, J. Appl. Mech. 33(2) (1966) 371-&.

[29] G.M. Hamilton, Explicit equations for the stresses beneath a sliding spherical contact, Proc. Inst Mech. Eng. C, 197(MAR) (1983) 53-59.

[30] H. Kong, M.F. Ashby, Wear mechanisms in brittle solids, Acta Metall. Mater. 40(11) (1992) 2907-2920.

[31] M. Barletta, L. Lusvarghi, F.P. Mantini, G. Rubino, Epoxy-based thermosetting powder coatings: Surface appearance, scratch adhesion and wear resistance, Surf. Coat. Technol. 201(16-17) (2007) 7479-7504.

[32] H.A. Padilla, B.L. Boyce, C.C. Battaile, S.V. Prasad, Frictional performance and near-surface evolution of nanocrystalline Ni-Fe as governed by contact stress and sliding velocity, Wear 297(1-2) (2013) 860-871.

[33] T.J. Rupert, C.A. Schuh, Sliding wear of nanocrystalline Ni-W: Structural evolution and the apparent breakdown of Archard scaling, Acta Mater. 58(12) (2010) 4137-4148.

[34] J.H. Dieterich, B.D. Kilgore, Direct observation of frictional contacts: new insights for state-dependent properties, Pure Appl. Geophys. 143(1-3) (1994) 283-302.

[35] W.G. Sawyer, K.J. Wahl, Accessing inaccessible interfaces: In situ approaches to materials tribology, MRS Bull. 33(12) (2008) 1145-1148.

[36] I. Szlufarska, M. Chandross, R.W. Carpick, Recent advances in single-asperity nanotribology, J. Phys. D Appl. Phys. 41(12) (2008) 123001.

[37] Y.F. Mo, K.T. Turner, I. Szlufarska, Friction laws at the nanoscale, Nature 457(7233) (2009) 1116-1119.

[38] L. Pastewka, M.O. Robbins, Contact between rough surfaces and a criterion for macroscopic adhesion, PNAS 111(9) (2014) 3298-3303.

[39] S. Li, Q. Li, R.W. Carpick, P. Gumbsch, X.Z. Liu, X. Ding, J. Sun, J. Li, The evolving quality of frictional contact with graphene, Nature 539(7630) (2016) 541-545.

[40] Q. Li, Y. Dong, D. Perez, A. Martini, R.W. Carpick, Speed dependence of atomic stick-slip friction in optimally matched experiments and molecular dynamics simulations, Phys. Rev. Lett. 106(12) (2011) 126101.

[41] R. Bennewitz, Friction force microscopy, Fundamentals of Friction and Wear on the Nanoscale, Springer 2015, pp. 3-16.

[42] Y. Liao, E. Hoffman, L.D. Marks, Nanoscale abrasive wear of CoCrMo in in-situ TEM sliding, Tribol. Lett. 57(28) (2015).

[43] T. Junge, J.-F. Molinari, Plastic activity in nanoscratch molecular dynamics simulations of pure aluminium, Int. J. Plasticity 53 (2014) 90-106.

[44] Y.L. Dong, Q.Y. Li, A. Martini, Molecular dynamics simulation of atomic friction: A review and guide, J. Vac. Sci. Technol. A 31(3) (2013) 24.

[45] Y. Mo, I. Szlufarska, Nanoscale heat transfer: Single hot contacts, Nat. Mater. 12(1) (2013) 9-11.

[46] P. Stoyanov, P.A. Romero, T.T. Jarvi, L. Pastewka, M. Scherge, P. Stemmer, A. Fischer, M. Dienwiebel, M. Moseler, Experimental and numerical atomistic investigation of the third body formation process in dry tungsten/tungsten-carbide tribo couples, Tribol. Lett. 50(1) (2013) 67-80.

[47] X.Z. Liu, Z. Ye, Y. Dong, P. Egberts, R.W. Carpick, A. Martini, Dynamics of atomic stick-slip friction examined with atomic force microscopy and atomistic simulations at overlapping speeds, Phys. Rev. Lett. 114(14) (2015) 146102.

[48] X. Hu, M.V.P. Altoe, A. Martini, Amorphization-assisted nanoscale wear during the running-in process, Wear 370–371 (2017) 46-50.

[49] W.G. Sawyer, N. Argibay, D.L. Burris, B.A. Krick, Mechanistic studies in friction and wear of bulk materials, Ann. Rev. Mater. Res. 44 (2014) 395-427.

[50] L. Nicola, Y. Xiang, J.J. Vlassak, E. Van der Giessen, A. Needleman, Plastic deformation of freestanding thin films: Experiments and modeling, J. Mech. Phys. Solids 54(10) (2006) 2089-2110.

[51] F.P. Bowden, D. Tabor, The Friction and Lubrication of Solids, Clarendon Press, Oxford, 1950.

[52] F. Bowden, D. Tabor, Mechanism of metallic friction, Nature 150(3798) (1942) 197-199.

[53] D.A. Rigney, W.A. Glaeser, Significance of near-surface microstructure in wear process, Wear 46(1) (1978) 241-250.

[54] D.A. Rigney, J.P. Hirth, Plastic deformation and sliding friction of metals, Wear 53(2) (1979) 345-370.

[55] K.-H. Zum Gahr, Formation of wear debris by the abrasion of ductile metals, Wear 74(2) (1981) 353-373.

[56] T. Hattori, Y. Kaneko, S. Hashimoto, Wear-induced microstructure in Ni/Cu nano-multilayers, J. Mater. Sci. 43(11) (2008) 3923-3930.

[57] P. Stoyanov, P.A. Romero, R. Merz, M. Kopnarski, M. Stricker, P. Stemmer, M. Dienwiebel, M. Moseler, Nano scale sliding friction phenomena at the interface of diamond-like carbon and tungsten, Acta Mater. 67 (2014) 395-408.

[58] D.A. Hughes, N. Hansen, Graded nanostructures produced by sliding and exhibiting universal behavior, Phys. Rev. Lett. 87(13) (2001) 135503.

[59] Z.P. Luo, G.P. Zhang, R. Schwaiger, Microstructural vortex formation during cyclic sliding of Cu/Au multilayers, Scr. Mater. 107 (2015) 67-70.

[60] S. Korres, T. Feser, M. Dienwiebel, In situ observation of wear particle formation on lubricated sliding surfaces, Acta Mater. 60(1) (2012) 420-429.

[61] D.A. Hughes, N. Hansen, Exploring the limit of dislocation based plasticity in nanostructured metals, Phys. Rev. Lett. 112(13) (2014) 135504.

[62] S. Karthikeyan, H.J. Kim, D.A. Rigney, Velocity and strain-rate profiles in materials subjected to unlubricated sliding, Phys. Rev. Lett. 95(10) (2005) 106001.

[63] N. Argibay, M. Chandross, S. Cheng, J.R. Michael, Linking microstructural evolution and macro-scale friction behavior in metals, J. Mater. Sci. 52(5) (2017) 2780-2799.

[64] D.A. Rigney, X.Y. Fu, J.E. Hammerberg, B.L. Holian, M.L. Falk, Examples of structural evolution during sliding and shear of ductile materials, Scr. Mater. 49(10) (2003) 977-983.

[65] P. Heilmann, W.A.T. Clark, D.A. Rigney, Orientation determination of subsurface cells generated by sliding, Acta Metall.31(8) (1983) 1293-1305.

[66] B. Bay, N. Hansen, D.A. Hughes, D. Kuhlmann-Wilsdorf, Evolution of F.C.C. deformations structures in polyslip, Acta Metall. Mater. 40(2) (1992) 205-219.

[67] W. Cai, P. Bellon, Microstructural self-organization triggered by twin boundaries during dry sliding wear, Acta Mater. 60(19) (2012) 6673-6684.

[68] N. Argibay, T.A. Furnish, B.L. Boyce, B.G. Clark, M. Chandross, Stress-dependent grain size evolution of nanocrystalline Ni-W and its impact on friction behavior, Scr. Mater. 123 (2016) 26-29.

[69] S. Brinckmann, C.A.C. Fink, G. Dehm, Nanotribology in austenite: Normal force dependence, Wear 338 (2015) 430-435.

[70] C. Greiner, Z. Liu, L. Strassberger, P. Gumbsch, Sequence of stages in the microstructure evolution in copper under mild reciprocating tribological loading, ACS Appl. Mater. Interfaces 8(24) (2016) 15809-19.

[71] S.V. Prasad, J.K. Michael, T.R. Christenson, EBSD studies on wear-induced subsurface regions in LIGA nickel, Scr. Mater. 48(3) (2003) 255-260.

[72] W. Cai, P. Bellon, Subsurface microstructure evolution and deformation mechanism of Ag-Cu eutectic alloy after dry sliding wear, Wear 303(1-2) (2013) 602-610.

[73] L. Pastewka, S. Moser, P. Gumbsch, M. Moseler, Anisotropic mechanical amorphization drives wear in diamond, Nat. Mater. 10(1) (2011) 34-38.

[74] A. Emge, S. Karthikeyan, H.J. Kim, D.A. Rigney, The effect of sliding velocity on the tribological behavior of copper, Wear 263 (2007) 614-618.

[75] D. Turley, L. Samuels, The nature of mechanically polished surfaces of copper, Metallography 14(4) (1981) 275-294.

[76] D. Hughes, D. Dawson, J. Korellis, L. Weingarten, A microstructurally based method for stress estimates, Wear 181 (1995) 458-468.

[77] A. Emge, S. Karthikeyan, D.A. Rigney, The effects of sliding velocity and sliding time on nanocrystalline tribolayer development and properties in copper, Wear 267(1-4) (2009) 562-567.

[78] M.S. Bednar, D. Kuhlmann-Wilsdorf, Amorphous and alloy film formation in sliding of silver on copper, Wear 181 (1995) 922-937.

[79] W.L. Li, N.R. Tao, Z. Han, K. Lu, Comparisons of dry sliding tribological behaviors between coarse-grained and nanocrystalline copper, Wear 274 (2012) 306-312.

[80] R. Buscher, A. Fischer, The pathways of dynamic recrystallization in all-metal hip joints, Wear 259 (2005) 887-897.

[81] D. Linsler, T. Schlarb, T. Weingartner, M. Scherge, Influence of subsurface microstructure on the running-in of an AlSi alloy, Wear 332 (2015) 926-931.

[82] A. Brink, K. Lichtenberg, M. Scherge, The influence of the initial near-surface microstructure and imposed stress level on the running-in characteristics of lubricated steel contacts, Wear 360–361 (2016) 114-120.

[83] D. Shakhvorostov, L. Jian, E. Nold, G. Beuchle, M. Scherge, Influence of Cu grain size on running-in related phenomena, Tribol. Lett. 28(3) (2007) 307-318.

[84] K.L. Hsu, T.M. Ahn, D.A. Rigney, Friction, wear and microstructure of unlubricated austenitic stainless steels, Wear 60(1) (1980) 13-37.

[85] A.H. Advani, J.C. Arroyo, L.E. Murr, S.K. Varma, L. Montes, C. Odegard, Transmission electron-microscopy of scratch-induced surface deformation microstructures in austenitic Fe-Cr-Ni alloys, Scr. Metall. Mater. 26(8) (1992) 1181-1186.

[86] A. Fischer, S. Weiss, M.A. Wimmer, The tribological difference between biomedical steels and CoCrMo-alloys, J. Mech. Behav. Biomed. Mater. 9 (2012) 50-62.

[87] M. Hahn, C. Bauer, R. Theissmann, B. Gleising, W. Dudzinski, A. Fischer, The impact of microstructural alterations at spray coated cylinder running surfaces of diesel engines–Findings from motor and laboratory benchmark tests, Wear 271(9) (2011) 2599-2609.

[88] D. Hughes, N. Hansen, Microstructural evolution in nickel during rolling from intermediate to large strains, Metall. Trans. A 24(9) (1993) 2022-2037.

[89] A.V. Chumaevsky, D.V. Lychagin, S.Y. Tarasov, A.G. Melnikov, Fragmentation, texturing and plastic flow in the subsurface of friction-processed copper single crystal, Adv. Mater. Res. 872 (2013) 30-35.

[90] M. Long, H.J. Rack, Subsurface deformation and microcrack formation in Ti-35Nb-8Zr-5Ta-O(x) during reciprocating sliding wear, Mater. Sci. Eng. C 25(3) (2005) 382-388.

[91] J.B. Singh, W. Cai, P. Bellon, Dry sliding of Cu-15 wt%Ni-8 wt%Sn bronze: Wear behaviour and micro structures, Wear 263 (2007) 830-841.

[92] X. Chen, Z. Han, K. Lu, Wear mechanism transition dominated by subsurface recrystallization structure in Cu-Al alloys, Wear 320 (2014) 41-50.

[93] J.E. Hammerberg, B.L. Holian, T.C. Germann, R. Ravelo, Nonequilibrium molecular dynamics simulations of metallic friction at Ta/Al and Cu/Ag interfaces, Metall. Mater. Trans. A 35A(9) (2004) 2741-2745.

[94] S. Karthikeyan, A. Agrawal, D.A. Rigney, Molecular dynamics simulations of sliding in an Fe-Cu tribopair system, Wear 267(5-8) (2009) 1166-1176.

[95] P.A. Romero, T.T. Jarvi, N. Beckmann, M. Mrovec, M. Moseler, Coarse graining and localized plasticity between sliding nanocrystalline metals, Phys. Rev. Lett. 113 (2014) 036101.

[96] N. Beckmann, P.A. Romero, D. Linsler, M. Dienwiebel, U. Stolz, M. Moseler, P. Gumbsch, Origins of folding instabilities on polycrystalline metal surfaces, Phys. Rev. Appl. 2(6) (2014) 064004.

[97] J. Gagel, D. Weygand, P. Gumbsch, Formation of extended prismatic dislocation structures under indentation, Acta Mater. 111 (2016) 399-406.

[98] J. Gagel, Personal communication: black line / network, 2016.

[99] D.A. Rigney, S. Karthikeyan, The evolution of tribomaterial during sliding: A brief introduction, Tribol. Lett. 39(1) (2010) 3-7.

[100] J.L. Young, D. Kuhlmann-Wilsdorf, R. Hull, The generation of mechanically mixed layers (MMLs) during sliding contact and the effects of lubricant thereon, Wear 246(1-2) (2000) 74-90.

[101] D. Shakhvorostov, K. Pohlmann, M. Scherge, Structure and mechanical properties of tribologically induced nanolayers, Wear 260(4-5) (2006) 433-437.

[102] D.A. Rigney, Large strains associated with sliding contact of metals, Mater. Res. Innov. 1(4) (1998) 231-234.

[103] D.A. Rigney, M.G.S. Naylor, R. Divakar, L.K. Ives, Low energy dislocation structures caused by sliding and by particle impact, Mater. Sci. Eng. 81(1-2) (1986) 409-425.

[104] D. Hughes, Microstructure and flow stress of deformed polycrystalline metals, Scr. Metall. Mater. 27(8) (1992) 969-974.

[105] D.A. Hughes, D.B. Dawson, J.S. Korellis, L.I. Weingarten, Near surface microstructures developing under large sliding loads, J. Mater. Eng. Perform. 3(4) (1994) 459-475.

[106] D.A. Hughes, N. Hansen, Deformation structures developing on fine scales, Philos. Mag. 83(31-34) (2003) 3871-3893.

[107] B. Yao, Z. Han, K. Lu, Correlation between wear resistance and subsurface recrystallization structure in copper, Wear 294 (2012) 438-445.

[108] M. Chamani, G.H. Farrahi, M.R. Movahhedy, Friction behavior of nanocrystalline nickel near the Hall-Petch breakdown, Tribol. Int. 107 (2017) 18-24.

[109] T.J. Rupert, W.J. Cai, C.A. Schuh, Abrasive wear response of nanocrystalline Ni-W alloys across the Hall-Petch breakdown, Wear 298 (2013) 120-126.

[110] U.F. Kocks, C.N. Tomé, H.-R. Wenk, Texture and Anisotropy: Preferred Orientations in Polycrystals and Their Effect on Materials Properties, Cambridge University Press, Cambridge, 2000.

[111] J. Shang, W.L. Ma, J.J. Lu, Comparison of the tribological behavior of columnar-grained polycrystalline copper with vertical/horizontal orientation sliding against AISI 1045 steel, Wear 297(1-2) (2013) 818-823.

[112] Y. Tsuya, Anisotropy of coefficient of friction and plastic deformation in copper single crystals, Wear 14(5) (1969) 309-322.

[113] V.D. Scott, H. Wilman, Surface re-orientation caused on metals by abrasion - its nature, origin and relation to friction and wear, Proc. R. Soc. London Ser. A 247(1250) (1958) 353-368.

[114] Z.N. Farhat, Contribution of crystallographic texturing to the sliding friction behaviour of fcc and hcp metals, Wear 250 (2001) 401-408.

[115] P.L. Menezes, Kishore, S.V. Kailas, Role of surface texture of harder surface on subsurface deformation, Wear 266(1-2) (2009) 103-109.

[116] M. Goto, M. Sasaki, A. Kasahara, M. Tosa, Frictional property depended on crystal preferred orientation analyzed by a combinatorial technique, Tribol. Lett. 55(2) (2014) 289-293.

[117] W. Cai, J. Mabon, P. Bellon, Crystallographic textures and texture transitions induced by sliding wear in bronze and nickel, Wear 267(1-4) (2009) 485-494.

[118] Y. Ohno, J. Inotani, Y. Kaneko, S. Hashimoto, Orientation dependence of high-angle grain boundary formation during sliding wear in copper single crystals, J. Jpn. Inst. Met. 74(6) (2010) 384-391.

[119] S.Y. Tarasov, D.V. Lychagin, A.V. Chumaevskii, Orientation dependence of subsurface deformation in dry sliding wear of Cu single crystals, Appl. Surf. Sci. 274 (2013) 22-26.

[120] S. Tarasov, V. Rubtsov, A. Kolubaev, Subsurface shear instability and nanostructuring of metals in sliding, Wear 268(1-2) (2010) 59-66.

[121] N.K. Sundaram, Y. Guo, S. Chandrasekar, Mesoscale folding, instability, and disruption of laminar flow in metal surfaces, Phys. Rev. Lett. 109(10) (2012) 106001.

[122] Y. Guo, W.D. Compton, S. Chandrasekar, In situ analysis of flow dynamics and deformation fields in cutting and sliding of metals, Proc. R. Soc. A 471(2178) (2015) 18.

[123] J.D. Honeycutt, H.C. Andersen, Molecular dynamics study of melting and freezing of small Lennard-Jones clusters, J. Phys. Chem. 91(19) (1987) 4950-4963.

[124] Y. Zhu, D. Kuhlmann-Wilsdorf, T. Imura, Determining subsurface stress distributions in tribological samples from dislocation cell sizes in low energy dislocation structures, Mater. Sci. Eng. A 113 (1989) 297-303.

[125] K. Wang, N.R. Tao, G. Liu, J. Lu, K. Lu, Plastic strain-induced grain refinement at the nanometer scale in copper, Acta Mater. 54(19) (2006) 5281-5291.

[126] K. Wolff, Z. Liu, D. Braun, J. Schneider, C. Greiner, Chronology of the microstructure evolution for pearlitic steel under unidirectional tribological loading, Tribol. Int. 102 (2016) 540-545.

[127] H. Sato, Y. Noda, Y. Watanabe, 3-Dimensional microstructural evaluation of wear-Induced layer in Al-Al3Ti functionally graded materials by serial sectioning, Mater. Trans. 54(8) (2013) 1274-1280.

[128] F. Dupont, I. Finnie, The simulation of sliding wear by cyclic deformation - microstructural aspects, Wear 140(1) (1990) 93-106.

[129] S.O. Hyatt, T.R. Bieler, The effect of a superimposed strain field on frictional texture measurements, Wear 184(2) (1995) 245-247.

[130] M.R. Bateni, J.A. Szpunar, X. Wang, D.Y. Li, Texture changes of carbon steel and stainless steel as a result of wear, in: P.V. Houtte, L. Kestens (Eds.), Icotom 14: Textures of Materials, Pts 1and 22005, pp. 441-446.

[131] D. Santhiya, Z. Burghard, C. Greiner, L.P.H. Jeurgens, T. Subkowski, J. Bill, Bioinspired deposition of TiO2 thin films induced by hydrophobins, Langmuir 26(9) (2010) 6494-6502.

[132] J.M. Jungk, J.R. Michael, S.V. Prasad, The role of substrate plasticity on the tribological behavior of diamond-like nanocomposite coatings, Acta Mater. 56(9) (2008) 1956-1966.

[133] N.N. Gosvami, J.A. Bares, F. Mangolini, A.R. Konicek, D.G. Yablon, R.W. Carpick, Mechanisms of antiwear tribofilm growth revealed in situ by single-asperity sliding contacts, Science 348(6230) (2015) 102-106.

[134] J. Li, A. Elmadagli, V.Y. Gertsman, J. Lo, A.T. Alpas, FIB and TEM characterization of subsurfaces of an Al-Si alloy (A390) subjected to sliding wear, Mater. Sci. Eng. A 421(1-2) (2006) 317-327.

[135] Z.N. Farhat, Y. Ding, D.O. Northwood, A.T. Alpas, Effect of grain size on friction and wear of nanocrystalline aluminum, Mater. Sci. Eng. A 206(2) (1996) 302-313.

[136] X. Chen, Z. Han, K. Lu, Enhancing wear resistance of Cu-Al alloy by controlling subsurface dynamic recrystallization, Scr. Mater. 101 (2015) 76-79.

[137] P. Stoyanov, D. Linsler, T. Schlarb, M. Scherge, R. Schwaiger, Dependence of tribofilm characteristics on the running-in behavior of aluminum-silicon alloys, J. Mater. Sci. 50(16) (2015) 5524-5532.

[138] A. Erdemir, A crystal-chemical approach to lubrication by solid oxides, Tribol. Lett. 8(2-3) (2000) 97-102.

[139] P.J. Jackson, Z.S. Basinski, Latent hardening and flow stress in copper single crystals, Can. J. Phys. 45(2P2) (1967) 707-735.

[140] H. Mughrabi, Cyclic hardening and saturation behavior of copper single crystals, Mater. Sci. Eng. 33(2) (1978) 207-223.

[141] L. Lu, X. Chen, X. Huang, K. Lu, Revealing the Maximum Strength in Nanotwinned Copper, Science 323(5914) (2009) 607-610.

[142] J. Jiang, T.B. Britton, A.J. Wilkinson, The orientation and strain dependence of dislocation structure evolution in monotonically deformed polycrystalline copper, Int. J. Plasticity 69 (2015) 102-117.

[143] R.D. Elena, A. Leonid, A. Lytvynov, Sapphire: Material, Manufacturing, Applications, New York: Springer Science and Business Media, LLC, 2009.

[144] C. Greiner, M. Schafer, U. Popp, P. Gumbsch, Contact splitting and the effect of dimple depth on static friction of textured surfaces, ACS Appl. Mate. Interfaces 6(11) (2014) 7986-90.

[145] P. Schreiber, Personal communication: Schematic diagram of the tribological contact. , (2016).

[146] J. Mayer, L.A. Giannuzzi, T. Kamino, J. Michael, TEM sample preparation and FIB-induced damage, MRS Bull. 32(5) (2007) 400-407.

[147] S. Schreijag, D. Kaufmann, M. Wenk, O. Kraft, R. Monig, Size and microstructural effects in the mechanical response of alpha-Fe and low alloyed steel, Acta Mater. 97 (2015) 94-104.

[148] R. Hielscher, H. Schaeben, A novel pole figure inversion method: specification of the MTEX algorithm, J. Appl. Crystallogr. 41 (2008) 1024-1037.

[149] P.W. Trimby, Y. Cao, Z.B. Chen, S. Han, K.J. Hemker, J.S. Lian, X.Z. Liao, P. Rottmann, S. Samudrala, J.L. Sun, J.T. Wang, J. Wheeler, J.M. Cairney, Characterizing deformed ultrafine-grained and nanocrystalline materials using transmission Kikuchi diffraction in a scanning electron microscope, Acta Mater. 62 (2014) 69-80.

[150] E. Demir, D. Raabe, N. Zaafarani, S. Zaefferer, Investigation of the indentation size effect through the measurement of the geometrically necessary dislocations beneath small indents of different depths using EBSD tomography, Acta Mater. 57(2) (2009) 559-569.

[151] L.P. Kubin, A. Mortensen, Geometrically necessary dislocations and strain-gradient plasticity: a few critical issues, Scr. Mater. 48(2) (2003) 119-125.

[152] H.J. Gao, Y.G. Huang, Geometrically necessary dislocation and size-dependent plasticity, Scr. Mater. 48(2) (2003) 113-118.

[153] H. Gao, Y. Huang, W.D. Nix, J.W. Hutchinson, Mechanism-based strain gradient plasticity - I. Theory, J. Mech. Phys. Solids 47(6) (1999) 1239-1263.

[154] M. Calcagnotto, D. Ponge, E. Demir, D. Raabe, Orientation gradients and geometrically necessary dislocations in ultrafine grained dual-phase steels studied by 2D and 3D EBSD, Mater. Sci. Eng. A 527(10-11) (2010) 2738-2746.

[155] A. Wimmer, W. Heinz, T. Detzel, W. Robl, M. Nellessen, C. Kirchlechner, G. Dehm, Cyclic bending experiments on free-standing Cu micron lines observed by electron backscatter diffraction, Acta Mater. 83(0) (2015) 460-469.

[156] R. Schneider, Personal communication: (HR)TEM investigation of the dislocation trace line, (2015).

[157] P. Messer, K. Hahn, Personal communication, (2015).

[158] L. Strassberger, Personal communication: TEM investigations on coppper's subsurface area under tribological loading, (2014).

[159] C. Patzig, T. Hoeche, Personal communication: TEM investigation on the subsurface chemistry, (2016).

[160] D. Hull, D.J. Bacon, Introduction to Dislocations, Elsevier 2011.

[161] S.Q. Deng, A. Godfrey, W. Liu, N. Hansen, A gradient nanostructure generated in pure copper by platen friction sliding deformation, Scr. Mater. 117 (2016) 41-45.

[162] L. Pastewka, Personal communication: Model for the formation of the dislocation trace line in the subsurface area of copper under tribological loading, (2016).

[163] R. Hull, Finite element analysis of stress relaxation in thin foil plan-view transmission electron microscopy specimens, Appl. Phys. Lett. 63(16) (1993) 2291-2293.

[164] B. Masters, Dislocation loops in irradiated iron, Nature 200(4903) (1963) 254-254.

[165] W. Wu, Free surface effects in TEM imaging of dislocation lines and loops in Fe, (2014).

[166] M. Schäfer, Personal communication, (2014).

[167] Y. Wang, D. Raabe, C. Klüber, F. Roters, Orientation dependence of nanoindentation pile-up patterns and of nanoindentation microtextures in copper single crystals, Acta Mater. 52(8) (2004) 2229-2238.

[168] W.P. Dong, E.J. Davis, D.L. Butler, K.J. Stout, Topographic features of cylinder liners - An application of three-dimensional characterization techniques, Tribol. Int. 28(7) (1995) 453-463.

[169] Y.L. Liu, L.J. Gui, S. Jin, Ab initio investigation of the mechanical properties of copper, Chin. Phys. B 21(9) (2012) 6.

[170] C.N. Reid, J.L. Routbort, Malleability and plastic anisotropy of iridium and copper, Metall. Trans. 3(8) (1972) 2257-2260.

[171] J. Neumann, T. Zhong, Y. Chang, The Cu− O (Copper-Oxygen) system, J. Phase Equilib. 5(2) (1984) 136-140.

[172] F. Reichel, L. Jeurgens, E. Mittemeijer, Thermodynamic modeling of the initial microstructural evolution of oxide films grown on bare copper, Thin Solid Films 516(7) (2008) 1457-1460.

[173] I. Khader, A. Hashibon, J.M. Albina, A. Kailer, Wear and corrosion of silicon nitride rolling tools in copper rolling, Wear 271(9-10) (2011) 2531-2541.

[174] Y. Chu, I. Robinson, A. Gewirth, Comparison of aqueous and native oxide formation on Cu (111), J. Chem. Phys. 110(12) (1999) 5952-5959.

[175] S.-K. Lee, H.-C. Hsu, W.-H. Tuan, Oxidation behavior of copper at a temperature below 300° C and the methodology for passivation, Mater. Res. 19(1) (2016) 51-56.

[176] A. Soon, M. Todorova, B. Delley, C. Stampfl, Thermodynamic stability and structure of copper oxide surfaces: A first-principles investigation, Phys. Rev. B 75(12) (2007) 125420.

[177] Y. Zhang, J.M. Shockley, P. Vo, R.R. Chromik, Tribological behavior of a cold-sprayed Cu–MoS2 composite coating during dry sliding wear, Tribol. Lett. 62(1) (2016) 9.

[178] G. Zhou, L. Luo, L. Li, J. Ciston, E.A. Stach, J.C. Yang, Step-edge-induced oxide growth during the oxidation of Cu surfaces, Phys. Rev. Lett. 109(23) (2012) 235502.

[179] C.P. León, C. Sürgers, H.v. Löhneysen, Formation of copper oxide surface structures via pulse injection of air onto Cu (111) surfaces, Phys. Rev. B 85(3) (2012) 035434.

[180] R. Milne, A. Howie, Electron microscopy of copper oxidation, Philos. Mag. A 49(5) (1984) 665-682.

[181] J. Ho, R. Vook, (111) Cu2O growth modes on (111) Cu surfaces, J. Cryst. Growth 44(5) (1978) 561-569.

[182] G. Zhou, TEM investigation of interfaces during cuprous island growth, Acta Mater. 57(15) (2009) 4432-4439.

[183] J. Yang, B. Kolasa, J. Gibson, M. Yeadon, Self-limiting oxidation of copper, Appl. Phys. Lett. 73(19) (1998) 2841-2843.

[184] J. Hallberg, R. Hanson, The elastic constants of cuprous oxide, Phys. Status Solidi (b) 42(1) (1970) 305-310.

[185] M. Manghnani, W. Brower, H. Parker, Anomalous elastic behavior in Cu_2O under pressure, Phys. Status Solidi (a) 25(1) (1974) 69-76.

[186] S.-R. Jian, G.-J. Chen, W.-M. Hsu, Mechanical properties of Cu_2O thin films by nanoindentation, Materials 6(10) (2013) 4505-4513.

[187] X.Y. Zhang, R. Schneider, E. Muller, M. Mee, S. Meier, P. Gumbsch, D. Gerthsen, Electron microscopic evidence for a tribologically induced phase transformation as the origin of wear in diamond, J. Appl. Phys. 115(6) (2014) 063508.

[188] M.I.D. Bouchet, C. Matta, B. Vacher, T. Le-Mogne, J.M. Martin, J. von Lautz, T. Ma, L. Pastewka, J. Otschik, P. Gumbsch, M. Moseler, Energy filtering transmission electron microscopy and atomistic simulations of tribo-induced hybridization change of nanocrystalline diamond coating, Carbon 87 (2015) 317-329.

[189] H. Furuichi, E. Ito, Y. Kanno, S. Watanabe, T. Katsura, N. Fujii, Amorphous copper formation and related phenomena at ultrahigh pressure, J. Non-Cryst. Solids 279(2-3) (2001) 215-218.

[190] T. Brink, D. Şopu, K. Albe, Solid-state amorphization of Cu nanolayers embedded in a Cu 64 Zr 36 glass, Phys. Rev. B 91(18) (2015) 184103.

[191] P.J. Blau, On the nature of running-in, Tribol. Int. 38(11-12) (2005) 1007-1012.

[192] D. Kiener, R. Pippan, C. Motz, H. Kreuzer, Microstructural evolution of the deformed volume beneath microindents in tungsten and copper, Acta Mater. 54(10) (2006) 2801-2811.

[193] C. Greiner, M. Schafer, Bio-inspired scale-like surface textures and their tribological properties, Bioinspiration Biomimetics 10(4) (2015) 044001.

[194] D. Braun, C. Greiner, J. Schneider, P. Gumbsch, Efficiency of laser surface texturing in the reduction of friction under mixed lubrication, Tribol. Int. 77 (2014) 142-147.

[195] X. Chen, Z. Han, X. Li, K. Lu, Lowering coefficient of friction in Cu alloys with stable gradient nanostructures, Sci. Adv. 2(12) (2016) e1601942.

[196] G. Kermouche, G. Jacquet, C. Courbon, J. Rech, Y.Y. Zhang, R. Chromik, Microstructure evolution induced by sliding-based surface thermomechanical treatments - Application to pure copper, Mater. Sci. Forum 879 (2016) 915-920.

[197] D. Linsler, F. Schrockert, M. Scherge, Influence of subsurface plastic deformation on the running-in behavior of a hypoeutectic AlSi alloy, Tribol. Int. 100 (2016) 224-230.

[198] B. Alfredsson, A. Cadario, Explicit equations for the stresses beneath a sliding spherical contact - G M Hamilton, Proceedings Part C, 1983, 197C,53-59, Proc. Inst. Mech. Eng. C 217(2) (2003) 281-281.

Appendices

Appendix I: Hamilton solution to the stress field under sphere-plane contact

As early as in 1966, Hamilton and Goodman assume that at every point of contact, the tangential force $Q = \mu P$, where P is the normal force from classical Hertzian theory. The von Mises stress field is therefore plotted as a criterion of plastic yielding. The unsymmetrical stress field under sliding contact can be clearly seen.

In 1983, Hamilton published the explicit equations for this solution [29, 198]. Here are the explicit equations in this solution as presented in the original paper:

Normal load

$$\sigma_x = \frac{3P}{2\pi a^3}\left[(1+\nu)z\phi + \frac{1}{r^2}\left\{\frac{y^2-x^2}{r^2}\times\left[(1-\nu)Nz^2 - \frac{1-2\nu}{3}(NS+2AN+a^3) - \nu Mza\right] - N(x^2+2\nu y^2) - \frac{Mx^2za}{S}\right\}\right]$$

$$\sigma_y = \frac{3P}{2\pi a^3}\left[(1+\nu)z\phi + \frac{1}{r^2}\left\{\frac{x^2-y^2}{r^2}\times\left[(1-\nu)Nz^2 - \frac{1-2\nu}{3}(NS+2AN+a^3) - \nu Mza\right] - N(y^2+2\nu x^2) - \frac{My^2za}{S}\right\}\right]$$

$$\sigma_z = \frac{3P}{2\pi a^3}\left[-N + \frac{azM}{S}\right]$$

$$\tau_{xy} = \frac{3P}{2\pi a^3}\left[\frac{xy(1-2\nu)}{r^4}\left\{-Nr^2 + \frac{2}{3}N(S+2A) - z(zN+aM) + \frac{2}{3}a^3\right\} + \frac{xyz}{r^4}\left\{-\frac{aMr^2}{S} - zN + aM\right\}\right]$$

$$\tau_{yz} = \frac{3P}{2\pi a^3}\left[-z\left\{\frac{yN}{S} - \frac{yzH}{G^2+H^2}\right\}\right]$$

$$\tau_{zx} = \frac{3P}{2\pi a^3}\left[-z\left\{\frac{xN}{S} - \frac{xzH}{G^2+H^2}\right\}\right]$$

where $A = r^2 + z^2 - a^2; S = (A^2 + 4a^2z^2)^{1/2}; r^2 = x^2 + y^2$

and

$$M = \left(\frac{S+A}{2}\right)^{1/2};\ N = \left(\frac{S-A}{2}\right)^{1/2};\ \phi = \tan^{-1}\left(\frac{a}{M}\right)$$

and

$$G = M^2 - N^2 + zM - aN; H = 2MN + aM + zN$$

Tangential load

$$\sigma_x = \frac{3Q}{2\pi a^3}\left[-x\left(\frac{\nu}{4}+1\right)\phi + \frac{axM}{r^4}\left\{\left(\frac{3}{2}-\frac{2x^2}{r^2}\right)\times(S\nu - 2A\nu + z^2) + \frac{x^2z^2}{S} + \frac{7\nu r^2}{4} - 2\nu x^2 + r^2\right\}\right.$$
$$+ \frac{xzN}{r^4}\left\{\left(\frac{3}{2}-\frac{2x^2}{r^2}\right)\left[-\frac{S}{6}(1-2\nu) - \frac{A}{3}(1-2\nu) - \frac{1}{2}(z^2+3a^2)\right] + \frac{a^2x^2}{S} - \frac{\nu r^2}{4} - \frac{7r^2}{4}\right\}$$
$$\left. + \frac{4a^3xz}{3r^4}\left(\frac{3}{2}-\frac{2x^2}{r^2}\right)(1-2\nu)\right]$$

$$\sigma_y = \frac{3Q}{2\pi a^3}\left[-\frac{3\nu x\phi}{4} + \frac{axM}{r^4}\left\{\left(\frac{1}{2}-\frac{2y^2}{r^2}\right)\times[\nu(S-2A+r^2)+z^2] + \frac{y^2z^2}{S} + \frac{3\nu r^2}{4}\right\}\right.$$
$$+ \frac{zxN}{r^4}\left\{\left(\frac{1}{2}-\frac{2y^2}{r^2}\right)\left[-\frac{S}{6}(1-2\nu) - \frac{A}{3}(1-2\nu) - \frac{1}{2}(z^2+3a^2)\right] + \frac{a^2y^2}{S} - \frac{3\nu r^2}{4} - \frac{r^2}{4}\right\}$$
$$\left. + \frac{4a^3zx}{3r^4}\left(\frac{1}{2}-\frac{2y^2}{r^2}\right)(1-2\nu)\right]$$

$$\sigma_z = \frac{3Q}{2\pi a^3}\left[\frac{zxN}{2r^2}\left\{1 - \frac{r^2+z^2+a^2}{S}\right\}\right]$$

$$\tau_{xy} = \frac{3Q}{2\pi a^3}\left[\frac{y}{2}\left(\frac{\nu}{2}-1\right)\phi + \frac{ayM}{r^4}\left\{\frac{x^2z^2}{S} + \nu\left[(S-2A)\times\left(\frac{1}{2}-\frac{2x^2}{r^2}\right) - 2x^2 + \frac{r^2}{4}\right] + \frac{r^2}{2} + z^2\left(\frac{1}{2}-\frac{2x^2}{r^2}\right)\right\}\right.$$
$$+ \frac{yzN}{r^4}\left\{\left(\frac{1}{2}-\frac{2x^2}{r^2}\right)\left[(2\nu-1)\left(\frac{S}{6}+\frac{A}{3}\right) - \frac{z^2}{2} - \frac{3a^2}{2} - \frac{r^2}{2}\right] + \frac{r^2\nu}{4} + \frac{a^2x^2}{S} - \frac{y^2}{2} - \frac{3x^2}{2}\right\}$$
$$\left. + \frac{4a^3yz}{3r^4}\left(\frac{1}{2}-\frac{2x^2}{r^2}\right)(1-2\nu)\right]$$

$$\tau_{yz} = \frac{3Q}{2\pi a^3}\frac{xyz}{2r^4}\left[aM\left\{\frac{1}{2} + \frac{1}{S}\left(\frac{z^2}{2} - \frac{3a^2}{2} - \frac{r^2}{2}\right)\right\} + \frac{zN}{2}\left\{-3 + \frac{1}{S}(5a^2+z^2+r^2)\right\}\right]$$

$$\tau_{zx} = \frac{3Q}{2\pi a^2}\left[\frac{3z\phi}{2} + \frac{azM}{r^2}\left\{1 + \frac{x^2}{r^2} - \frac{x^2}{S}\right\} + \frac{N}{r^2}\times\left\{-\frac{3}{4}(S+2A) + z^2 - \frac{3}{4}a^2 - \frac{1}{4}r^2 + \frac{z^2}{2}\left(\frac{1}{2}-\frac{2x^2}{r^2}\right)\right\}\right]$$

where *A, S, M, N, r* and ϕ are the same as before.

Appendix Figures

Figure A1: Contour maps of von Mises stress of a circular contact in the subsurface cross-sectional area of the contact calculated using classical Hertzian model and Hamilton's solution. Enlarged images of Fig. 1.2. (a) Hertzian model; (b) Hamilton solution. The coefficient of friction here is 0.25. Distances are normalized by the Hertzian contact radius and the stress level is normalized to maximum Hertzian pressure. z-axis is the sample surface normal and x-axis is the sliding direction [28]. The sample is plotted as the upper contact body so that the normal load is along the z-axis in positive direction, and the tangential force is in x-axis positive direction.

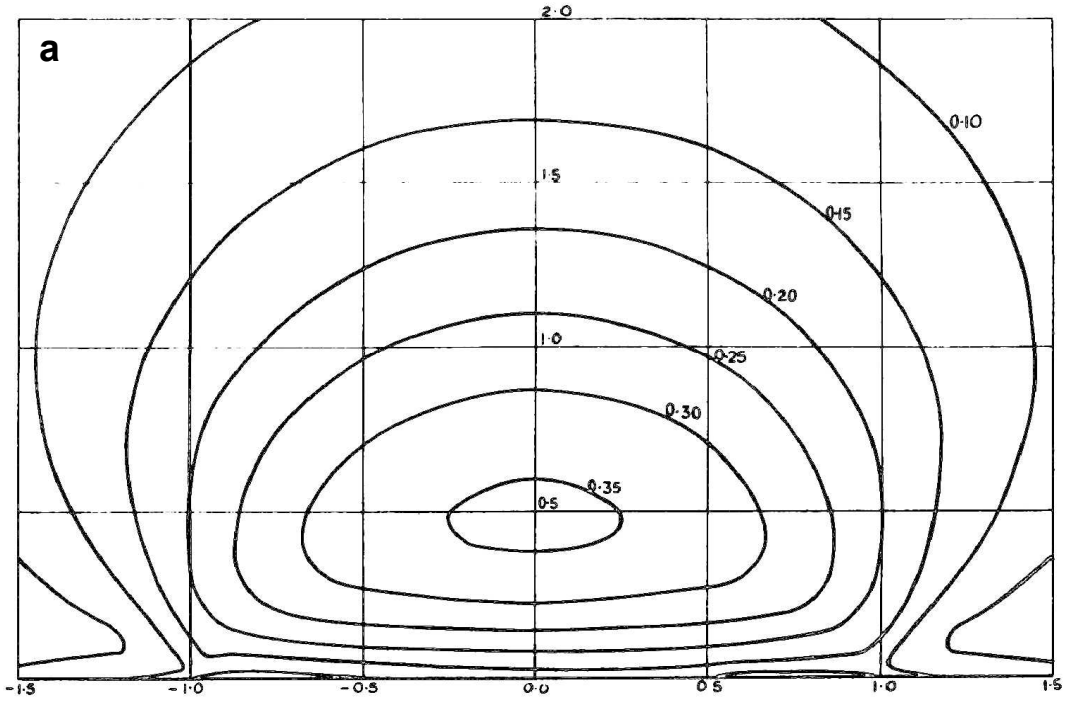

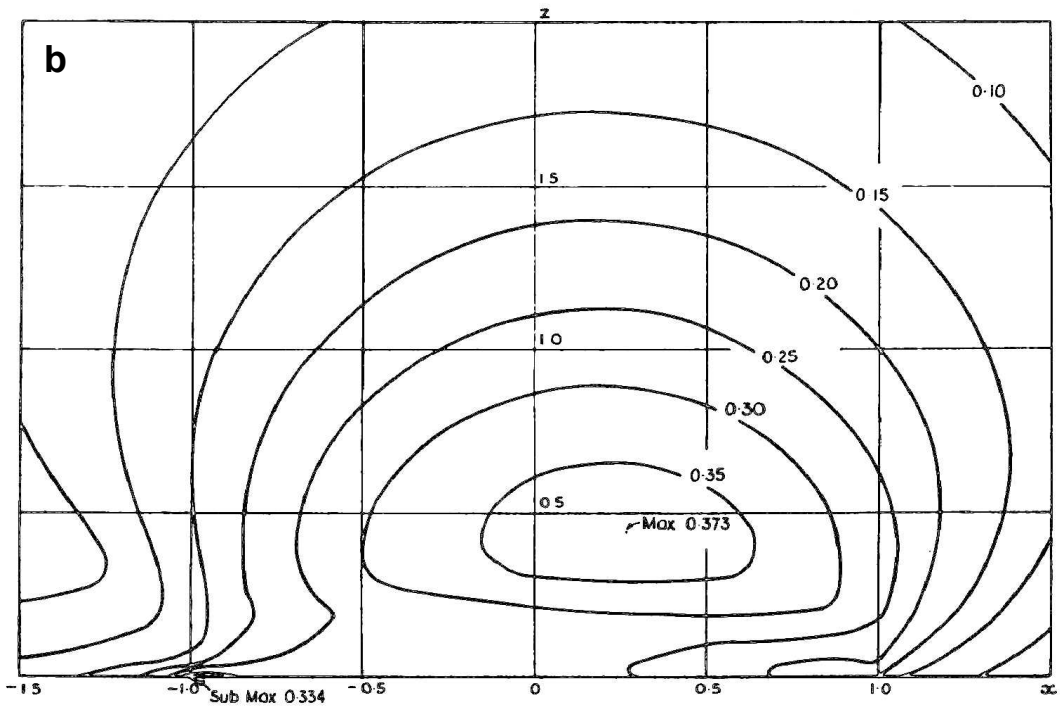
b
z
0·10
0 15
0 20
0·25
0·30
0·35
1 5
1 0
0 5
Max 0·373
Sub Max 0·334
−1 5
−1·0
−0·5
0
0·5
1·0
x

Figure A2: SEM/FIB image of the initial microstructure of the OFHC copper sample surface. The image is acquired via secondary electrons induced by the ion beam. The grains with different crystallographic orientations are clearly visible through a channeling effect of the ion beam. The average grain size is between 30 and 40 µm.

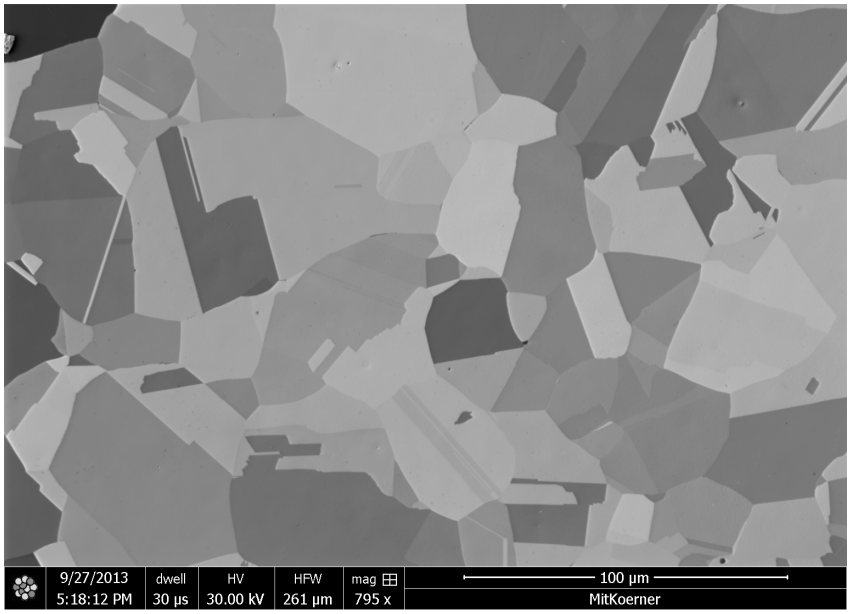

Figure A3: Enlarged image of the Fast Fourier transform (FFT) image in the right-bottom corner of Fig. 3.3b [156]. The FFT was perfomed in the area beneath the dislocation trace line in Fig. 3.3b. The spots in red circles are used for inverse FFT for enhanced view of atom planes.

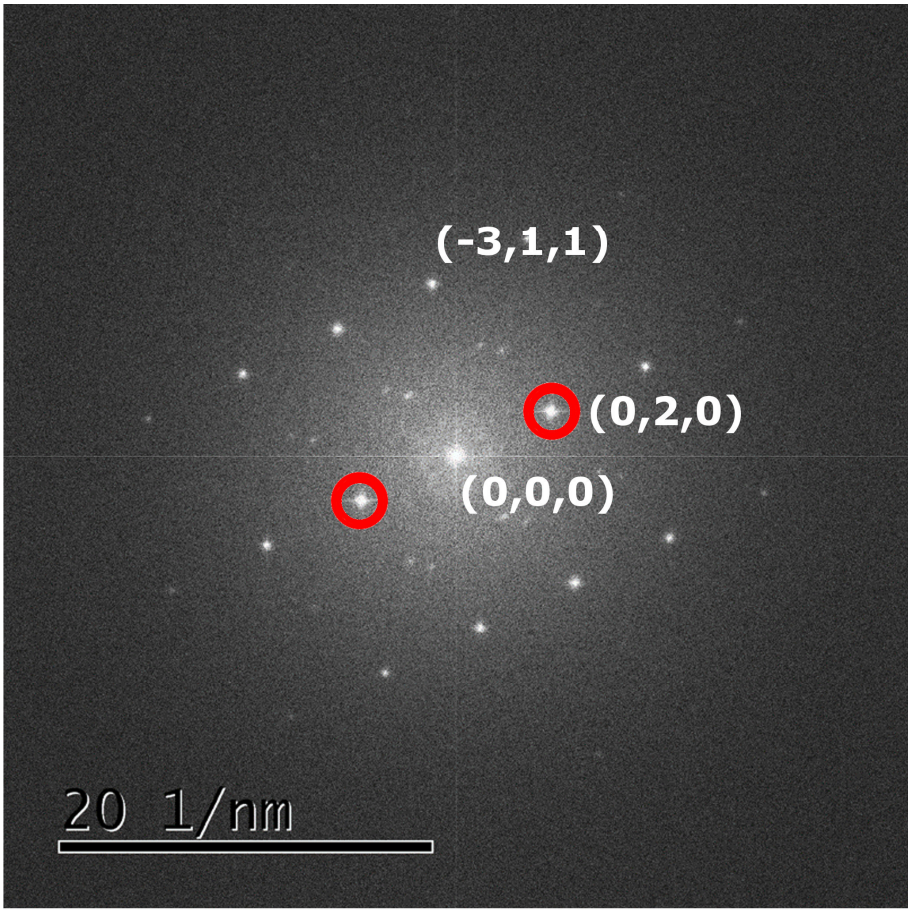

Figure A4: SEM images of OFHC copper under tribological loading after different cycle numbers at the dead centers. (a, b) after 10 cycles; (c, d) after 100 cycles; (e, f) after 500 cycles; (g, h) after 1000 cycles; (i, j) after 5000 cycles. The cross-sections were prepared at the two dead centers of each wear track, perpendicular to the sliding surface and parallel to the sliding direction. (a, c, e, g, i) are at the left dead center, (b, d, f, h, j) are at the right dead center. The contrast at the top of the images is from the two protective platinum layers.

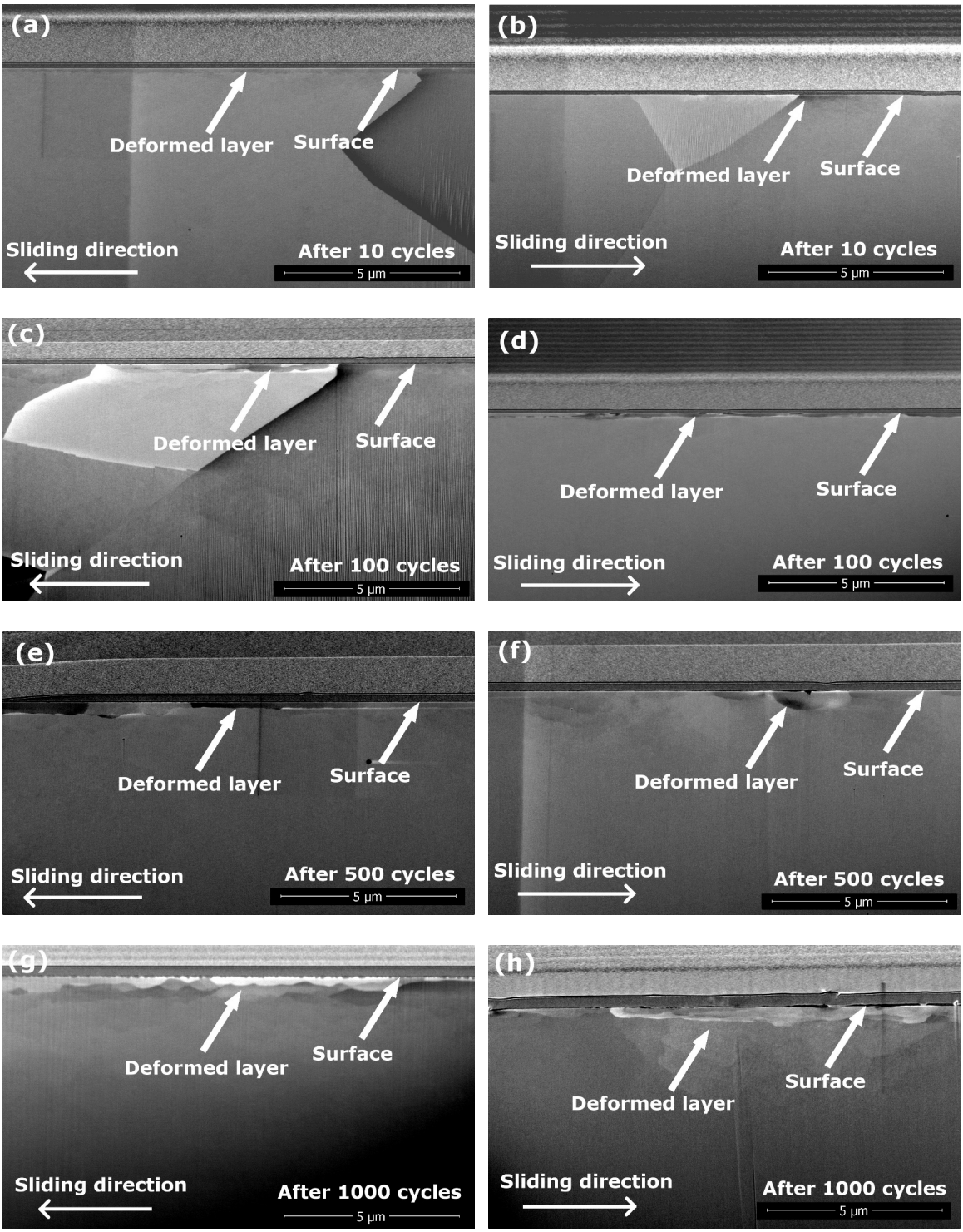

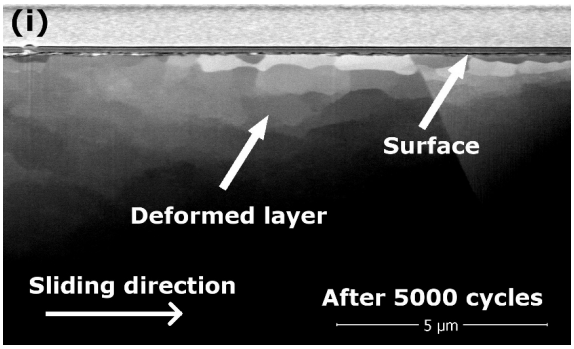
(i)
Surface
Deformed layer
Sliding direction
After 5000 cycles
5 µm

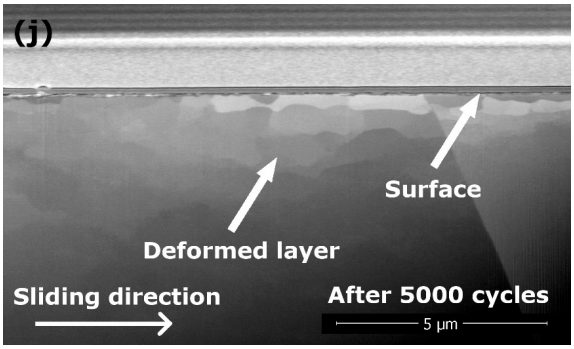
(j)
Surface
Deformed layer
Sliding direction
After 5000 cycles
5 µm

Figure A5: Micro hardness measurement in the cross-sectional area of the wear track after 5000 cycles loading [166]. Note that the x-axis and y-axis use different scale. The measurement was performed with micro hardness measurement instrument, and for a large area scan covering the whole wear track, the measurement was performed in three continuous areas and then stitched together for mapping.

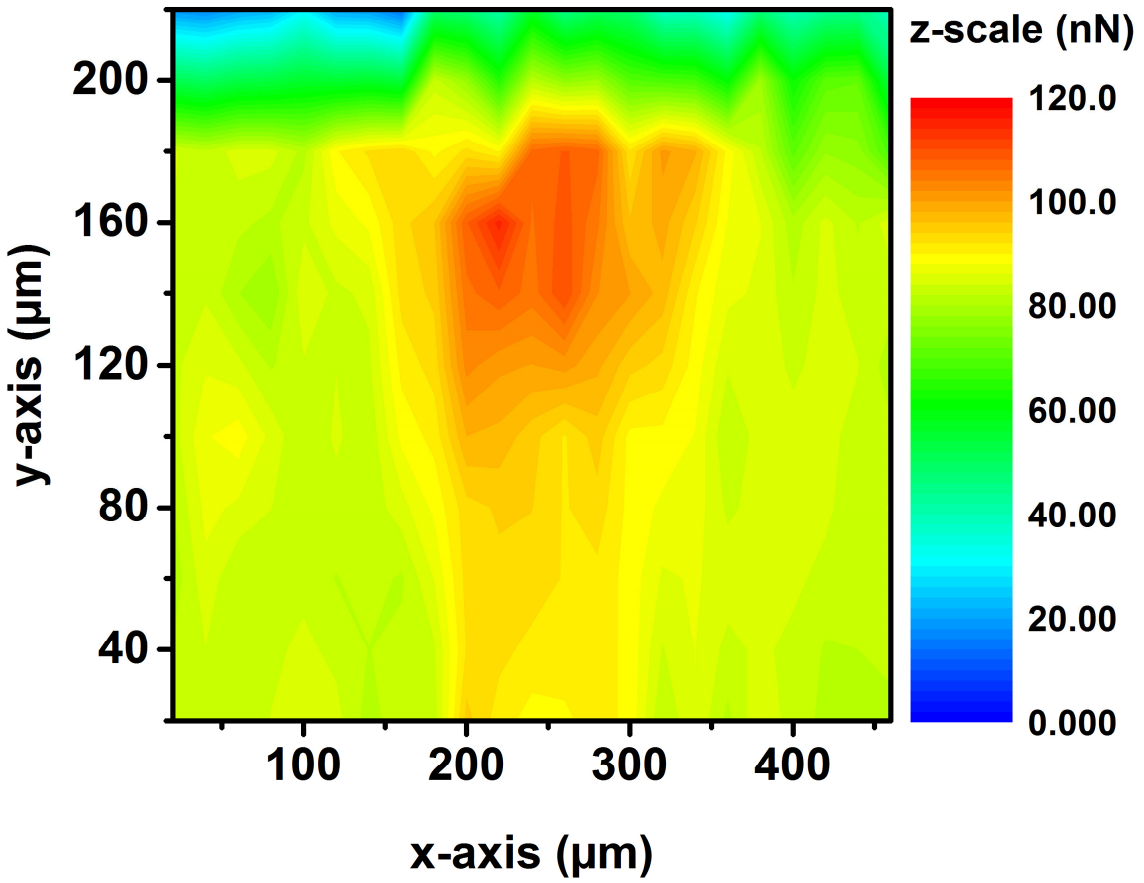

Figure A6: (HR)TEM images of a cluster after 5000 cycles of tribological loading [159]. (a) BF image; (b) DF image using one of the diffraction beams; (c) HRTEM image from the area in the red rectangle in (b). The results are taken from the same lamella as shown in Fig. 3.15c. The sample surface is marked by dashed white lines. The sliding direction is marked by a white double arrow. (d) STEM image in HAADF mode showing the two windows where the EDXS spectra data were acquired. (e) spectra for the two windows in (d) for a range in X-Ray photon energy of 0.1-10.0 keV; (f) spectra for the two windows in (d) for a range in X-Ray photon energy of 0.1-1.5 keV.

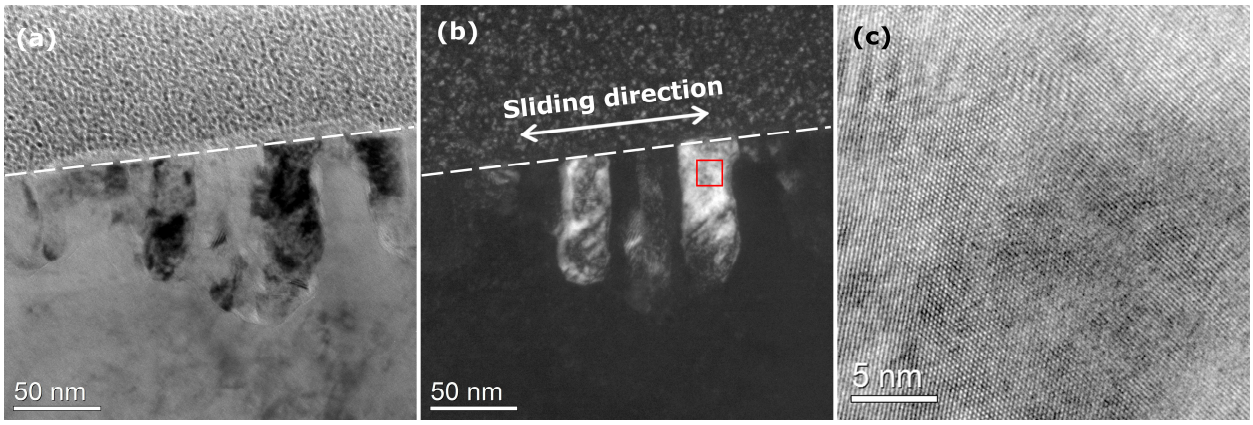

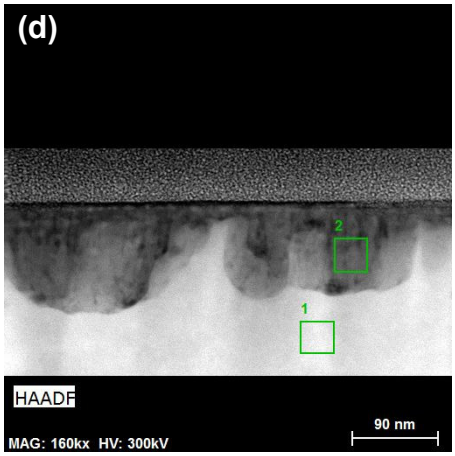

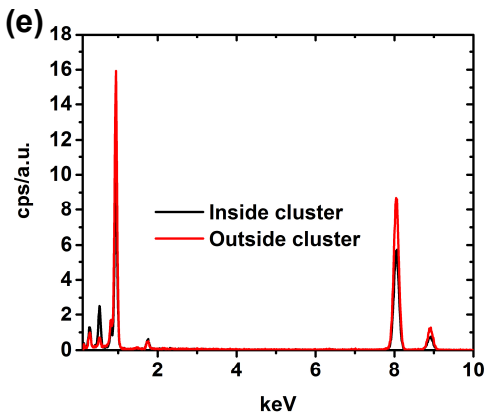

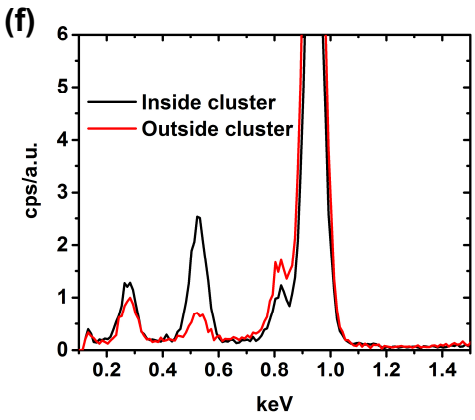

Figure A7: STEM image and EDXS spectra results on the cross-sectional area of a TEM lamella from the wear track after 10 cycles of tribological loading [159]. The experiment used 1.5 N normal load and a sapphire sphere as the counter body. (a) STEM image in HAADF mode. (b) spectra for the two windows in (a) for a range in X-Ray photon energy of 0.1-10.0 keV; (e) spectra for the two windows in (a) for a range in X-Ray photon energy of 0.1-1.5 keV. The spectrum above and beneath the trace line shows that there is no difference in the chemical composition between the two areas.